Fakultät für Maschinenwesen
Lehrstuhl für Carbon Composites

A Simulation Approach of Permeability Prediction for RTM Process Simulation

Christoph Hahn

Vollständiger Abdruck der von der Fakultät für Maschinenwesen der Technischen Universität München zur Erlangung des akademischen Grades eines

Doktor-Ingenieurs (Dr.-Ing.)

genehmigten Dissertation.

Vorsitzender:	Prof. Dr.-Ing. habil. Boris Lohmann
Prüfer der Dissertation:	Univ.-Prof. Dr.-Ing. Klaus Drechsler
	Prof. Christophe Binetruy, PhD
	(Ecole Centrale de Nantes, France)

Die Dissertation wurde am 21.05.2014 bei der Technischen Universität München eingereicht und durch die Fakultät für Maschinenwesen am 24.10.2014 angenommen.

For every ailment under the sun there is a remedy, or there is none;
If there be one, try to find it; If there be none, never mind it.

W.W. Bartley

Abstract

Following the trend of growing fiber composite materials usage, process automation and increasing component complexity, there arises a need for process prediction using simulation. The work presented here addresses a fast and robust characterization method of permeability for RTM process modeling. A simulation approach is presented based on fabric images, image processing and textile modeling. The core of the approach is comprised of algorithms for image processing that are presented. A parameter study on six fabrics was conducted demonstrating its capabilities. In the following, the simulation approach itself was investigated more in-depth and a sensitivity as well as a mesh refinement study were conducted. Finally the simulation approach was applied to a validation geometry and the quality of RTM process prediction was assessed.

For comparison of the simulation approach to experimental permeability characterization and RTM manufacturing a two-step validation approach was followed. At first, a test-setup for permeability testing was developed and put into service. A test campaign focusing on non-crimp fabrics (NCF) gave the permeability results for comparison of material data. Participation at the second permeability benchmark exercise proved the credibility of the experimental facilities. In a second step the simulation approach was employed to predict the fill time and flow front pattern of a complex component. The RTM experiments were conducted including a sensor-based evaluation of flow front progression. The permeability results from experiments and the simulation approach showed excellent correlation for two biaxial non-crimp fabrics. For the fill time prediction of the RTM component, the simulation approach gave the best results and the flow front pattern could be predicted reasonably well.

Kurzzusammenfassung

Im Zuge der wachsenden Bedeutung von Faserverbundwerkstoffen als Konstruktionswerkstoff, der fortschreitenden Automatisierung und zunehmend komplexeren Bauteilen steigt die Notwendigkeit Prozessvorhersagen zur Herstellung mittels Simulation zu treffen. Im Folgenden wird ein schneller und robuster Simulationsansatz zur Permeabilitätsbestimmung für die RTM-Prozessimulation vorgestellt, dieser basiert auf der Analyse von Bilddaten der betreffenden Textilien und deren anschließender Modellierung. Das Herzstück der Methode bilden Algorithmen zu Bildanalyse. Diese werden vorgestellt und exemplarisch auf Bilddaten von sechs verschiedenen Textilien angewendet um deren Leistungsfähigkeit zu zeigen. Des Weiteren wird der Simulationsansatz untersucht und dabei eine Sensitivitäts- sowie eine Netzfeinheitsstudie durchgeführt. Schließlich wird der Simulationsansatz an einem Validierungsbauteil eingesetzt und die Qualität der Vorhersage wird durch den Vergleich mit RTM-Experimenten gezeigt.

Zum Abgleich des Simulationsansatzes wurde ein zwei-stufiges Vorgehen gewählt. Zum einen wurde im Zuge der Arbeit ein Prüfstand zur experimentellen Permeabilitätsbestimmung entwickelt und in Betrieb genommen. Ein Testkampagne mit Multiaxial-Gelegen lieferte Ergebnisse um die reinen Materialkenndaten vergleichen zu können. Die Teilnahme an der zweiten internationalen Permeabilitäts-Benchmark-Studie zeigte die Glaubwürdigkeit der experimentellen Ergebnisse. In einem zweiten Schritt wurde der Simulationsansatz eingesetzt um bei einem Valdidierungsbauteil Füllzeit und Flieffrontverlauf vorherzusagen. Bei den RTM-Experimenten wurde der Fließfrontfortschritt mit kapazitiven Sensoren gemessen um den Vergleich mit der Simulation zu ermöglichen. Die Permeabilitsergebnisse aus den Experimenten und dem Simulationsansatz zeigen sehr gute Übereinstimmung für die zwei getesteten Biaxial-Gelege. Bei der Füllzeitvorhersage für den RTM-Prozess gibt der Simulationsansatz die besten Ergebnisse. Ebenso kann der Fließfrontverlauf hinreichend genau vorhergesagt werden.

Acknowledgements

I would like to thank everyone who helped me throughout the course of my research. My deep gratitude to Prof. Klaus Drechsler for providing the excellent research environment and the Audi AG for funding the work presented here. The number of contacts I made at Audi is too high to mention everybody, thank you all for your support, thank you Joachim.

Many thanks to Prof. Christophe Binetruy for his guidance, enthusiastic support and optimism. The great collaboration and the numerous long discussions gave direction to that project.

I want to thank all colleagues at the research groups around the globe focusing on liquid composite molding for their ongoing support and inspiration, especially Stepan V. Lomov with his team at KU Leuven and Christophe Binetruy together with Sebastien Comas-Cardona at EC Nantes. Many thanks to Peter Mitschang and his group for their support in RTM manufacturing, thank you Matthias. Thanks a lot to Simon Bickerton and Piaras Kelly at the University of Auckland, Francois Trochu and Edu Ruiz at Ecole Polytechnique in Montreal and to the guys at SICOMP Sweden. You all made it a great pleasure to establish research on that field at LCC.

Moreover, I want to say thank you to all colleagues at the LCC who have supported me. Thanks heaps Elinor, Swen, Andrew and Reinhold who were involved in my research for your support. Thank you Elisabeth and Roland for management and supervision, I have learned a lot. Keep the great *'Yes we can'* -attitude.

Finally, a big kiss to my wife Lisa and my family for all the love and support throughout the time. Your encouragement has been a great help and motivation.

Contents

Nomenclature

Abbreviations

CFD	Computational fluid dynamics
CoV	Coefficient of variation
De	Deborah Number
FEA	Finite element analysis
FRP	Fiber reinforced polymers
GLCM	Gray level co-occurrence matrix
GUI	Graphical user interface
IYF	Intra-yarn flow
LCM	Liquid composite molding
LSF	Least square fit (approach)
NCF	Non-crimp fabric
OEM	Original equipment manufacturer
PH	Pre-heating
Re	Reynold Number
RF	Reduction factor
RTM	Resin transfer molding
RVE	Representative volume element
SFF	Squared flow front (approach)
STM	Stitched mat model (WiseTex specific wording)
UD	Uni-directional

Symbols

A	$[m^2]$	Area
β	$[^\circ]$	Permeability ellipse rotation: angle between K_{0° and K_1
CoV	[%]	Coefficient of variation
Da	$[-]$	Darcy number
d	$[m]$	Distance
ϵ	$[-]$	Shear strain
$\dot{\epsilon}$	$[1/s]$	Shear rate
δ	$[^\circ]$	Shear angle
$\mathbf{K}$		Permeability tensor
K_1	$[m^2]$	Principal permeability along major ellipse axis
K_{0°	$[m^2]$	Permeability along direction 0°
m_a	$[g/m^2]$	Areal weight
μ	$[N \cdot s/m^2]$	Dynamic viscosity
n	$[1/min]$	Revolution speed
p	$[N/m^2]$	Pressure
ϕ	[%]	Porosity
Re	$[-]$	Reynolds number
t	$[mm]$	Thickness
θ	$[^\circ]$	Fiber orientation
V_f	[%]	Fiber volume fraction

1 Introduction

1.1 Composite Materials

Composite materials, or composites, are materials that are produced by combining materials to a structure that is better than the individual components [1]. In the following thesis, the expression *composite materials* will be used to describe fiber reinforced polymers (FRP) comprised of carbon fibers and a polymeric epoxy matrix. Composite materials have significant advantages compared to traditional lightweight materials – combining low density with high stiffness and strength. The composite sector has experienced rapid growth in recent years. In the aerospace industry, Airbus and Boeing have demonstrated a considerable increase of carbon fiber composites use for the A350 and 787 *Dreamliner* compared to their previous developments A380 and 777 [2]. In the automotive sector companies have started to bring composites into series production such as AUDI together with Lamborghini the Aventador and BMW the i3 and i8. A study published by Mc Kinsey & Company [3] predicts a 17% annual increase in the use of carbon fiber for the automotive sector worldwide between 2010 and 2030. However, the study mentions a major challenge original equipment manufacturers (OEM) will have to address due to the more expensive material: "the OEMs will be directly confronted with a threat to their margins and may have to deal with the additional cost of challenges that cannot be fully anticipated at the moment, such as repair and maintenance. Competence in lightweight thus will be key in future cost competitiveness". It comes without saying that cost-effectiveness is a key-parameter for the success of new technologies. With respect to the composite materials sector, the result during each step along the manufacturing chain costs must be reduced significantly compared to current practice. The work presented in this thesis will focus on efficient material characterization and manufacturing process simulation. These will aid the development of robust and thus cheap manufacturing processes and avoid additional costs due to trial-and-error engineering in process development.

1.2 Liquid Composite Molding

Liquid composite molding (LCM) processes involves the impregnation of a dry fiber preform with liquid resin. The main goal of LCM processing is to fully and quickly saturate the empty space between the fibers with the resin before it gels. Commonly, thermosetting resins with low pre-cure viscosity are used. A complete summary of LCM processes is given by Advani and Sozer [4]. Liquid composite molding processes encompass processes such as RTM and VARI which will be presented in the following.

1.2.1 Resin Transfer Molding

Resin Transfer Molding (RTM) manufacturing requires a tool that is in the shape of the part where the fiber preform is placed. The tool is closed and held under pressure by clamping mechanically, for example, by using a press. The resin is injected into the compressed preform through the injection gates from an injection device (e.g. pressure pot, multi-component injection device). When the injection is finished the resin is allowed to cure and finally the component is demolded. A schematic of the process and the equipment involved is depicted in Figure 1.1[1].

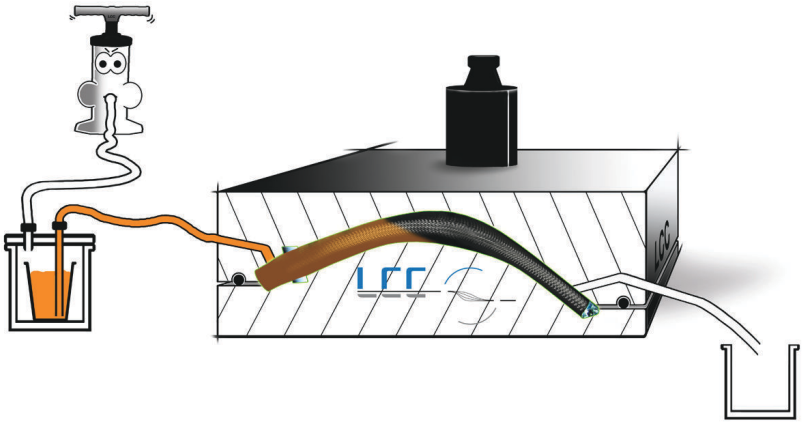

Figure. 1.1: Schematic of RTM process

RTM allows lower-cost production of complex parts with good surface quality compared to autoclave manufacturing. As RTM is a process classification rather than a process definition, various alternative expressions exist. To reduce pore content of RTM components the cavity can be evacuated before injecting, known as Vacuum Assisted RTM (VaRTM). RTM-light describes a tool with lower stiffness that is cheaper so that the part dimensions - especially the thickness - are prone to the variations of process induced forces such as the injection pressure. For recent developments towards RTM series production, including injection pressure higher than 40 bar and curing times shorter than 5min, expressions such as *high-pressure* (HP) RTM are employed. Very accurate positioning of the press, allows to leave a gap between between the mold halves during injection and close it before the mold is filled. Thereby the injection pressure for equal fill time can be reduced compared to classic RTM at the expense of increased tooling force during final closure. This feature is commonly described as compression RTM (C-RTM) or *Spalt-RTM* in the German language.

Today's industrial applications of the RTM process are numerous. The German OEMs in the automotive sector have established processes where components are manufactured in series production by using injection pressures higher than $30bar$ and resins that allow demolding at less than $3min$ after injection. Another application that illustrates the degree of geometrical complexity that can be achieved using RTM processing is given

[1]Source: LCC lecture notes

in the following: Figure 1.2 shows at the right the chassis[2] of the Roding roadster car[3] depicted in the left. This car is produced in small series and the decision to use RTM was made for the sake of repeatability and surface quality.

Figure. 1.2: Roding roadster and its RTM chassis

1.2.2 Vacuum Assisted Resin Infusion

For vacuum assisted resin infusion (VARI), as can be seen in Figure 1.3[4] the top half of the mold is replaced by a vacuum bag, similar to the autoclave process. The pressure gradient to drive the liquid resin is generated by vacuum. Often, an additional layer of an easy-to-saturate distribution medium is employed to counterbalance the drawback of low injection pressure, such as the Seemann's composite resin infusion molding process (SCRIMP). For low pore content and robust processing even with imperfect sealing, air-permeable membranes are used for evacuation as it is practiced in the so-called VAP process.

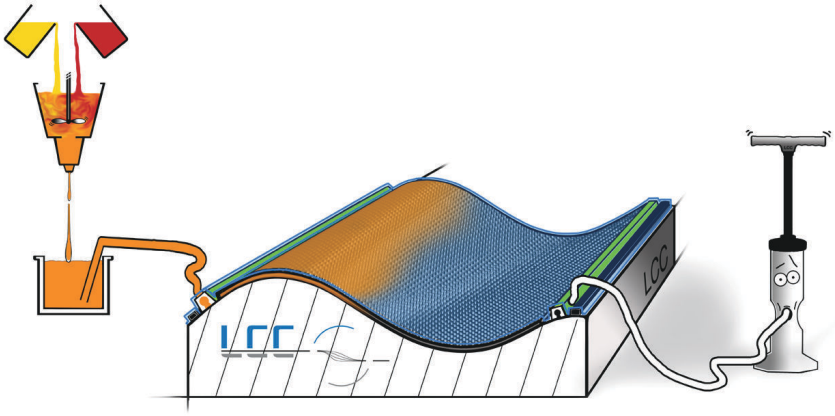

Figure. 1.3: Schematic of VARI process

[2] `http://www.sk-carbon.de/bauteilfertigung.html`, checked 12/03/2014

[3] `http://www.roding-automobile.de/roding-roadster/roding-roadster-r1/fahrzeug.html`, checked 12/03/2014

[4] Source: LCC lecture notes

A schematic of the process and the equipment involved is depicted in Figure 1.3. Resin infusion is applied for some applications due to its simplicity, low costs for equipment and the ability to manufacture large structures such as boat hulls or wind blades as depicted in Figure 1.4[5].

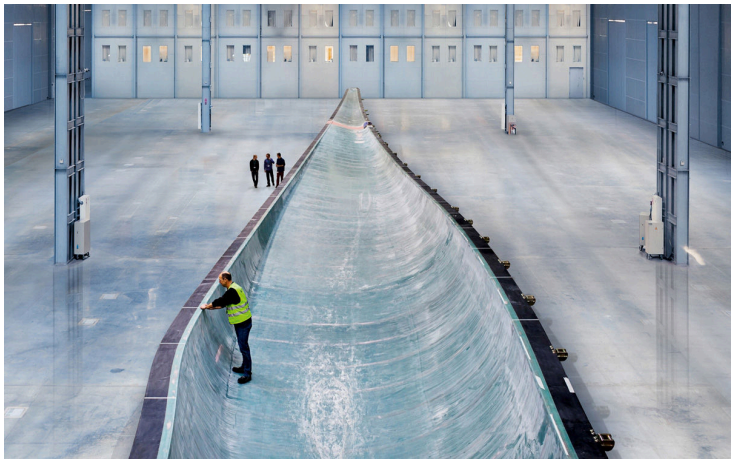

Figure. 1.4: Composite mold of a rotor blade half for wind turbines

1.2.3 Definition of Fiber Volume Fraction and Areal Weight

A very important property in connection with LCM processes is the fiber volume fraction, which denotes the ratio between volume of fibers in a control volume and the control volume itself. The fiber volume fraction will be denoted as V_f in the following and is defined as follows:

$$V_f = \frac{m_{preform}}{\rho_{fiber} \cdot A_{preform} \cdot t} = \frac{m_a}{\rho_{fiber} \cdot t} \; [-], \tag{1.1}$$

with the preform mass $m_{preform}$, the density of the fibers ρ_{fiber} and the cavity volume which is defined as the area of the preform $A_{preform}$ multiplied by its thickness t. Instead of V_f, a term denoted as porosity ϕ is commonly used. The relation between V_f and ϕ reads as follows:

$$\phi = 1 - V_f \tag{1.2}$$

To express the weight of a fabric, one commonly uses the area specific weight, or simply areal weight, denoted as m_a:

$$m_a = \frac{m_{preform}}{A_{preform}} \; \left[\frac{g}{m^2}\right] \tag{1.3}$$

[5]http://www.bine.info/typo3temp/pics/183ada11ba.jpg, , checked 12/03/2014

1.3 Motivation

With the trend of increasing use of composite materials, industry and here especially automotive companies are strongly supporting application and development of composite manufacturing process simulation. The complexity of components and process technology is significant and design based on experience or 'rule of thumb' is hazardous.

For these reasons, process simulation and process validation using simulation are particularly valuable. For a well-established process such as RTM, models have been developed and implemented as presented in Chapter 2. However, the benefit of process simulation requires considerable effort to understand material behavior for realistic process simulations. As entrepreneurial decisions have a strong focus on the cost-benefit ratio, there is a requirement for fast and robust material characterization prior to manufacturing process simulation.

The principal aim of this project is to develop efficient, cost-effective characterization techniques to provide data in a timely manner for use in LCM process simulations. This will allow more widespread use of LCM process simulation.

1.4 Objectives of the Thesis

Three major objectives were considered based on the motivation.

- Development of a fast and robust method for material characterization:
  The method should enable users to determine permeability in-house, even if they don't have practical experience with permeability testing. Furthermore, the time to obtain the desired data should be fast enough to fit in the overall picture of simultaneous engineering. So, it should be possible to conduct process simulation to validate manufacturability during the concept- and design-phase of a component where the material and lay-up are prone to changes.

- Development of an experimental permeability test setup:
  Before introducing a novel approach it is essential that trustworthy information can be obtained. Therefore, an experimental test setup shall be designed and brought into service. With that setup, experiments in the framework of the 2^{nd} permeability benchmark exercise shall be conducted on the one hand to ensure that results correlate to other institutes specialized on permeability testing; on the other hand a reliable database to validate the new approach should be created.

- Application of the method to process simulation of a demonstrator component:
  The method developed method shall be applied to a component. RTM manufacturing of a component or validation geometry shall be conducted including flow front tracking. Furthermore, the preform shall be assessed to obtain the fiber orientation and hence the shear strain. With this knowledge it is possible to validate the resin injection of a real component compared to RTM process simulation with the input data of the new method.

1.5 Thesis Outline

Chapter 1 gives an introduction to carbon fiber composites and their use with a focus on LCM manufacturing. Furthermore, the *gap of knowledge* is described that motivates the thesis project. Based on the motivation the goals are derived and an outline to the whole thesis document is given. Finally, the assumptions made within the thesis are stated.

Chapter 2 summarizes the state of the art and the fundamental equations describing RTM, permeability determination - analytic and experimental techniques - as well as LCM process modeling. As the approach to be developed will deal with fabric unit cell models and digital image processing the current state of research on these fields is presented and evaluated.

Chapter 3 introduces the setup to determine permeability experimentally. The contribution to the 2^{nd} permeability benchmark exercise is presented. The results of a permeability test campaign with two non-crimp fabrics and the permeability results with respect to areal weight, fiber volume fraction (V_f), number of layers and stack thickness are presented.

In Chapter 4, a simulation approach for permeability prediction is presented which is based on digital image processing applied to optically scanned samples of a fabric. The results are used to set up unit cell models of the fabric. Based on their discretized form in voxel format a computational fluid dynamics (CFD) simulation is performed where permeability is obtained.

Chapter 5 focuses on the validation of the simulation approach on two levels. At first, the permeability values obtained with the simulation approach are compared to the results obtained experimentally. In a second step, the results from the simulation approach are used to set up a component model which is compared to the real-world resin injection.

Chapter 6 summarizes the results obtained within this project and evaluates them. Open questions are stated and an outlook is given about how further research on that field could look like.

1.6 Assumptions and Restrictions

For the project certain assumptions have been made:

- The focus throughout the project was put on carbon-fiber non-crimp fabrics (NCF), because this class of materials is the first choice for structural applications in series production such as in automotive industry when impact loading or optical appearance are of secondary importance. It goes without saying, most of the work conducted within the project could be applied to other fabric types such as woven or braided fabrics. The digital image processing has been particularly developed and adjusted to detect and analyze properties specific for biaxial NCFs such as the small gaps created during the stitching of the UD layers.

- The material permeability characterization was conducted based on scanned images of the dry NCFs. Hence, it was necessary to assume that RTM processing does not alter the fabric structure. For robust RTM manufacturing this is anyhow required as fabric structure and structural properties are closely related and process induced deviation cannot be tolerated. For the validation component presented here, this statement has been proven to be acceptable.

- The material characterization was conducted on undeformed samples of the fabric and all deformations occurring during preforming were applied to numeric models of the fabric. Every change that a fabric is subject to during preforming can be expressed as in-plane (shear) or out-of-plane deformation (compression). Hence, the assumption was made that permeability of a fabric lay-up is a function of V_f and shear strain ϵ, i.e. $K = f(V_f, \epsilon)$. Another reason is that current RTM solvers usually can typically deal with variations of fiber volume fraction. Furthermore, it is inefficient to develop permeability characterization to an extend so that common RTM solvers cannot deal with it anymore, because the overall project goal is fast and efficient material characterization for RTM process simulation.

- For this work the focus was set on in-plane permeability determination, through-thickness flow and permeability were not considered. It was checked for any case that simplification to the 2D simplification is admissible. Furthermore it was assumed that the fabric lay-up is equal over the component dimensions. The overall focus of the project was on RTM manufacturing assuming a perfectly rigid mold, mold deflections have not been considered.

2 State of the Art

Chapter 2 presents an overview of the state of research and available implementations in the following fields:

- LCM Manufacturing (Section 2.1): The underlying governing equations and involved assumptions are presented.
- Permeability (Section 2.2): The definition of permeabilits is introduced and concepts for evaluation are reviewed.
- LCM Process Modeling (Section 2.3): Based on the governing equations introduced in Section 2.1, relevant simplifications and whether they are applicable are discussed and available simulation approaches and software tools are presented.
- Textile Modeling (Section 2.4): The background of micromechanics for textile modeling is assessed and concepts as well as available tools are studied with a particular focus on how permeability can be determined with textile modeling.
- Digital Image Processing (Section 2.5): Definitions and key concepts of digital image processing are presented with a focus on image segmentation and extraction of geometrical information.

2.1 Governing Equations for Flow in LCM

Darcy's law is the underlying equation of motion (conservation of momentum) for resin flow in resin transfer molding. The averaged flow front velocity $\langle \boldsymbol{v} \rangle$ is proportional to the difference of the averaged pressure gradient $\nabla \langle p \rangle$ and body force $\rho\, \boldsymbol{g}$. The coefficients of proportionality are the material properties permeability $\boldsymbol{K}$ and viscosity μ:

$$\langle \boldsymbol{v} \rangle = -\frac{\boldsymbol{K}}{\mu} \cdot \left[\nabla \langle p \rangle - \rho\, \boldsymbol{g} \right]. \tag{2.1}$$

Darcy's law and the continuum equation for an incompressible fluid,

$$\nabla \cdot \boldsymbol{v} = 0, \tag{2.2}$$

provide the basis for describing flow in RTM.

Darcy's law can be derived from the most general form of the equation of motion, the Navier-Stokes equations:

$$\frac{\partial \left(\rho \boldsymbol{v} \right)}{\partial t} + \nabla \cdot \left(\rho \boldsymbol{v} \boldsymbol{v} \right) = \nabla \cdot \sigma + \rho \boldsymbol{g}, \tag{2.3}$$

by applying local volume averaging and introducing certain assumptions. Volume averaging is a method to upscale physical laws in a heterogeneous material and can be conducted for a quantity $f(x)$ in a domain with the volume V by integrating it over the entire volume [5] (p.95):

$$< f(x) >= \int_V \frac{1}{V} \cdot f(x)\, dV \tag{2.4}$$

The size of the domain is crucial, because it is the main criterion determining whether averaging will lead to intrinsic homogenized properties. An illustration of volume averaging is given in Figure 2.1. A more-in-depth introduction to homogenization will be given in Section 2.4 Textile Modeling.

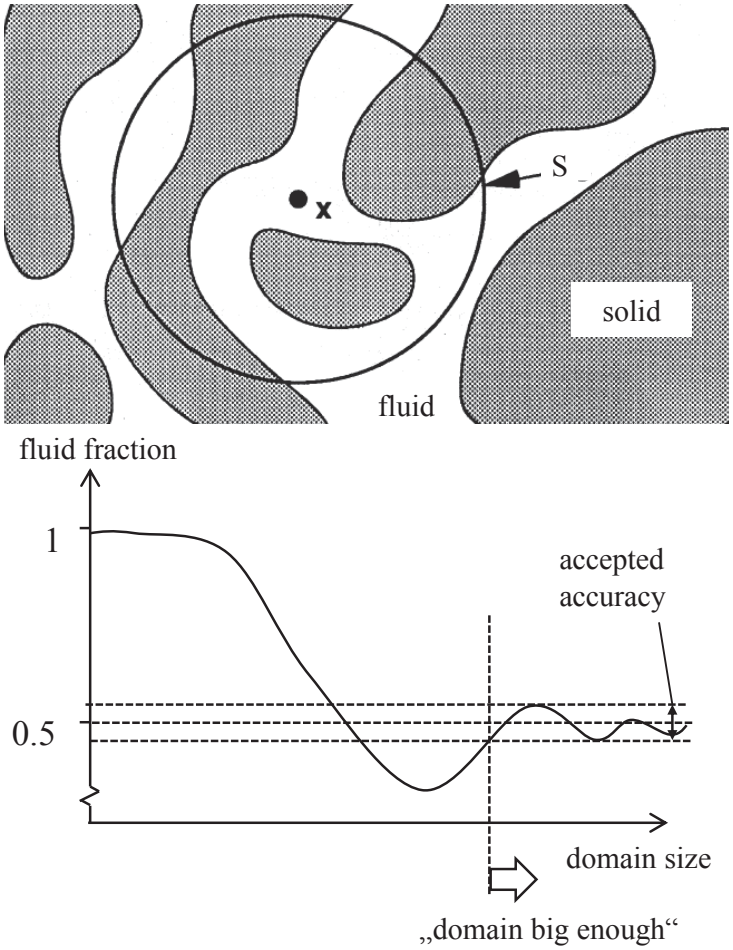

Figure. 2.1: Importance of domain size for volume averaging

The assumptions required for the derivation of Darcy's law have been investigated by Whitaker [6], Bear [7], Tucker [8] and Advani [4] and are summarized in the following:

- A representative volume, large enough to be acceptable for homogenization, can be defined inside the porous medium.

- Fluid and resin are incompressible.
- The solid phase is stationary.
- Fluid is Newtonian, i.e. viscosity is independent of shear rate.
- Surface effects between fluid and solid are neglected.
- Flow velocity is so that $Re < 1$ (Reynold Number).
- No mass exchange happens between fluid and solid phase.
- Flow front is sharply defined: No fluid is ahead of the flow front and there is complete saturation behind the flow front.
- Fluid viscosity is constant.

The assumptions arise from deriving Darcy's law mathematically rigorous. For real-world processes not all of the assumptions are realistic. Some researchers proved the validity of Darcy's law where violations of these assumptions exist. Pillai [9] showed the validity of Darcy's law for unsaturated flow.

For flow with Reynold number $Re > 1$, the Forchheimer equations can be employed [10], (p. 417):

$$-\nabla P = \frac{\mu}{K} v + \beta \rho v^2, \tag{2.5}$$

where β is the so-called non-Darcy coefficient of permeability.

For flow of resin inside fiber bundles and the required flow boundary condition at the solid-fluid interface, the Brinkman's equation can be employed [11]:

$$-\frac{\mu}{K} \cdot v + \mu' \nabla^2 v = \nabla P, \tag{2.6}$$

where μ' is an effective viscosity term.

Advani et al. [12] have reviewed literature and searched for flow situations that deviate from Darcy's law. For the following configurations, departures from Darcy's law may occur.

- Preforms containing layers with differing permeability
  The difference in permeability of two adjacent layers will lead to different flow velocities and hence to shear stresses which are transmitted through the fluid across the boundary, but Darcy's law does not represent momentum transport by shear.
- Viscoelastic fluid
  Studies have shown that for $De > 5$ (Deborah number) deviations from Darcy's law occur. This is somehow logical because the derivation of Darcy's law assumes the presence of a Newtonian fluid.

- Surface energy between fluid and the reinforcement surface
  It has been proven that the degree of saturation plays a significant role on evaluating permeability. Due to the fact that fiber bundles are no solids and have a certain packing density, flow within fiber bundles cannot be neglected.

The assumptions required for the derivation of Darcy's law state that the fiber bundles are impermeable and surface effects do not happen. In reality, fiber bundles are a porous medium as well as the pores and allow a certain flow. Figure 2.2 illustrates the phenomenon of dual scale flow. Depending on the surface energy between fibers and resin and depending on the injection pressure the dominant flow either takes place within the fiber bundles (Fig. 2.2, left) or in the channels between the fiber bundles (Fig. 2.2, right). Generally, high injection pressure will cause channel dominated flow as the channels create less resistance to the flow than the fiber bundles. Situations with slow flow front progression and low injection pressure will be dominated by flow in the fiber bundles because the capillary pressure due to the surface energy will play a more important role.

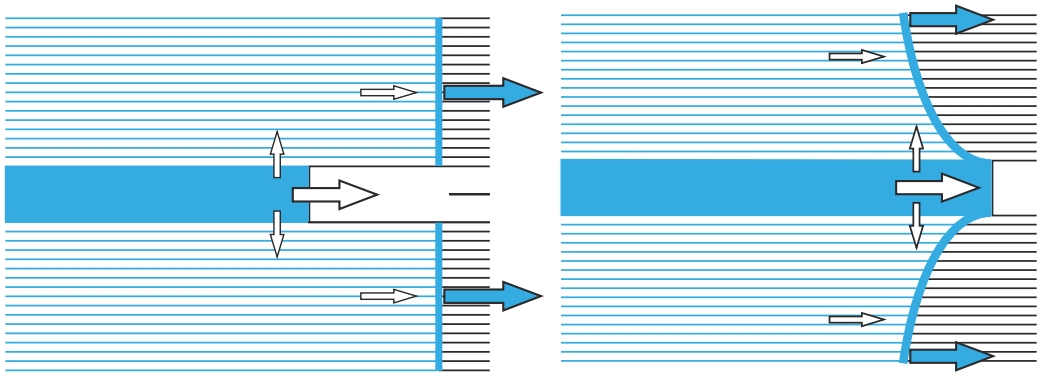

Figure. 2.2: Dual scale flow phenomenon, illustration from Binetruy [13]

The topic of flow in a dual scale porous medium has been investigated by many researchers. A recent work by Leclerc and Ruiz [14] gives a good literature review about previous research. The work also presents a practical approach to characterize void formation mechanisms and provides a scheme to determine the optimal injection speed (same flow velocity in channels and fiber bundles) based on the capillary number. There have also been studies focusing on the question how to implement the intra-bundles flow into simulation such as the works by Dimitrovova [15, 16] and Verleye [17].

2.2 Permeability

2.2.1 Definitions

Permeability as it is mentioned in Darcy's law is the most important fiber domain material property for RTM modeling. Bear [7] (p.119 ff) gives a concise description of the property denoted as permeability or hydraulic conductivity:

- Darcy's law, and hence permeability can only be applied when the porous medium is homogeneous (i.e. a property is independent of the position within this medium). This necessitates caution when averaging.
- For an isotropic porous medium, the permeability is a scalar property with unit $[m^2]$.
- For an anisotropic porous medium, permeability can be expressed as a symmetric 2^{nd} rank tensor [18] with positive values
- The permeability tensor can be diagonalized. For the 2D case it can be shown that permeabilities in the principal directions have the lowest and the highest values. In analogy to stress analysis, Mohr's circle [19] can be applied to derive the diagonalized form graphically.

In the two-dimensional context the quantity permeability can be nicely visualized. A flow experiment with experimental coordinate system 0°, 90° and 45° representing the test directions and central injection will result in a circular or elliptical flow front depending on whether the medium is iso- or anisotropic. Figure 2.3 illustrates an elliptic flow front in such a test coordinate system. The edge of the flow front represents the square root of the permeability. It becomes clear visually why the 1,1- and 2,2-entry in the diagonalized permeability tensor are the highest and lowest values of the tensor. The permeability in the 3D context can be visualized with an ellipsoid as Bear demonstrated [7] (p.144).

Gebart [20] and Weitzenboeck [21] have derived schemes to caluclate K_1 and K_2 for experimentally obtained permeabilities in independent directions: K_{0°, K_{45° and K_{90°. With the relation

$$tan^{-1}(x) = sin^{-1}\left(\frac{x}{\sqrt{1+x^2}}\right) \tag{2.7}$$

as it can be found e.g. in Papula's formulary [22] (p.102) the equations can be rearranged so that mathematical equivalence can be proved.

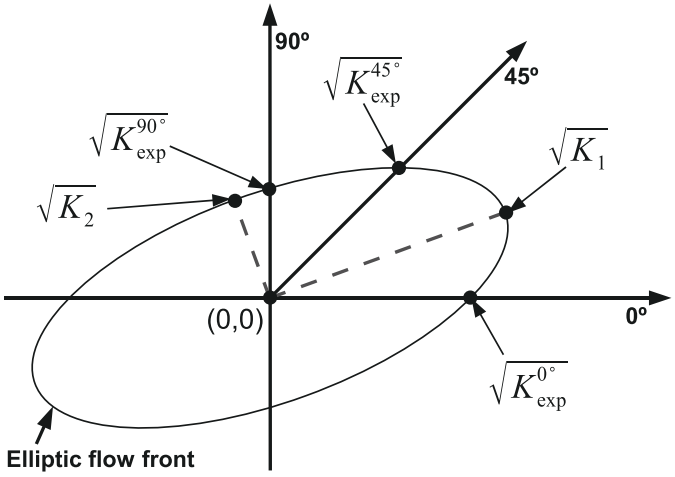

Figure. 2.3: Elliptic flow front pattern of the in-plane permeability tensor showing the effective permeabilities, illustration from Alms et al. [23]

2.2.2 Analytical Determination

Several researchers have investigated whether permeability can be determined analytically, and if so, how well. A commonly used approach dates back to 1977, where Kozeny introduced a relationship between permeability and V_f that was later modified by Carman and is today commonly denoted as the Kozeny-Carman equation:

$$K(V_f) = \frac{R^2}{4k} \frac{(1 - V_f)^3}{V_f^2}, \tag{2.8}$$

where k is the so-called Kozeny constant and R the filament radius. The origin of this equation is an analytic model to describe permeability of an idealized porous medium consisting of tortuous capillaries using the Hagen Poiseuille equation [24].

A summary of the validity and applicability of the Kozeny-Carman relation is given by Chapuis et al. [25]. Modifications of the Kozeny-Carman relation that account for the directionality of permeability are given by Gutowski [26] and Gebart [27]. Gutowski proposed different Kozeny constants with respect to the direction and Gebart proposed equations for parallel and transverse fluid flow in unidirectional reinforcements consisting of parallel and regularly packed fiber beds as can be seen in the following:

$$K_{parallel} = \frac{8R^2}{c} \frac{(1 - V_f)^3}{V_f^2} \tag{2.9}$$

$$K_{transverse} = C_1 \left(\sqrt{\frac{V_{f,max}}{V_f}} - 1 \right)^{\frac{5}{2}} R^2, \tag{2.10}$$

where the parameters C_1 and $V_{f,max}$ depend on the fiber arrangement (quadratic or hexagonal arrangement) and c depends on both fiber arrangement and the fiber volume fraction.

Based on the works by Gebart, Lundström [28] proposed a scheme to predict permeability particularly of NCFs. He came up with the result that small variations of the geometry change the permeability significantly. A more advanced approach based on the work of Lundström was proposed by Nordlund et al. [29]. He developed a global permeability model based on a meso-scale description of the fabric geometry and investigated the influence of scatter arising from fabric manufacturing using Monte Carlo simulations. He showed that variability of the fabric geometry affects global permeability but not as much as the stitching process. The importance of stitching will be addressed in that document later on.

Tran et al. [30, 31] proposed a more generic approach where mean-field homogenization techniques are used to predict the in-plane and out-of-plane permeability of fabrics. The prediction of the permeability tensor using their approach is error-prone especially for the misaligned UD fibers. However, the authors came up with the results that permeability of a reinforcement with dual scale porosity (macro pores between the fiber bundles and intra-bundle micro pores) can be predicted by this continuum approach and show good agreement with experimental results.

In conclusion, the relations discussed here provide a toolbox to estimate the permeability of a single layer of a unidirectional fabric. There are also approaches available to determine permeability of crimp fabrics such as weaves and braids. Due to the fact that this class of fabrics is not further investigated within this work, reference is given to research works having focused intensively on permeability prediction of woven fabrics such as Rieber for weaves [32] and Endruweit for braided preforms [33].

Permeability of Multi-Layer Preforms

To assess the permeability of a multi-layer preform, it is straight-forward to apply averaging, i.e. the rule of mixtures which is known from micromechanics. The thickness-weighted average can be written as:

$$K = \frac{1}{t} \sum_{i=1}^{n} t_i \cdot K_i, \tag{2.11}$$

where n is the number of layers and t_i and K_i are the thickness and the in-plane permeability of the layer i, respectively.

However, this approach neglects fluid flow and permeability in the thickness direction. To overcome this constraint, Calado and Advani [34] proposed a model where the transverse flow between adjacent layers is taken into account. The averaged in-plane permeability is a function of in-plane and through-thickness permeability of the individual layers, the thickness of each layer and the length of the mold. Studies on through-thickness flow have been conducted for 2-layer and 3-layer stacks and permeability results from the weighted averaging as well as from the published approach have been compared to simulations with *LIMS* [35], (cf. to Section 2.3) a FE-based simulation tool for mold filling. The approach presented always gives lower errors than the weighted average approach. A further advantage of the method presented is that the transverse apparent permeability can be deduced based on the in-plane permeability, the thickness and the average location of the flow front in the individual plies.

Chen and Liu [36] developed a description of the 3D permeability for multi-layer stacks based on a model for the interface layer derived from hydraulic radius theory. Two interface parameters, the tortuosity factor and the degree of overlapping were introduced. The results compared to experiments show good correlation for the best fit of the interface parameter, which is not necessarily physically based. The proposed model overestimates the influence of the stacking sequence compared to experiments.

Diallo et al. [37] performed an experimental study with stacks composed of high- and low-permeability fabrics, focusing on the influence of the stacking sequence and fluid flow rate. The results from experimental testing were used to derive the averaged in-plane permeability. However, the model requires the flow front progression along the thickness direction to be known which is rarely the case. Diallo et al. investigated the range of applicability of the weighted-average approach. Further, it was shown that the experimental results for 3D flow correlate well to simulation results obtained with RTMFLOT [38], a simulation tool for simulation of the RTM process (cf. to Section 2.3).

Adams et al. [39], [40] and Luce et al. [41] have conducted experiments on multilayer fiber reinforcements and proposed an analytical model. Parnas et al. [42] have developed a proposal for a standard reference fabric that allows calibrating measured permeability values

There are some experimental works published focusing on multilayer stacks of non-crimp fabrics such as the PhD thesis presented by Loendersloot [43] and results of a study by Elbouazzaoui et al. [44] who compared their results to a model proposed by Drapier [45]. Also works presented by Talvensaari et al. [46] and Groessing [47] take the effect of the number of layers into account.

In conclusion, the majority of the research has focused on the through-thickness flow arising from differences in in-plane permeability of the individual plies and on the nesting behavior. A comprehensive study on NCFs that presents a method to obtain the averaged in-plane permeability of a stack in a straightforward manner is currently not available. Additionally, there are not enough experimental studies that would allow derivation of an averaging scheme. Also factors that might be influential such as the cavity thickness and the areal weight of the fabrics used have not yet been investigated in depth.

2.2.3 Experimental Determination

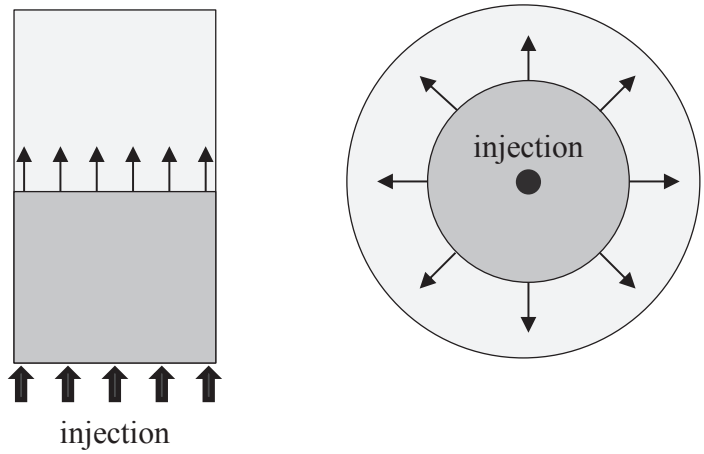

Figure. 2.4: Schematic of left 1D rectilinear (left) and 2D radial (right) permeability test setup

Permeability determination is necessary for prediction of process parameters such as fill time or required injection pressure. Together with analytical approaches, experimental determination of permeability is very common. There are numerous articles published focusing on experimental permeability testing. Parnas [48] and Gebart [20] conducted experiments to compare steady state and transient permeability testing using a rectilinear and a radial test setup. Lundstroem [49] presented a multi-cavity setup to reduce testing time for 1D measurement. The range of validity of Darcy's law has been investigated in depth as has already been shown in Section 2.2.1.

Between 2008 and 2010 an effort has been made to comprehend the existing knowledge about experimental testing through a benchmark study. This study was conducted with the principal goal of comparing results obtained with different test setups and to begin setting up a common standard. In 2011, results of the 1^{st} permeability benchmark exercise were published [50]. Eleven participants performed permeability experiments on two woven twill (2x2) fabrics, one comprised of carbon fibers and one of glass fibers. For this exercise, there were no restrictions, neither regarding the test method (1D or 2D), nor the measured property (flow rate or flow front progression) or the test fluid. It was discussed that the repeatability of the test procedure, especially all manual steps, are very prone to errors what is called human factor in the article. These factors lead to a very high scatter in the results.

Based on these results a guideline document for a 2^{nd} permeability benchmark exercise was created [23]. For this exercise, the following test boundary conditions were fixed:

- Test method has to be 1D.
- Measurement of flow front progression.
- Test fluid was to be silicone oil.

- Design aspects of the tool such as design of spacer plates or sealants.
- Injection pressure (1 *bar*).
- Number of repeats (10).
- Fixed evaluation procedure.

The experiments for the 2^{nd} permeability benchmark exercise at the Institute for Carbon Composites, have been conducted in winter 2011/2012. The results were published at the FPCM-11 and ICCM-19 conferences. In parallel, a paper detailing the results was prepared and published by Composites A [51].

In analogy to the 1^{st} permeability benchmark exercise, a woven fabric was distributed between the participants. For the permeability values measured in the given directions (K_{0°, K_{45° and K_{90°) there was a scatter between all participants of $\pm 18.9\%$ for K_{0°, using the least-square fit approach ($\pm 21.2\%$ for K_{45° and $\pm 20.1\%$ for K_{90°). When comparing the results after tensor diagonalization, the scatter is $\pm 19.7\%$ for K_1, $\pm 15.6\%$ for K_2 and $\pm 19.2\%$ for the rotation angle β. These results are a huge improvement compared to the first benchmark exercise where the scatter was significantly bigger [50]. Based on that results, there are ongoing efforts to standardize the proposed method for permeability testing.

So far, the two benchmark exercises have only investigated woven fabrics, however there is no evidence that reproducibility and robustness should be significantly lower for other types of textiles. Of course, the fabrics itself could be more or less heterogeneous. In the book by Lomov [52] (p.166ff), a summary of results from permeability experiments conducted on non-crimp fabrics is given.

2.3 LCM Process Modeling

2.3.1 Governing Equations

Tucker [8] (p.293ff) and Advani [4] (p.195ff) derived the governing equations for RTM with the focus of numerical implementation. From the most general forms, they simplified the equations using the scaling technique [53], i.e. defining characteristic values and plugging them into the governing equations. Computing all terms and comparing their orders of magnitude allows one to neglect certain terms.

The resulting equations for isothermal flow, not including chemical reactions such as cure, are documented in Section 2.1. A very good example is the decision whether a flow situation can be simplified to a 2D problem. Because through-thickness permeability is critical to measure on the one hand and on the other hand 3D flow simulations require significant numerical effort it is desired to simplify a flow problem to the 2D case whenever it is admissible. A decision criterion is given by Equation 2.12, its derivation is documented in Appendix A.1.

$$\frac{l \cdot K_z}{t \cdot K_x} \gg 1 \tag{2.12}$$

2.3.2 State of Research

The field of flow modeling has been a major focus in research over the last 20 years. Based on the initial contributions such as Trochu [38] or Bruschke [35], researchers have developed concepts to deal with typical questions arising from real-world manufacturing. Works by Liu [54] and Barandun [55] focused on the topic of injection strategy and modeling of the boundary conditions. For modeling of resin infusion, the coupled problem of flow and compaction has been addressed by Joubaud [56], Celle [57] and Govignon [58, 59]. Dual scale flow, impregnation of the space in and between fiber bundles, has been addressed by Ruiz [60] and Leclerc [14]. A topic that arises from manufacturing, called race-tracking, where the flow front is advancing a lot faster at the edges of a cavity compared to the interior has been investigated by Bickerton [61]. This phenomenon is not only a challenge for manufacturing but also for simulation because in a discretized model areas with high difference in permeability might cause numerical instabilities. High permeability gradients play an important role in modeling of through-thickness flow for resin infusion with a (high permeability) distribution layer.

2.3.3 Implementations and Available Tools

During the 1990s, research groups worked on implementing the governing equations for LCM into solvers and developed pre- and post-processing environments, such as RTMflot [38] or *LIMS* [35, 62]. Furthermore groups at ETH Zurich and the University of Auckland (UoA) have developed codes for LCM simulation, each with a special focus on certain processes such as SimLCM [63], developed at UoA, which is able to account for tool and fabric thickness deformation. Studies have been undertaken employing multi-purpose CFD solvers to model Darcy flow, such as Ansys Fluent [64]. Another tool that should be mentioned here due to its focus on fast RTM simulation is myRTM [65]. Here, an approach based on cellular automata has been used to model Darcy flow.

Today, there are few commercially-available tools, limited to PAM-RTM, originating from RTMflot, distributed by ESI and RTM-Worx developed by Polyworx [66, 67]. PAM-RTM can be considered as industry standard for its large functionality and because it is embedded into the ESI Composites Simulation Suite where simulation tools for draping simulation, crash simulation and deformation simulation are available.

2.4 Textile Modeling

2.4.1 Non-Crimp Fabrics

For structural components NCFs have become very popular for mainly two reason. One the one hand, the straight in-plane fiber orientation ensures very good mechanical properties as opposed to woven fabrics with an undulated fiber architecture that results in degradation of stiffness and strength. On the other hand, NCFs can be tailored to specific lay-up requirements by variation of areal weight, fiber orientation and stacking sequence. Both reasons together, explain the popularity of NCFs for series production of composites components. In recent years, the manufacturing speed of NCFs has been significantly increased mainly by developments in the machine technology. The book edited by Lomov [52] gives a concise description of the production of non-crimp fabrics. Figures 2.5 and 2.6 give an insight into up-to-date machine technology for manufacturing of NCFs. Figure 2.5 depicts an illustration of an entire warp knitting machine including the storage system for the fiber carrying bobbins.

Figure. 2.5: Warp knitting machine for manufacturing of non-crimp fabrics [68]

Figure 2.6 illustrates how the tows are spread and placed before stitching and winding up the fabric. The process of spreading is crucial as it determines the areal weight of the fabric and its local variability. In the following, the placed fiber layers are stitched together to allow handling of the fabric. The stitch pattern has a significant influence on the formability of the fabrics. Figure 2.7 gives an overview about the most common stitch patterns such as *franse* and *tricot*. Combinations of stitch patterns creates a variety of possible stitch patterns, details can be reviewed in [69].

Figure. 2.6: Fiber spreading and placement during NCF manufacturing [68]

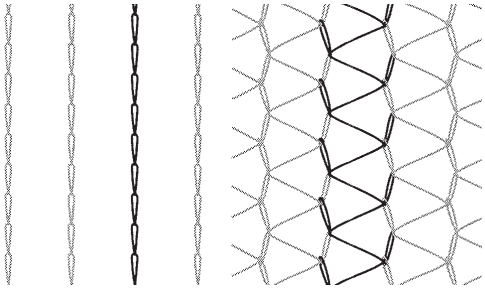

Figure. 2.7: Franse (left) and tricot (right) stitch pattern [52]

2.4.2 Geometry Modeling

For material modeling it is important to consider scale. Continuum mechanics, and hence the concept of homogeneous continuum can be applied at the micro-scale or the macro-scale. On the micro-scale, also denoted as the constituent level, models for the material's constituents are employed. In the context of this work, the micro level is defined as the domain of the filaments forming the fiber bundles and the resulting gaps (that will be filled during resin injection). On the macro-scale, the component level, composites are treated as anisotropic materials with its own homogenized measurable properties. The description of a material in another scale requires homogenization (micro- to macro-scale) or localization (macro- to micro-scale). It has always to be accounted for whether scale transformation is admissible, e.g. for homogenization the micro domain has to be chosen big enough to be be able represent macro properties. Both material descriptions have their pros and cons, cf. Aboudi [5](p.88ff). Very often, the decision of scale condenses to a conflict of two objectives: accuracy versus computational efficiency. For the presented work, the macro property permeability is strongly dependent on the micro-structure of the fiber domain. Thus, the following review focuses primarily on micromechanical models and its capabilities to predict in conjunction with homogenization the macro composite behavior.

The principal goal of micromechanics is to capture the material heterogeneity while allowing it to be treated as an effective (pseudo-homogeneous) continuum at a higher scale.

Micromechanics provides two approaches to describe a heterogeneous material, as can be seen in Figure 2.8. A material can either be modeled using the concept of representative volume elements (RVE), that characterizes materials with statistically homogeneous microstructure at an appropriate scale or using a representative unit cell model (RUC) that mimics periodic heterogeneous materials, see Drago [70].

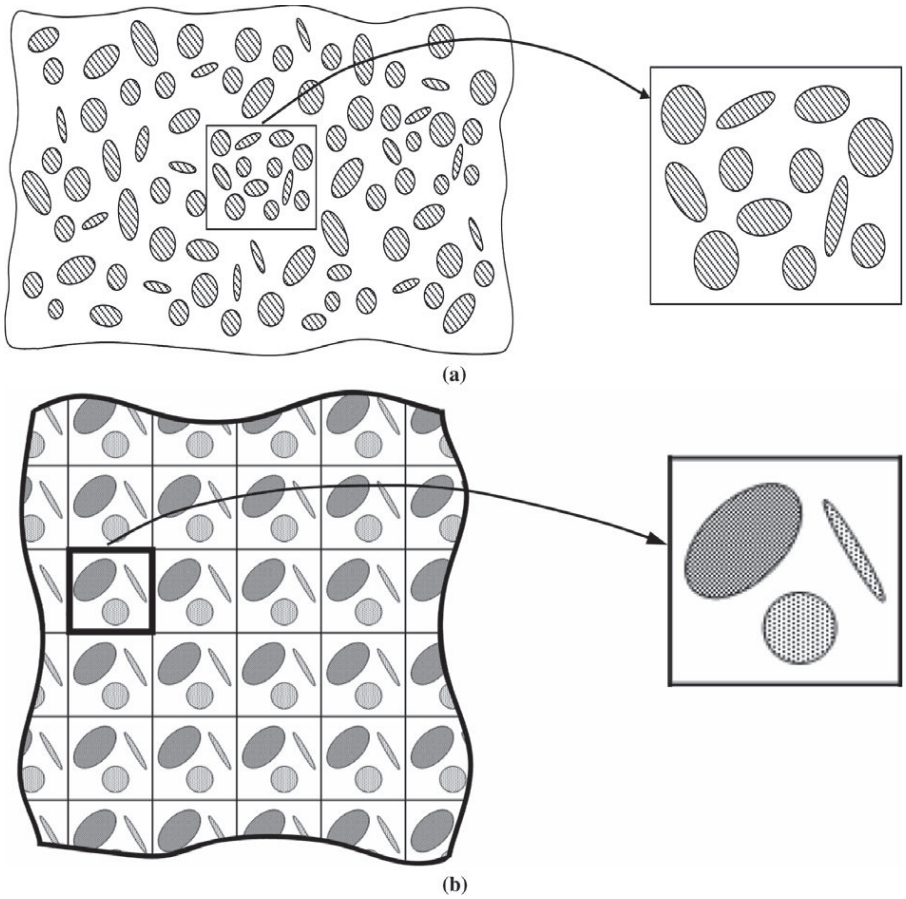

Figure. 2.8: RVE (a) versus RUC (b), illustration from Drago [70]

When considering NCFs, these fabrics have a periodic structure, however no unit cell exactly resembles another one. The gaps appearing almost black in Figure 2.9 have a high dimensional scatter. An accepted approach is to model fiber composites as RUCs [71], otherwise the RVE size would have to be defined for each batch of a material. If it is required, the heterogeneity of their features is taken into account by applying additionally stochastic analyses.

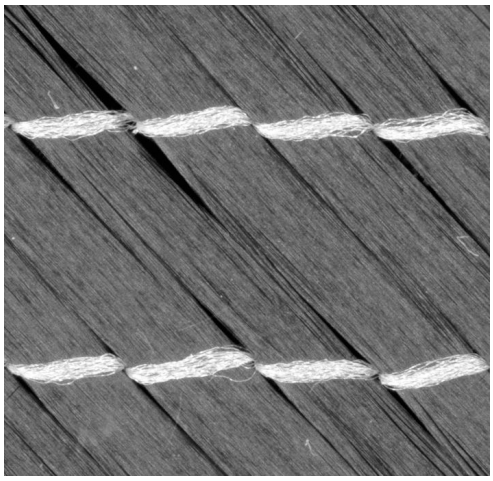

Figure. 2.9: Example scan of a NCF fabric

The idea of developing tools to model the internal geometry of a textile reinforcement has been followed by various researchers such as Lomov at al. who developed WiseTex [72] or Long et al. who developed TexGen [73]. Both tools implement a description of the internal structure of textile reinforcements on the unit cell level for a collection of fabric types. The motivation for geometry modeling is typically the prediction of fabric properties such as permeability or mechanical properties of a cured laminate [74].

Both tools, WiseTex and TexGen, include models for NCFs. Apart from technical details, they both have similar functionality. The geometrical model for NCFs incorporated in WiseTex [75, 52] is based on a cross-ply UD laminate distorted by the stitching as can be seen in Figure 2.10. The two constituents of the model, the unidirectional fiber layers and the stitching, are defined independent from each other. The way all fabrics are modeled within the WiseTex software is strictly hierarchical. I.e. based on the filament definitions, usually a filament of the reinforcing fiber and a polymeric filament for stitching, the yarns are defined. Moreover, a fabric is set-up entirely based on the yarn definitions, hence commonly fiber and stitch yarn. This hierarchical structure will simplify the procedure of defining an XML structure for the fabrics using tags, sub-tags etc. presented in Chapter 4.

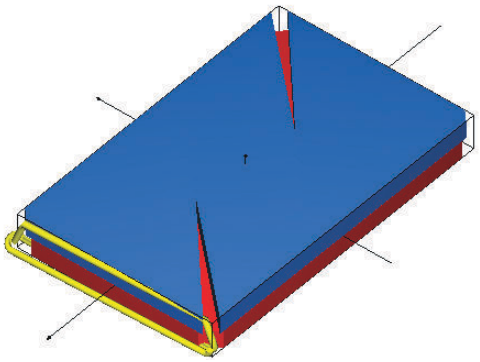

Figure. 2.10: Stitched mat model created, using WiseTex [72]

Defining the fiber domain sets following parameters of the model:

- Fiber orientation
- Fabric thickness
  (by the definition of V_f resulting from filament diameter, linear density, packing density and fiber material density)

To that extent, the structure of the stitched mat model is equal to that of a more simple model, namely that of a unidirectional ply. The definition of the stitching (Fig. 2.11) creates the stitched mat model. The stitching is based on principles of warp knitting, a detailed introduction of which can be found in [69]. The type of the stitching is defined using a code system, the so-called Leicester notation. The definition of the stitch yarns is equal to a standard WiseTex yarn definition. In addition to the stitch type, the dimensions of the stitching can be defined. The definition of the stitch domain sets the following fabrics properties:

- Size of the unit cell
  (by defining the distance between stitching, stitch type and stitch loop dimensions)
- Dimensions of the gaps.

For detailed information about the hierarchy behind fabric modeling in WiseTex, the reader is referred to the *Computational Models, Methods and Algorithms* guide of WiseTex [76].

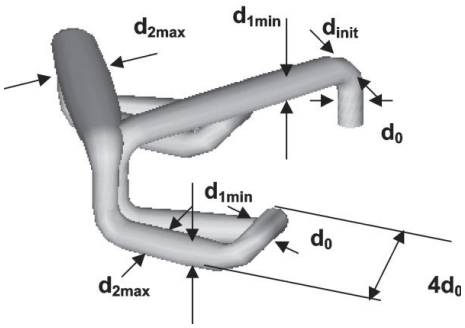

Figure. 2.11: Stitching

A collection of papers by Lomov et al. show a complete set of applications of modeling and experimental characterization of multiaxial multiply stitched preforms:

- Geometry of the preform [75]
- KES-F characterization of the deformability of the preforms at low loads [77]
- Biaxial tension, picture frame and compression tests of the preforms [78]
- Mechanical properties of composites and damage observation [79]
- Geometry of sheared biaxial fabrics. [80]

- Fatigue behavior at low loads: Stiffness degradation and damage development [81]

Unit cell modeling provides an averaged description of a fabric. As all fabrics are heterogeneous, research has been undertaken to study local variability and its effect on global properties, such as Guilleminot et al. [82]. Research with a detailed focus on NCFs and permeability has been presented amongst others by Loendersloot [80] who investigated the gap size and distribution of NCFs. Zhang et al. [83] set-up a stochastic description of permeability for a chopped strand mat.

2.4.3 Permeability Modeling

Textile modeling with a particular focus on permeability determination has been studied by Beavers [84] who investigated the flow at the bounds between a flow channel and a permeable porous medium compared to an impermeable solid. Prediction of permeability based on fabric geometry models has been investigated amongst others by Delerue [85], Belov [86], Wong [87] [88] and Verleye [89].

Most straightforward approach is to set-up a model based on the unit-cell internal geometry description that distinguishes between solid (impermeable) and fluid domains. A more advanced approach takes the intra-yarn flow into account modeling Stokes flow in the fluid domain, Darcy flow in the fiber domain and coupling it with Brinkmann equation.

A recent paper by Verleye et al. [90] compares two concepts of permeability modeling. One method is based on a finite difference discretization of a 3D unit cell and solving the Stokes equations. The second method computes a 2D approximation of the fluid flow. The results have been compared with respect to computational efficiency, where the simplified 2D approach proved its benefits. A comparison to experimental tests was not undertaken.

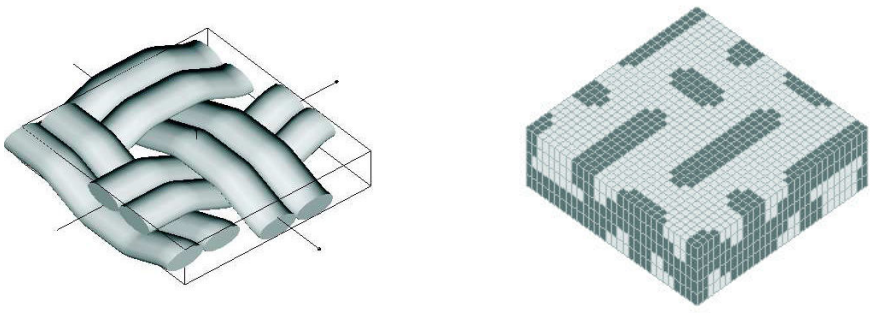

Figure. 2.12: WiseTex model of a woven fabric (left) and illustration of respective voxel file (right)

Figure 2.12 depicts a woven fabrics modeled in WiseTex and an illustration of the respective voxel file as it can be processed by FlowTex. Voxel files can be represented using text files, an example is given by Figure 2.13 where the actual voxel file text is depicted on the left and explanations are given on the right. The voxel model presented in Figure 2.13 neglects intra-yarn flow because the fiber domain is modeled using impermeable solid voxels denoted as `S`. Models in FlowTex accounting for intra-yarn flow use Brinkmann point

instead which are denoted as `B` followed by string of nine tensor entries specifying size and orientation of the permeability tensor of the yarn domain, as can be seen in Figure 2.14.

`Biaxial`	Model name
`0.03`	Voxel dimension $[mm]$ in x-/y-/z-direction
`0.03`	
`0.0124`	
`106`	Number of voxels $[-]$ in x-/y-/z-direction
`169`	
`24`	
`FFFFSSSSSFFFFFFFFFFF[...]`	Voxel description: solid `S` and fluid `F`
`53.91`	V_f [%] estimated by the lattice
`50.31`	V_f [%] given by WiseTex
`7.52`	ϕ [%] estimated by the lattice
`9.04`	ϕ [%] given by WiseTex

Figure. 2.13: Voxel file (left) and explanatory comments (right)

```
B 1.22E-009 2.51E-011 -1.70E-009 2.51E-011 8.24E-011
-3.76E-011 -1.70E-009 -3.76E-011 2.63E-009
```

Figure. 2.14: Textstring of a voxel file representing a Brinkmann point

2.5 Digital Image Processing

In this section the state of research in the field of digital image processing is reviewed. The main focus is to assess techniques that allow information to be extracted from images depicting carbon fiber fabrics so that a fabric model can be set-up.

2.5.1 Definitions

Following the definition in the textbook of Gonzalez and Woods [91], a digital gray-level image is composed of a 2D function, $f(x,y)$, where x and y are spatial coordinates and f is the intensity (gray level) at each pair of coordinates. An image may by called digital image when the intensity values are discrete quantities, e.g. 256 gray-levels for an 8bit gray-level image. Color images can also be defined according to this definition with the adding that each color channel such as red, green, blue for the RGB model or cyan, magenta, yellow and key (black) for the CMYK color model require a 2D level function on its own and the colors of the image are based on superimposing the color channels. For the thesis at hand, the focus will be merely on gray-level images because all relevant image content can be segmented and analyzed based on the gray-level or intensity. Processing of color

images would be nothing but applying the same features but on multiple color domains resulting in enhanced computational cost.

There is no clear-cut boundary of the expression *digital image processing*. A useful distinction is given by Gonzalez and Woods [91] who distinguish between low-, mid- and high-level processes and define *digital image processing* to comprise low- and mid-level processes.

- The input and output of a *low-level process* are images. Such processes involve operations such as noise reduction, contrast enhancement or sharpening which are commonly used to pre-process images.
- The input of a *mid-level process* is an image, the output are attributes extracted from the image. Tasks are employed to segment an image, e.g. dividing it into certain objects of interest, describe those objects and classify them.
- *Higher-level processing* includes bringing a 'sense' to the recognized objects.

Everything that goes beyond finding the 'sense' in an image belongs to the domain of image analysis and computer vision which will not be addressed in that thesis.

2.5.2 Methods

Gonzales and Woods [91, 92] reviewed existing concepts, methods and algorithms. The methods reviewed in this section can be classified into two parts *Image Segmentation* and *Image Domain Analysis*.

Image Segmentation

Segmentation is a pre-processing step where images are split into certain areas of interest. For instance, algorithms to evaluate fiber orientation will only work properly when they are applied to pixels representing fibers.

Gray-level thresholding - The most straightforward approach to segmentation is gray-level thresholding. Figure 2.15 (left) shows a gray-level histogram plotting gray-levels occurences in an image. Gray-level thresholding is simply defining one or two gray-level bounds and denoting the pixels that are outside or within this limit as belonging to the desired domain. Based on this scheme, Otsu [93] developed an optimization scheme to compute the gray-level bound so that the between-domain variance is maximized and the within-domain variance is minimized. An example application of the scheme developed by Otsu is depicted in Figure 2.15 (right).

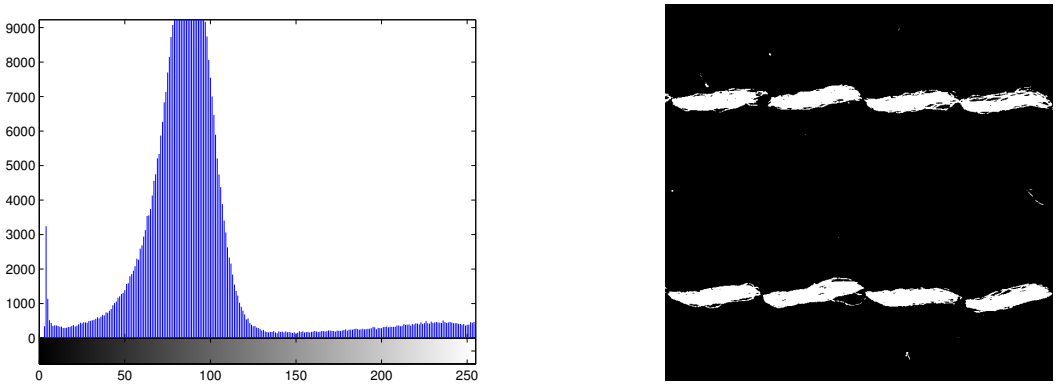

Figure. 2.15: Gray-level histogram (left) and resulting binary image after Otsu graylevel-thresholding (right) applied to Figure 2.9

Segmentation using gray-level thresholding does not account for geometric details but is acting on global properties. In order to segment local features more accurately, morphological operations can be employed.

Mathematical morphology - Mathematical morphology is a technique for the analysis and processing of geometrical structures, based on lattice theory and random functions, introduced by Jean Serra [94]. Two functions, *erosion* and *dilatation*, form the basis of this discipline. Erosion and dilatation are the core operations based on which many other operations are derived such as opening, closing or the Hit-and-Miss transformation for shape detection.

With A being an image in the two-dimensional space with elements z and pixel coordinates $z(x,y)$ dilatation of A by B is denoted as:

$$A \ominus B = \left\{ z \mid (\widehat{B})_z \cap A \neq \emptyset \right\}, \tag{2.13}$$

where $\emptyset$ is the empty set and B is the structuring element.

Erosion of A by B is denoted as:

$$A \oplus B = \left\{ z \mid (\widehat{B})_z \cap A^c = \emptyset \right\}, \tag{2.14}$$

where $A^c = \{z \mid w \notin A\}$ is the complement of A.

An illustration of both operations is given by Figure 2.16.

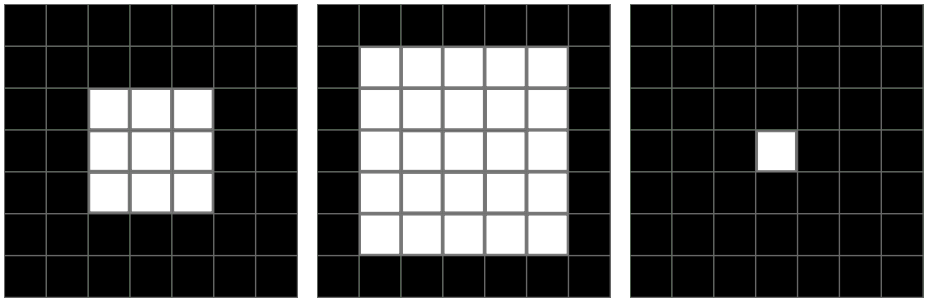

Figure. 2.16: Original image with a 3x3 block (left), image after dilation (center) and image after erosion (right)

Every morphological operation requires a structuring element. For the examples in Figure 2.16, an element of type *square* 3 by 3 was employed. With this matrix the original images were sampled and the morphed image was created.

By varying the shape and size of the structuring element, the morphed image could be manipulated. Figure 2.17 shows structuring elements of various shapes.

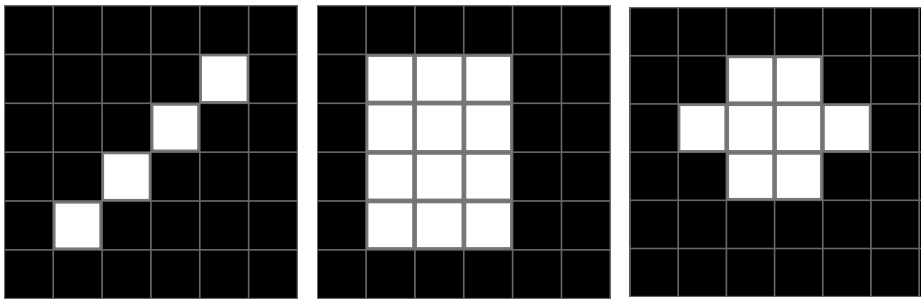

Figure. 2.17: Examples of structuring elements: line (left), rectangle (center) and diamond (right)

Watershed segmentation - Pixels of a gray-level image are assigned to a certain level depending on their gray-level. Watershed segmentation [95] is especially suited for the segmentation of overlapping bodies. Figure 2.18 shows two ellipse shaped areas that overlap each other.

Starting from the edges to the center points, level information can be assigned. The further the distance from a point to the edge the lower is the level. The mode of operation of a watershed algorithm can be imagined as filling the valleys of the level image with water. The place where the two waterfronts meet can be considered as the division line.

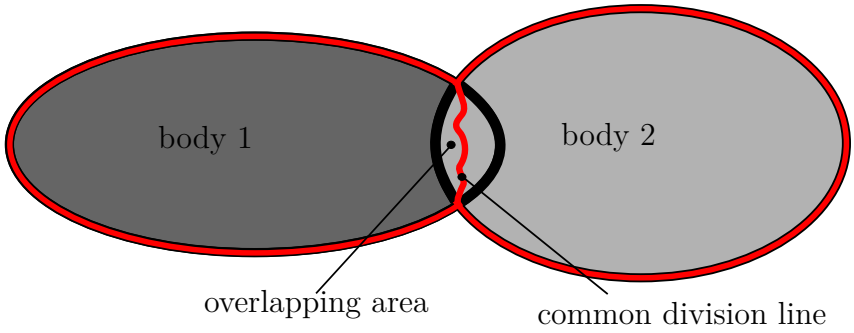

Figure. 2.18: Overlapping ellipses

Second order statistics and texture analysis - First order statistics, such as gray-level thresholding, considers every pixel independently. First order information is simple and fast to compute, however it doesn't take into account any information about space. If the input is an 8 by 8 pixel gray-level image, the result is exactly the same. Second order statistics are properties that involve at least 2 pixels and allow the evaluation of spatial properties, e.g. what the human eyes considers as textures.

Jean Serra presented the mathematical morphology, in particular the texture analysis [96]. Haralick has published a summary of available texture features [97]. The works published by Mostaco-Guidolin et al. [98] and Oliveira et al. [99] show how texture analysis can be applied in medical engineering.

Second order statistics are based on the gray-level co-occurrence matrix (GLCM). The GLCM is constructed from a gray-level image by a process requiring the definition of a displacement vector (direction and length).

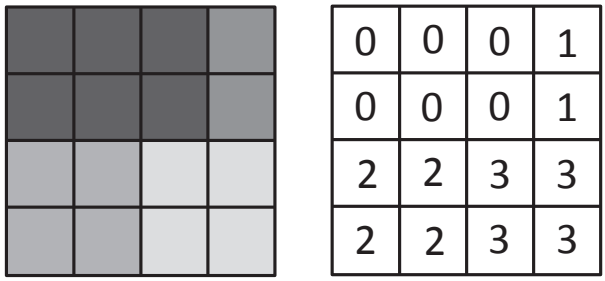

Figure. 2.19: Gray-level image depicted in image format (left) and matrix notation (right)

$GLCM(i,j)$ $[x\ y]$ is the probability to find a pixel pair whose gray-levels are i and j (i is the gray-level of the origin pixel and j of the destination pixel) and the distance from i to j can be described with the definite vector $[x\ y]$.

Figure 2.19 depicts a digital gray-level image (left) and its matrix notation (right), Figure 2.20 shows the gray-level image (left) and its gray level co-occurrence matrix (right) derived with a displacement vector of [0 1]. Generally, the vector can be arbitrarily chosen, the vector here suggests that a pixel is compared to the one right of it. In Figure 2.20 two entries of the GLCM are investigated exemplarily. The top left entry contains the number of occurrences of gray level 0 in a pixel and the same value in the pixel right

of it. This occurs four times in the matrix in Figure 2.20 (left). The fourth entry in line three hence denotes the occurrences (two) of a jump from gray level 2 to gray level 3 which is also marked in the matrix in Figure 2.20 (left).

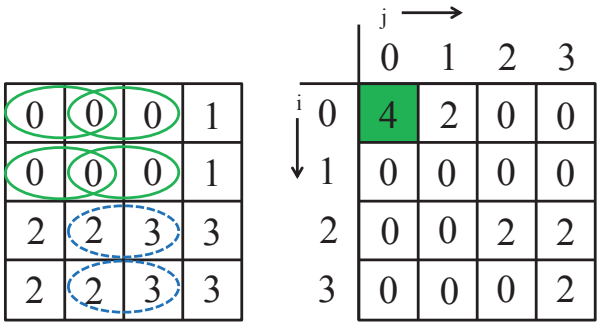

Figure. 2.20: Gray-level image in matrix format (left) and its gray-level co-occurence matrix (right)

Having the GLCM at hand for a certain image, one can employ texture features such as contrast, entropy, energy etc. (cf. Haralick [97]) to segment image areas that are represented by different textures.

Image Domain Analysis

Fourier transformation - Fourier transformation has been applied by Nishimura [100], Marquez [101] amongst others to measure fiber orientation from images of fibers. The principle has been explained by Richard Alan Peters [102], and is summarized here.

Let $f(x,y)$ for $x = 0,1,2,\ldots,M-1$ and $y = 0,1,2,\ldots,N-1$ denote a digital image of size $M \times N$. The 2D Discrete Fourier transformation (DFT) of $f(x,y)$ denoted by $F(u,v)$, is given by:

$$F(u,v) = \sum_{x=0}^{M-1} \sum_{y=0}^{N-1} f(x,y) e^{-j2\pi(\frac{ux}{M}+\frac{vy}{N})}, \tag{2.15}$$

for $u = 0,1,2,\ldots,M-1$ and $v = 0,1,2,\ldots,N-1$.

Letting $R(u,v)$ and $I(u,v)$ represent the real and imaginary part of $F(u,v)$, the Fourier spectrum is defined as:

$$|F(u,v)| = \left[R^2(u,v) + I^2(u,v))\right]. \tag{2.16}$$

The complex function $F(u,v)$ can be expressed in polar form as:

$$F(u,v) = |F(u,v)|\, e^{j\phi(u,v)}, \tag{2.17}$$

with the phase angle $\phi(u,v) = arctan\left[\frac{I(u,v)}{R(u,v)}\right]$.

Fiber orientations can be extracted by searching for the highest Fourier coefficients in the Fourier spectrum. Figure 2.21 (left) presents an example image that was created with edges aligned purely in the 45° direction and Figure 2.21 (right) shows its Fourier spectrum. Applying further filtering techniques and applying curve fitting (see following section) can be used to extract the edge orientation from an edge image.

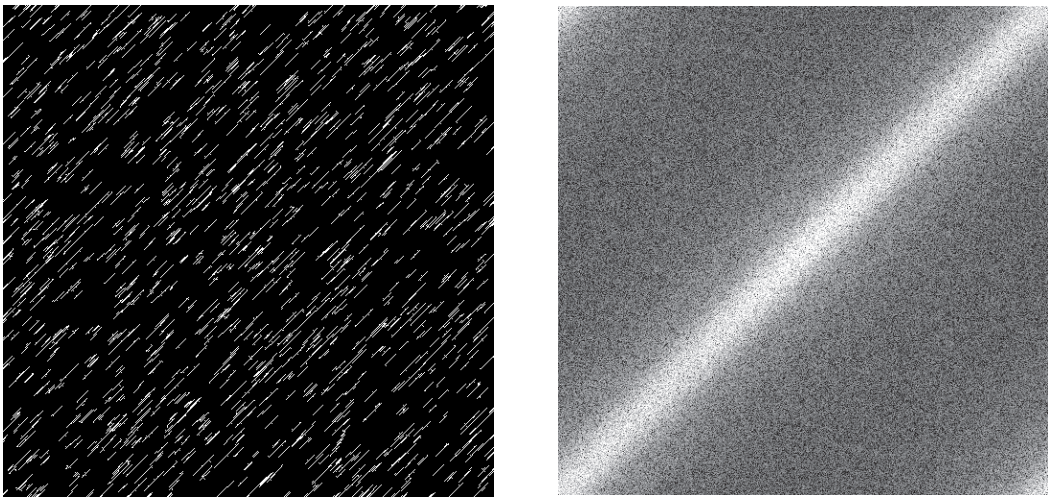

Figure. 2.21: Image with 45° edges (left) and its Fourier spectrum (right)

Edge detection - Humans recognize features in images commonly by difference in brightness. Smooth changes are recognized continuously whereas abrupt changes are recognized as edges. A powerful scheme for edge detection was proposed by Canny [103]. An example of edge detection is given in Figure 2.22.

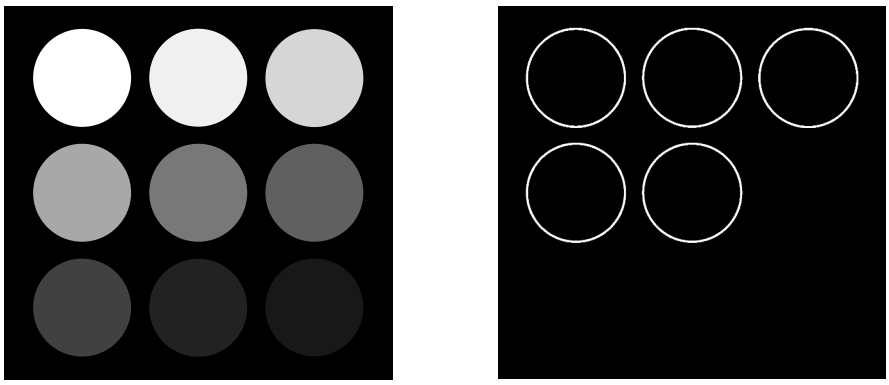

Figure. 2.22: Image with circles of different gray levels (left) image after edge detection (right)

Curve fitting - After segmentation, binary images stored into matrices can be interpreted as coordinates. Figure 2.23 demonstrates how a straight line can be obtained using a least squares approach.

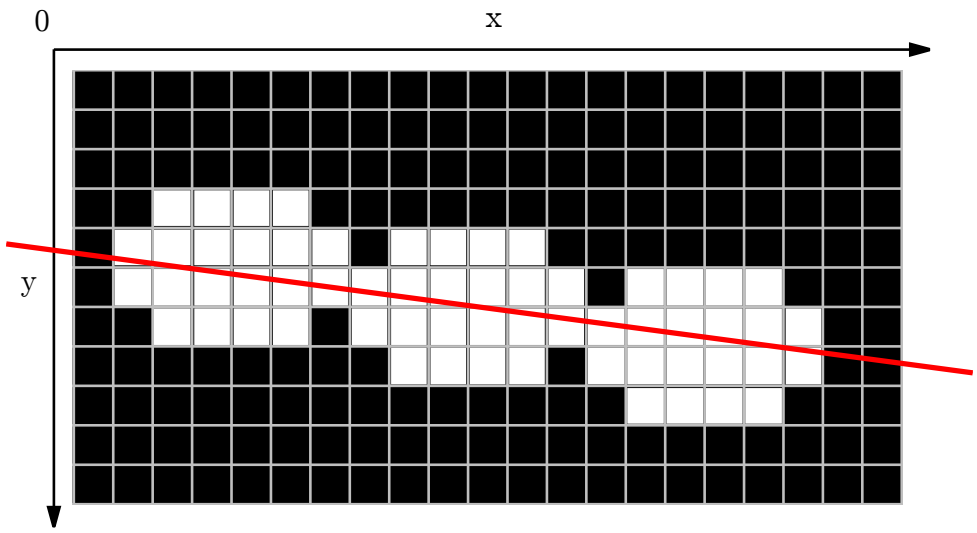

Figure. 2.23: Curve fitting using least square approach

2.5.3 Applications

Digital image processing is applied in various fields of engineering, natural science and computer science. The most important applications in composites engineering are quality inspection as performed by Trias [71] and Tsai [104] or quantifying variability by Vanaerschot [105] and Zhang [83].

Applications to Quality Inspection

Quality assurance using image processing developed at FIBRE - The Faserinstitut Bremen (FIBRE) has developed a tool for determination of orientations (mostly of fibers) in digital images using Fourier transformation [106]. Examples depicted in Figure 2.24 and 2.25 demonstrate that even the detection of large gaps, fish eyes and foreign particles is possible by evaluating heterogeneities in fiber orientation. Feature extraction purely based on orientation also has its drawbacks because not every image has an oriented texture, as can be seen in Figure 2.9.

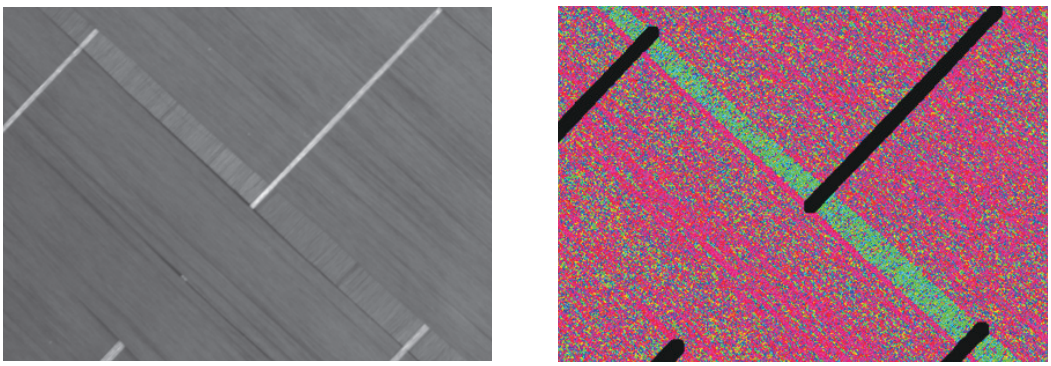

Figure. 2.24: Gaps detected in a gray-level image (left) by difference in fiber orientation using Fourier transformation (right), taken from [107]

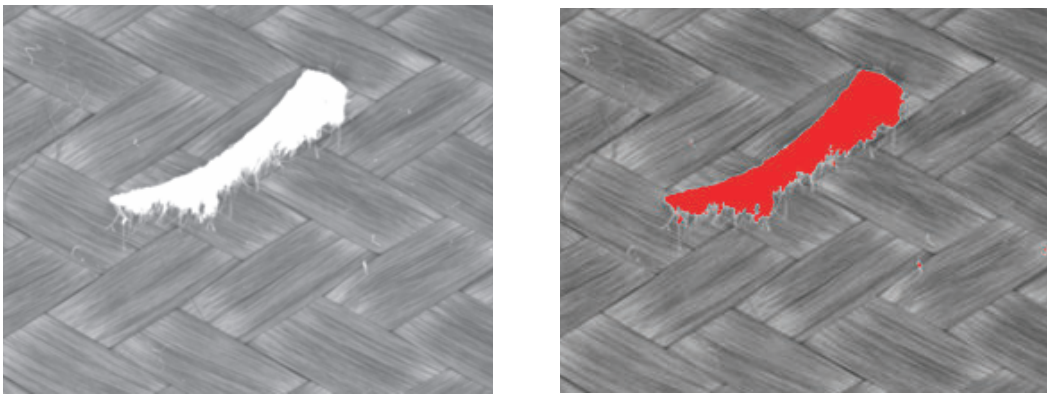

Figure. 2.25: Foreign particle detected by anomalies in fiber orientation, taken from [107]

Determination of fiber orientation using ProFactor sensor - ProFactor GmbH in Steyr, Austria has developed a sensor to detect fiber orientation [108]. The sensor, depicted in Fig 2.26, can be handled manually or on a robot arm and is particularly suited for use in a production environment. Also, the software performance is very robust, a result is obtained for any scan, however adjustments to the software are not possible and a measure of the result quality is not implemented.

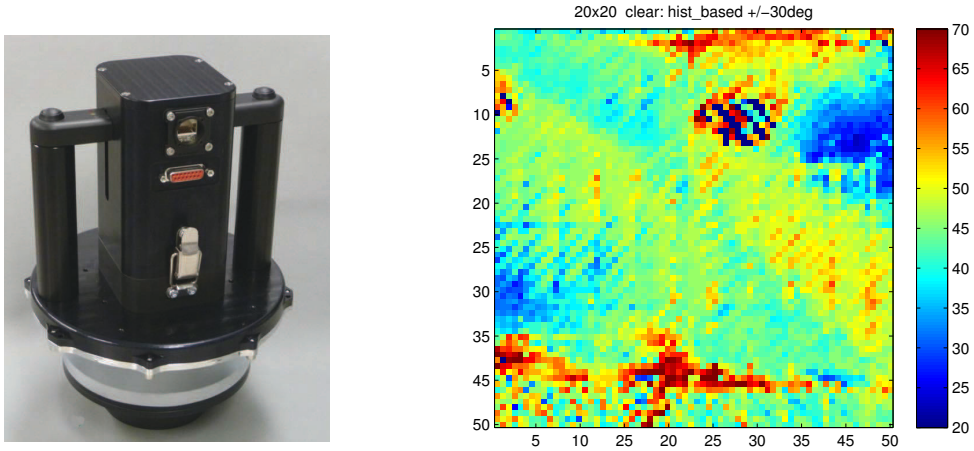

Figure. 2.26: ProFactor sensor (left) and fiber orientation plot (right)

In addition to the two examples presented in detail there are more research institutes and companies working on that field such as Automation W+R and GOM.

Applications for Image Processing as Input for Simulation

Frishfelds et al. [109] developed the idea to extract averaged data from scanned images. The use of this information for determination of permeability has been mentioned in the title but hasn't been followed in the paper.

Zhang et al. [83] applied statistical modeling on digital gray-level images of a chopped strand mat manufactured by Owens Corning (M705-450) composed of E-glass fibers. The images were acquired using a light box device where samples were placed on a transparent plate and illuminated from behind. For the technique transmitted light is correlated with the local variations of areal weight and hence permeability. Direct application of the method to carbon fibers is not possible due to their limited light transmitting capabilities.

3 Experimental Permeability Tests

Chapter 3 summarizes all results from experimental permeability testing that are relevant for this project. Chapter 3.1 will introduce the employed test setup starting with a hardware description followed by an introduction of the sensor concept and evaluation methodology. Chapter 3.2 presents experimental results from the contribution to the 2^{nd} permeability benchmark exercise and Chapter 3.3 presents the results of a comprehensive parameter study conducted for two NCFs.

3.1 LCC Testing Facility

The LCC employs a 1D test setup for permeability testing comprised of four cavities that can be operated simultaneously. The cavity thickness can be adjusted using distance frames ranging from $0.25\,mm$ to $4.80\,mm$. The test setup may be used for both transient and steady state permeability testing. Result evaluation is executed by a data management software, developed in-house.

The permeability test setup at LCC in its current stage was a joint development between colleagues, mostly Swen Zaremba and Reinhold Meier. The work was supported by several students undertaking term papers or diploma thesis projects. Their contributions will be referenced at the respective locations within this chapter. A complete list of supervised student projects can be found in the Appendix.

3.1.1 Hardware

Figure 3.1 depicts an overview of the four cavities and in Figure 3.2 a top view of the permeability test setup is shown. The top and bottom mold halves were manufactured from aluminum *AlZnMgCu1,5* and have a thickness of 45 mm each. The distance frames were grinded from steel plates (unless the desired thickness was available from a retailer) and then laser cut to its final dimensions including bore holes. The injection gate was positioned on the bottom mold and has a channel shape to ensure that the fluid arrives at the entire fabric edge simultaneously. The outlet is manufactured the same way but in the top mold, to ensure that air is removed from the cavity before the fluid starts to exit the mold. The four cavities are used to perform four 1D measurements in parallel which results in speed-up compared to operating a single cavity. Originally, a four cavity setup was proposed by Gebart and Lidstroem [20] with the core idea to obtain an in-plane permeability tensor within one experiment (requiring three cavities) and to have additionally the reference to a material with well known permeability (fourth cavity) for obtaining a measure of quality.

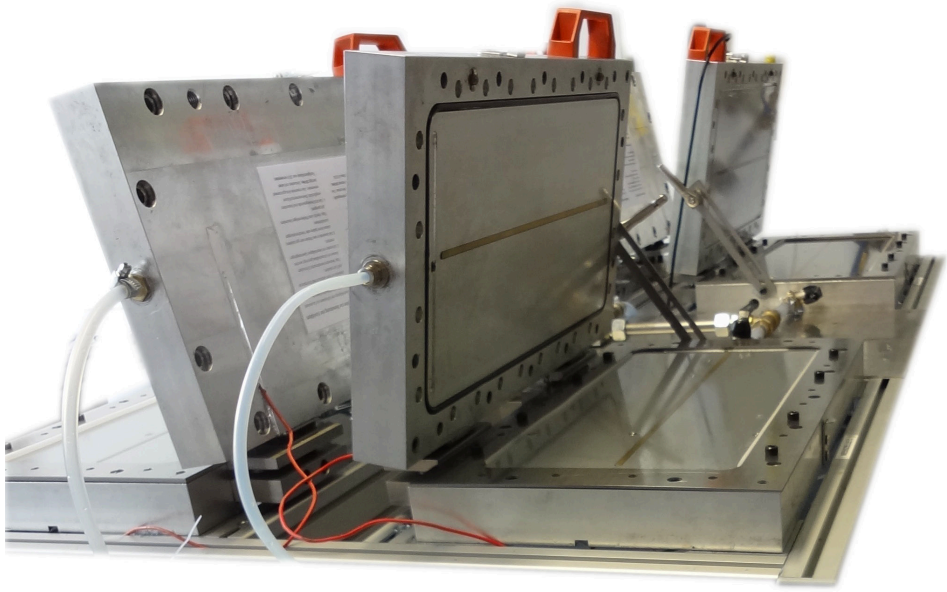

Figure. 3.1: Permeability testing facility at LCC

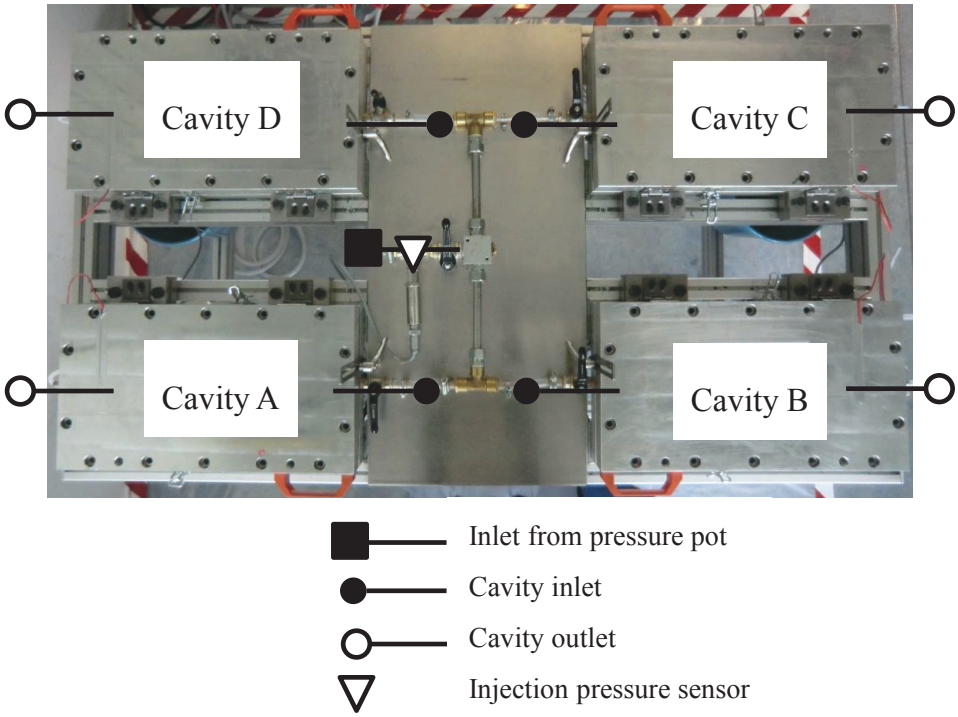

Figure. 3.2: Overview of the 4-cavity setup at LCC

Deflection test
Permeability is very sensitive to variations of V_f, as stated by Kozeny-Carman relation in Section 2.2.1. To account for mold deformation and its influence on fiber volume fraction V_f and hence permeability, a deflection test was conducted by applying an optical 3D deformation analysis with a GOM ARAMIS-4M during a test run. A finite element analysis (FEA) was considered for deformation prediction but finally was omitted because of too many unknowns such as boundary conditions and the change of compaction response from dry to impregnated.

A speckled pattern measuring 141 mm x 100 mm was applied to the mold as can be seen in Figure 3.3, covering the area where the biggest deflections will occur. The Figure shows three sections (*sec 0*, *sec 1* and *sec 2*) and four positions (Pos 1, Pos 2, Pos 3 and Pos 4). At each intersection, deflections were evaluated over time during the test run. Furthermore, Figure 3.3 depicts the pressure sensors installed in the cavity denoted as P2, P4 and P5 that are used to detect advancing flow fronts and additionally the pressure sensors RT1 and RT2 that are installed at the boundaries of the cavity in order to detect overshooting flow fronts close to the edges, denoted as race-tracking.

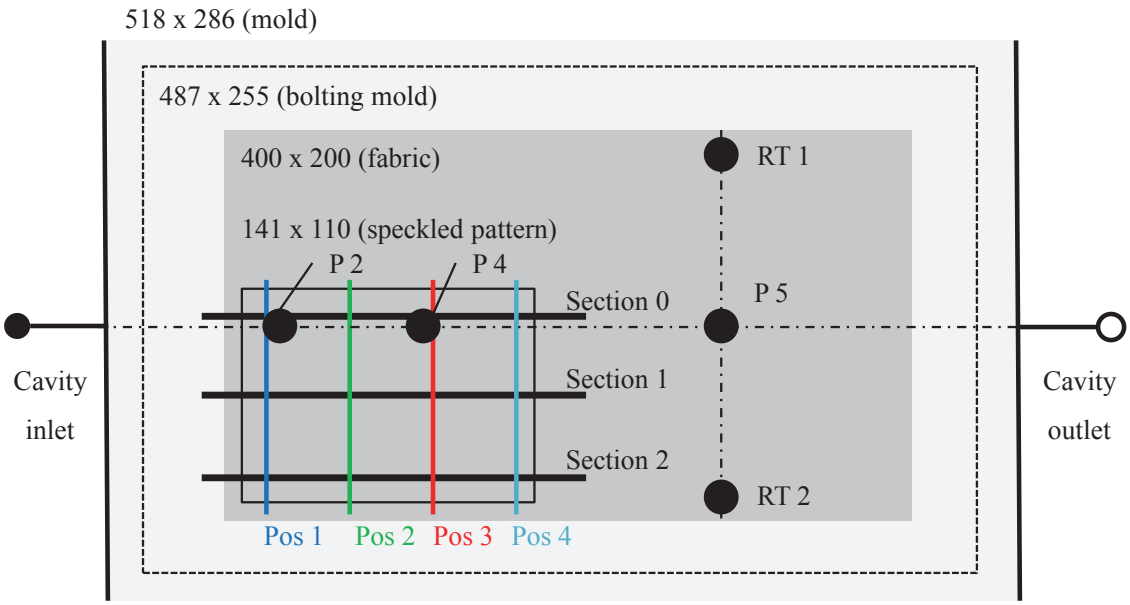

Figure. 3.3: Sketch of mold dimensions and position of speckled pattern

Parameters such as injection pressure p_{inj} and V_f were chosen so as to achieve maximum deformations. For this test, the following conditions were used:

- Fabric:
  - Biax Saertex (SAE540)
    (same fabric used as for experimental testing in Section 3.3)
  - Areal weight $540 g/m^2$
  - Cavity thickness $t = 4mm$, 8 layers: $\rightarrow V_f = 61\%$

- Compaction response (Walbran [110])
  - Dry (long term) compaction response of the fabric:
    $p_{compact} = 90kPa$ @ $V_f = 60\%$
    $p_{compact} = 35kPa$ @ $V_f = 52.5\%$
  - Saturated compaction stress is $10 - 15\%$ lower than dry
- Injection pressure: $p_{inj} = 3\,bar$

At the start of injection ($t = 434s$), the deflections were normalized to $0mm$. Therefore, only the deflections due to the applied injection pressure were taken into account. Figures 3.4, 3.5 and 3.6 show the actual deflection results:

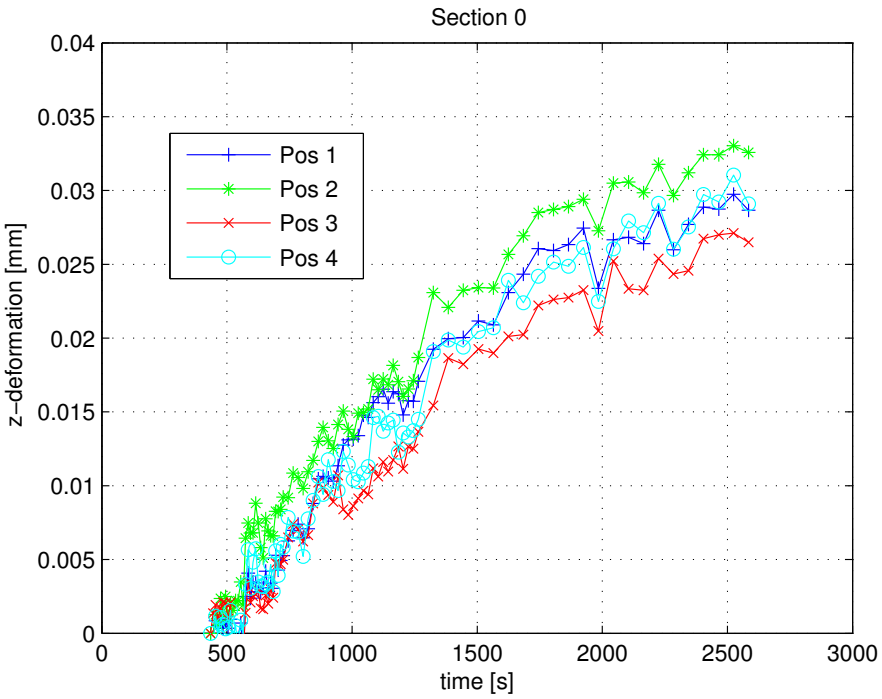

Figure. 3.4: Deflection over time - Section 0

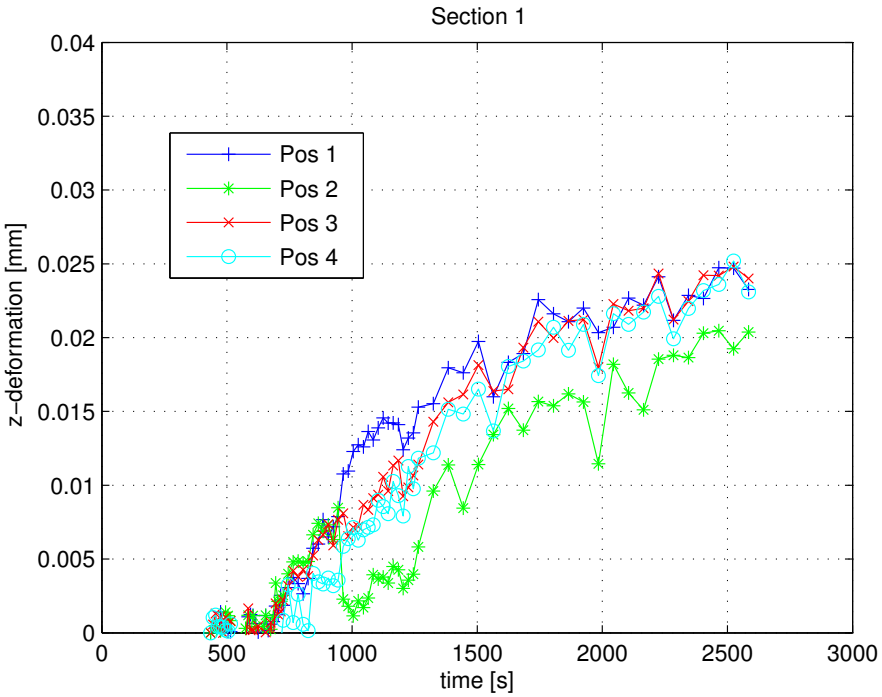

Figure. 3.5: Deflection over time - Section 1

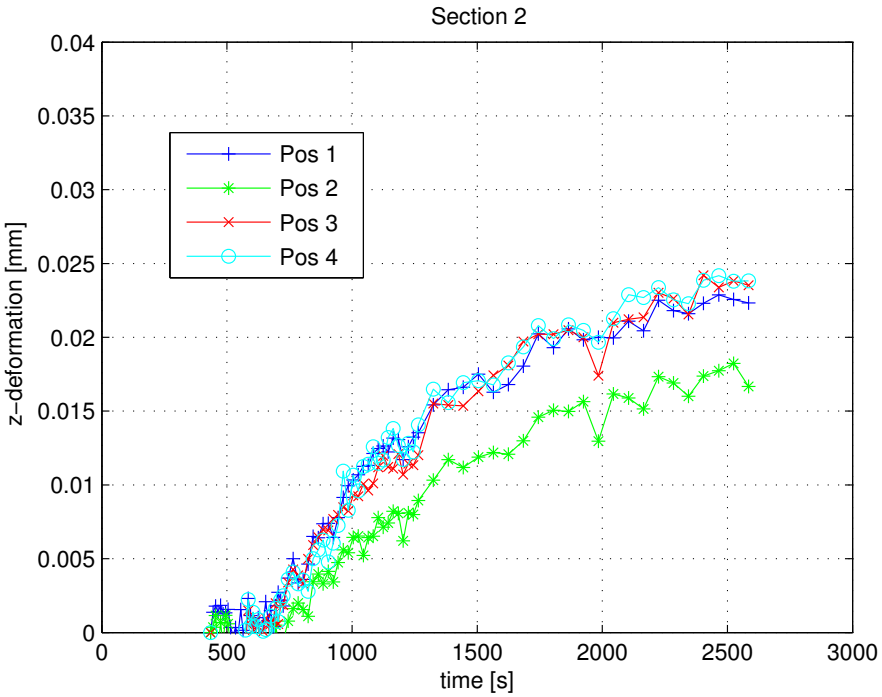

Figure. 3.6: Deflection over time - Section 2

A maximum local mold deflection of $0.066mm$ ($2 * 0.033mm$, for both mold halves) was measured. For the cavity thickness of $t = 4mm$, this leads to a maximum local deviation

of thickness compared to the intended value of $\Delta t = 1.65\%$. The lower the cavity thickness the bigger the resulting impact on the final V_f . The deflection rises with the impregnation progress and thus the flow front advancement. The maximum deflection happens when steady state flow is reached. The deflections are larger the closer the distance to the center line between the long sides of the mold. These results are logical because the further the flow front has progressed the more area of the mold is subject to the pressure load. Due to the clamping at the edges with zero deflection it is clear that the maximum deflection will be at the center line.

Another evaluation was performed specifically to obtain a measure for mold deflection due to fabric compaction. The difference between the *highest* and *lowest* z-coordinate within the area of the speckled pattern was found to be $\Delta z = 0.0084mm$ after tightening the bolts, assuming that the cavities were ideally flat at the start of the test. This difference in the z-coordinates is a result of the fabric compaction response. This force can be imagined as an additional fluid pressure applied homogeneously to the fabric through contacts between fibers and the mold. However, even for a very low cavity thickness of $t = 1mm$ it is less than 1% of the cavity thickness and therefore may be neglected.

As the measures of z-deformation do not give a concise description, e.g. the deflection-time-curve of position 2 gives the highest deformations for section 0 (Figure 3.6) and the lowest ones for section 2 (Figure 3.6), a smeared approach was employed to prediction test induced off-plane deformation. The deformations obtained with the deflection test were extrapolated to the entire mold using a polynomial curve fitting with the least-squares approach. One could employ formulae for bending lines derived for certain load cases, see Dubbel [111](p.C18ff). Here, polynomial regression was employed with orders of up to five where a bigger set of boundary conditions is required and this may lead to non realistic results at the edges. Thus, the most simple approach of polynomial fitting with second order shape functions was employed here resulting in a point-symmetric deformation with respect to the cavity center. The results are plotted in Figure 3.7.

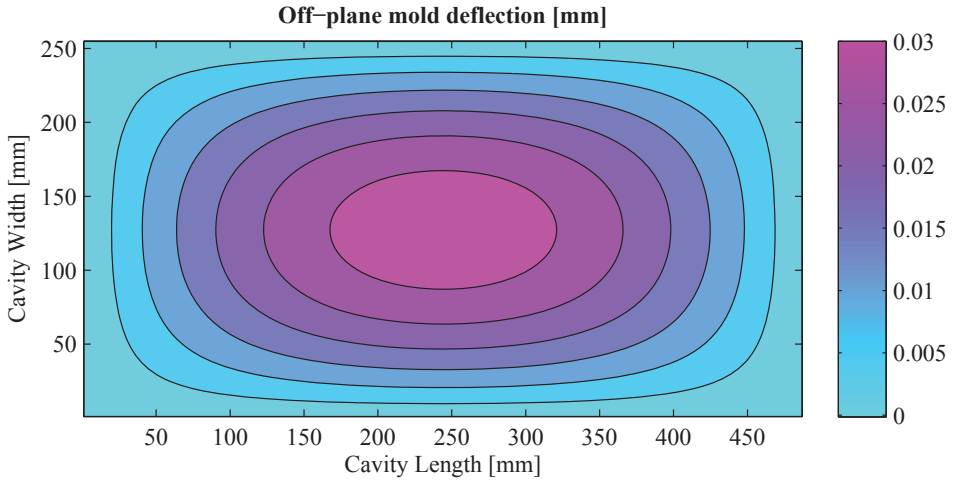

Figure. 3.7: Contour plot with extrapolated deflections for entire cavity

Integrating along the cavity dimension leads to an averaged mold deflection of $d_{avg} = 0.0148mm$ for one mold half. Assuming that the deflection is linearly dependent to the applied injection pressure one could define a factor m for two mold halves

$$m = \frac{2 \cdot d_{avg}}{p_{inj}} = \frac{2 \cdot 0.0148\ mm}{3\ bar} = 9.8710^{-3}\ \frac{mm}{bar}. \tag{3.1}$$

Then, one can derive the following relation for the deflection-induced change of V_f denoted as ΔV_f:

$$\Delta V_f = -V_{f,des} \cdot \frac{1}{1 + \frac{t_{des}}{p_{inj} \cdot m}}, \tag{3.2}$$

where t_{des} and $V_{f,des}$ are the desired quantities for the experiment.

Normalization of the deflection to the minimum tested cavity thickness of $1mm$ for the maximum tested pressure of $2bar$ (cf. Section 3.2) and an assumed $V_f = 55\%$ would lead to a V_f decrease of 1.06%.

This value shows that the impact of mold deflection is low, typically the changes of areal weight are in a similar range as can be seen in the result tables in the Appendix. However, mold deflection cannot be completely neglected depending on the test conditions. It is recommended to take mold deflection into account for higher V_f (resulting in higher forces introduced by the fabrics compaction) and lower thickness (cf. Equation 3.2).

Section 3.3.7, where transient and stationary test results are compared, will highlight the impact of mold deflection on permeability. For the presentation of all other permeability results in the following chapters, mold deflection has been neglected.

3.1.2 Sensor Technology

Darcy's law was derived for purely saturated flow in porous media. In practice, permeability is often measured during the impregnation phase, as has been suggested in the 2^{nd} permeability benchmark exercise [23]. The setup presented here is capable of measuring permeability during saturation, by sensing the flow front progression, called transient testing. This setup also enables measuring after saturation, called steady-state testing, by recording the mass flow rate at the outlet. Both tests can be conducted in progression without replacing the fiber preform enabling the comparison of the two permeability values as focused on in Section 3.3.7.

For permeability testing certain quantities have to be measured during the experiment. The injection pressure has to be continuously known. Depending on the test type - steady-state or transient, the detection of the flow rate or flow front progression are required respectively. The setup utilizes a *HBM P3MBP* reference pressure sensor installed at the central injection gate (cf. Figure 3.2) to continually monitor the injection pressure. The flow rate during steady-state testing is recorded using *HBM S2M* force transducers installed at each of the outlet gates where the test fluid is collected in buckets.

The main task for transient testing is proper detection of flow front progression. Most commonly, flow front is detected visually through a transparent top mold as it was suggested for the 2^{nd} permeability benchmark exercise [23]. This, however, comes along with a loss of mold stiffness that will results in bigger deflections. For the experiments in Section 3.3, a novel approach for flow front detection was employed. Experiments conducted by J. Holzapfel showed that pressure sensors are able to detect arrival of a flow front. Figure 3.8 shows an idealized (left) and a measured pressure curve (right) plotted over time recorded with pressure sensors in the mold along the flow direction.

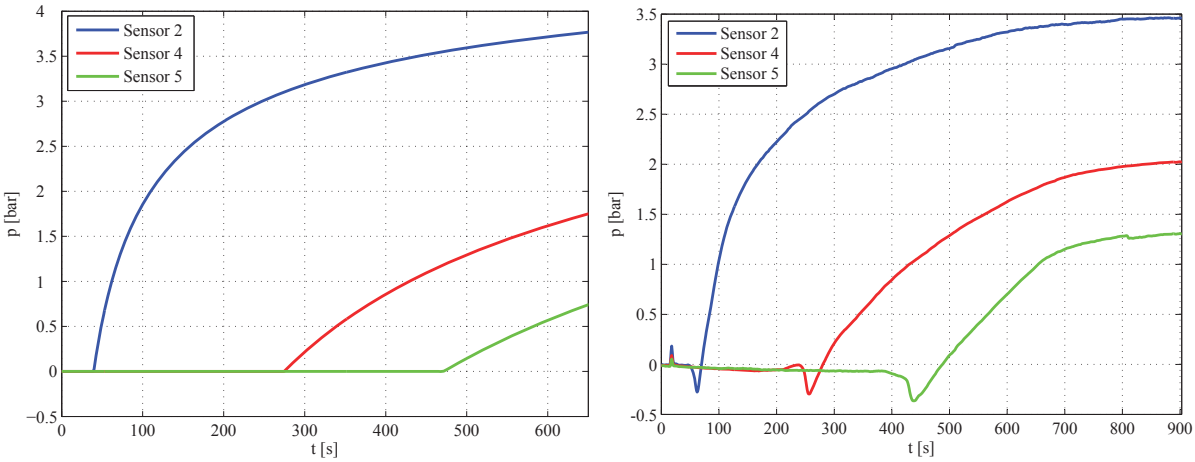

Figure. 3.8: Plot: Ideal and real p(t)-curves at certain position with $p_{inj} = const.$

Idealized pressure curves over time for defined position in the mold along the flow direction can be calculated using the following formula derived from Darcy's law;

$$p(x,t) = p_{inj} - x \cdot \sqrt{\frac{p_{inj}\ \mu\ (1 - V_f)}{2Kt}}. \tag{3.3}$$

The main difference between the two curves in Figure 3.8 is the pressure drop that is recorded with the sensors resulting from the difference between dry and wet compaction. Dry fibers show a certain force response to compaction and this force is significantly lower for impregnated (wet) fibers due to the lubricating effect of the fluid (resin). Based on this observation, an algorithm was developed to detect this pressure drop by differentiating the p-t-signal and then searching for the local minimum which represents the decline in the p-t-signal.

In the following the algorithm is presented in short format:

```
Assemby of p = f(t) data
Filtering signals
Derivation f‘(t) using diff
Detection of minimum in f‘(t) using min
Find points with slope of f‘(t) smaller than x % of the minimum
```

It has been demonstrated experimentally by using a transparent mold and pressure sensors for flow front detection that the method is very robust and three sensors along the flow direction are enough to evaluate permeability with sufficient quality. The validation experiments for the novel approach were completed by A. Schug within a semester thesis project [112]. In the setup, sensors produced by *Omega Newport* of type *PXM600* were installed which can be flash mounted so that they are smooth with the cavity boundary.

Permeability testing using the 1D approach is prone to race-tracking [61], which means an advancing of the flow front at the edges of the cavity due to imperfect sealing. Therefore, the test setup is equipped with sensors detecting race-tracking. Here, the same concept as for flow front detection using pressure sensors was employed. Sensors are positioned at the edges of the cavity to detect the flow there and compare it with the flow front position in the center of the cavity. Using this approach, experiments that show a high deviation between flow front position in the center compared to the edges can be rejected for evaluation. Additionally, silicon sealings are employed at the edges to ensure proper sealing. Silicon tapes with an oversized thickness (10-15%) are put between the edges of the cavity and the fiber preform, this approach has been suggested by Alms et al. [23]. Closing the mold compacts the silicon tapes and expands them in-plane due to Poisson ratio, possible gaps are closed and race-tracking is avoided. Figure 3.3 also depicts all pressure sensors. Pressure sensors for flow front detection are denoted as P and the pressure sensors for detection of race tracking as RT

3.1.3 Data Evaluation

Connection to the sensors and data acquisition is performed using a *National Instruments Compact DAQ* used in conjunction with *LabView 2012* software. Subsequently the gathered data is transferred to Excel using macros and the results for individual tests per cavity are saved in *xlsx*-format. This is a common format and has been chosen for that reason to be able to archive the data.

An in-house programmed Matlab tool with a graphical user interfaces (GUI) contains the algorithms for evaluation of transient and steady state permeability. Figure 3.9 depicts a screenshot of the evaluation tool's Main GUI. Coding and GUI creation has been performed by A. Schug [112].

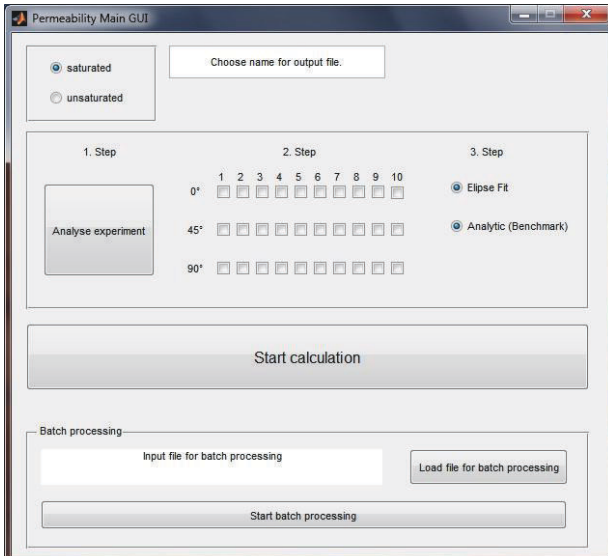

Figure. 3.9: GUI of permeability evaluation tool

The steps performed by the Matlab tool can be summarized as follows:

1. Import of experimental raw data
2. Evaluation of permeability (steady-state, transient or both)
3. Determination of principal permeability tensor using an
   - Analytical scheme provided by Weitzenboeck [21]
   - Algorithm based on least-square ellipse curve fitting (presented in detail in Section 3.3.5)
4. Export the results to a report in Excel format in a printable layout

3.2 Test Results Benchmark Exercise

Following section will focus on the experiments conducted for the benchmark exercise with a Hexcel woven fabric, see Table 3.1.

	Hexcel G0986
Areal weight $[g/m^2]$	285
Construction	Twill 2-by-2
Fiber type	Carbon HTA 5131
Yarn size	6K

Table. 3.1: Data sheet of testes woven fabric

The indices *SFF* and *LSF* in the results are abbreviations for squared flow front and least square fit that are averaging approaches presented in [23] to determine a permeability value based on flow front positions recorded at several times.

Squared Flow Front Approach
The squared flow front approach (SFF) calculates the permeability based on following equation:

$$K_{exp} = \frac{m}{2p_{inj}}\phi\mu, \tag{3.4}$$

where m is the slope of a fitted line when plotting the squared flow front position (x_f^2) over time t. p_{inj}, ϕ and μ are the injection pressure, the porosity and the viscosity.

Least Square Fit Approach
The least square fit approach (LSF) uses an integral form for the flow front position x_f.

$$x_f = \sqrt{\frac{2K}{\phi\mu}I(t)}, \tag{3.5}$$

where $I(t) = \int_0^t p_{inj}(t)\, dt$.

The integral is approximated with the trapezoidal rule of integration and finally a least square fit is applied to obtain the final equation to evaluate permeability:

$$K_{exp} = \frac{a^2\phi\mu}{2}, \tag{3.6}$$

where a is defined as

$$a = \frac{\sum_{i=1}^{n} x_{f,i}\sqrt{I(t)}}{\sum_{i=1}^{n} I(t)}. \tag{3.7}$$

Same as in the benchmark exercise article [51], LSF averaging method leads to smaller deviation in the results and will be used in the following for evaluation of permeability.

Tables 3.2, 3.3, 3.4 and 3.5 show the permeability results obtained for the 0°, 45°, 90° direction and the principal permeability. Figure 3.10 illustrates the definition of the test directions.

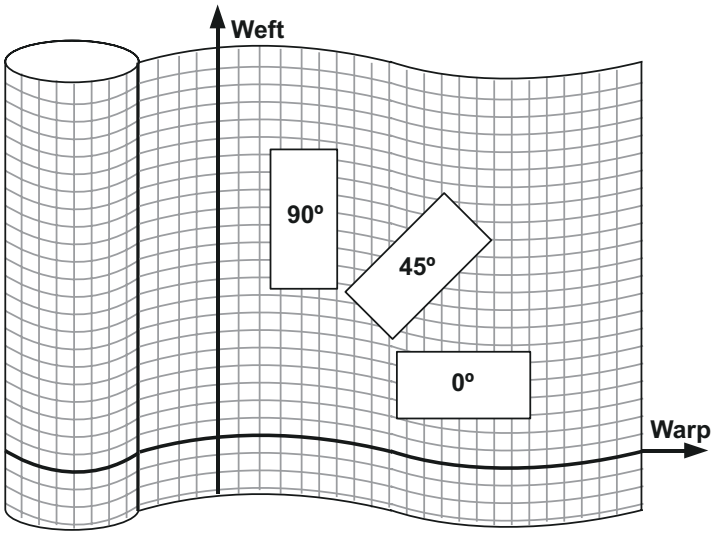

Figure. 3.10: Definition of permeability test directions from [23]

Test	$\mathbf{V_f}$ [%]	$\mathbf{K_{0,SFF}}$ $[10^{-11}m^2]$	$\mathbf{K_{0,LSF}}$ $[10^{-11}m^2]$
1	45.20	9.25	8.04
2	45.01	8.47	7.33
3	45.12	7.34	6.56
4	45.10	9.64	8.72
5	45.06	9.23	8.13
6	44.18	12.2	11.2
7	44.00	13.3	10.1
MEAN	48.21	9.91	8.58
STD	0.50	2.10	1.60
CoV [%]	1.11	21.13	18.67

Table. 3.2: K_0 permeability results

Test	$\mathbf{V_f}$ [%]	$\mathbf{K_{45,SFF}}$ $[10^{-11}m^2]$	$\mathbf{K_{45,LSF}}$ $[10^{-11}m^2]$
1	45.21	9.85	9.07
2	45.28	9.65	9.48
3	45.30	8.66	8.43
4	45.12	9.94	8.99
5	45.36	8.04	7.72
6	45.30	9.90	9.40
MEAN	45.26	9.34	8.85
STD	0.08	8.01	6.7
CoV [%]	0.19	8.57	7.57

Table. 3.3: K_{45} permeability results

Test	$\mathbf{V_f}$ [%]	$\mathbf{K_{90,SFF}}$ $[10^{-11}m^2]$	$\mathbf{K_{90,LSF}}$ $[10^{-11}m^2]$
1	45.12	16.7	15.0
2	45.21	13.5	12.5
3	45.06	15.1	13.5
4	45.30	12.4	11.3
5	45.21	15.3	13.0
6	43.87	14.2	13.2
7	44.35	15.3	13.3
MEAN	44.87	14.6	13.1
STD	0.55	14.1	11.2
CoV [%]	1.22	9.63	8.56

Table. 3.4: K_{90} permeability results

	$\mathbf{K_1}$ $[10^{-11}m^2]$	$\mathbf{K_2}$ $[10^{-11}m^2]$	$\boldsymbol{\beta}^1$ [°]
SFF	17.5	8.9	117.4
LSF	13.0	8.2	109.3

Table. 3.5: K_1, K_2 and rotation angle β

The experiments for the benchmark exercise have been conducted using a mold as it was introduced in the previous section, but with a transparent upper mold because the method for flow front detection hasn't been available at that time. A negative effect on the results is very unlikely because the comparison of optical flow front detection and to that using pressure sensors has shown nice correlation in experiments.

Permeability in 0° and 45° direction shows similar values of 8.58 10^{-10} and 8.85 10^{-10} whereas the value in 90° direction is significantly higher with a permeability of 13.1 10^{-10}. Main reason for this can be found in the difference of yarn tension between warp and weft direction and the resulting difference is flow channel architecture. Rieber [32] has investigated that phenomenon experimentally for different woven fabrics.

The results presented have a coefficient of variation (CoV) below 10% apart from the tests in 0° direction. The results are very close to the mean value evaluated for all test results submitted by the participants, as presented in [51]. In summary, the results prove the credibility of test setup and test method at LCC.

[1] β is defined as the angle between $K_{0°}$ and K_1

3.3 NCF Permeability Testing

Following section addresses the test campaign performed on two NCFs assessing the influence of areal weight, number of layers and V_f on permeability. Support during experiments has been provided by S. Faber in the framework of a semester thesis [113].

3.3.1 Materials

Two fabrics manufactured by Saertex were used Table 3.6 gives an overview of the material data of both fabrics. For the sake of simplicity the fabrics are referred to as *SAE 274* and *SAE 540* based on their areal weight and the manufacturer Saertex. These materials were chosen to enable a consistent study on the influence of areal weight as all other parameters such as manufacturer, fabric construction and stitching were the same. Figure 3.11 shows scans of the front and rear sides of both fabrics.

	SAE 274	**SAE 540**
Areal weight $[g/m^2]$	$274 \pm 5\%$	$540 \pm 5\%$
Construction	Biax $-45°$ / $+45°$	
Fiber type	Tenax HTS	
Yarn size	12K	
Stitch type	franse	
Stitch yarn	PES 48dtex	PES 76dtex
Stitch line distance $[mm]$	5.08	
Stitch length $[mm]$	3.18	

Table. 3.6: Data sheet of employed NCFs

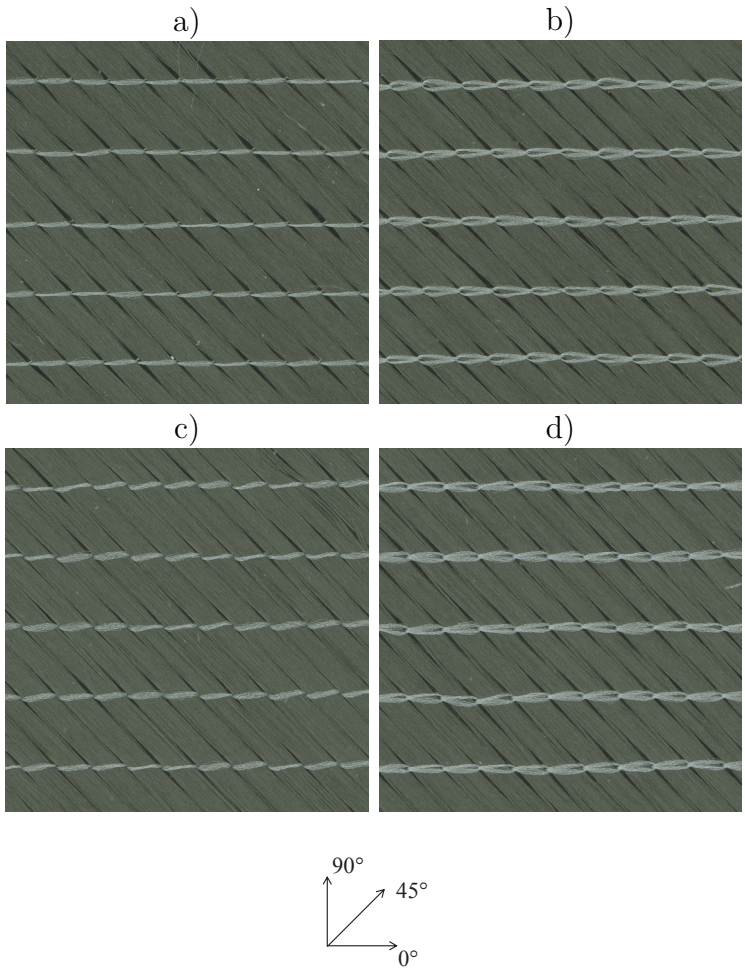

Figure. 3.11: Scans of SAE 274 front side (a) and rear side (b) and SAE 540 front side (c) and rear side (d)

3.3.2 Result Overview

This section gives a results overview about permeability tests conducted on the NCFs presented in Section 3.3.1. In contrast to the initial goal to determine permeability of preforms with thickness ranging from 0.25 mm to 5.0 mm and a range of V_f between 50% and 60%, experiments have been conducted for preform thickness between 1.0 mm to 5.0 mm and V_f between 50% and 55%. The tests for lay-up thickness below 1.0 mm and V_f above 55% could not be conducted due to problems associated with mold sealing.

Five repeats were conducted for each setting. Figures 3.12 and 3.13 show the mean and standard deviation values of the experiments, which can also be accessed in Appendix A.2. The coefficient of variation is below 10% for most of the tests. This shows the reproducibility of the employed test method.

Results show a clear trend for higher permeability when stationary testing is conducted. Stationary test results are higher by a factor of 1.42 for the SAE 274 and 1.25 for the SAE 540. Most likely, this was due to the higher deflections that occur for stationary testing.

During stationary testing, an injection pressure between 1 *bar* and 3 *bar* was applied to the entire mold whereas the transient testing employed a lower injection pressure (between 0.5 *bar* and 1 *bar*). The area of the mold exposed to the injection pressure is increasing during the experiment because of the progressing flow front. A detailed investigation of this phenomenon is presented in Section 3.3.7.

The influence of preform thickness, or number of layers respectively, on permeability appears to be rather low for the investigated thickness range. NCFs don't have out-of-plane undulations such as woven fabrics, so nesting between layers will not be as important as for woven fabrics. So one can assume that layers are geometrically well separated. In conclusion, the rule of mixtures may be employed without any correction factors accounting for the cavity thickness.

For the application of the simulation approach in Chapter 5 stationary permeability values were taken as reference. One major reason is that Darcy's law is derived for the state of a completely saturated porous medium. However, transient tests are often preferred because usually results can be obtained faster and it was also suggested for the benchmark exercise [51]. This work will reveal that permeability results from transient and stationary testing are similar but never exactly the same. Furthermore factors such as test cavity size have an impact. For a mold with infinite flow length transient and stationary permeability results would converge to the same value.

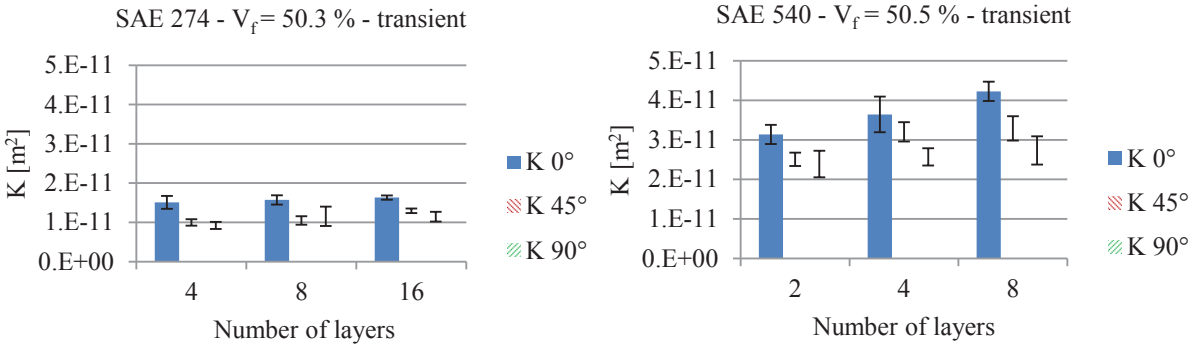

Figure. 3.12: Overview of results from transient permeability testing

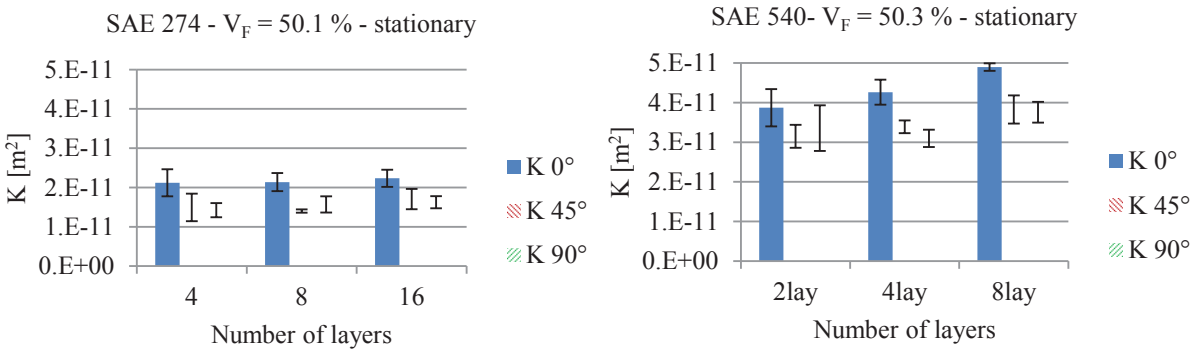

Figure. 3.13: Overview of results from stationary permeability testing

As expected, permeability for higher V_f is significantly lower as shown in Figure 3.14.

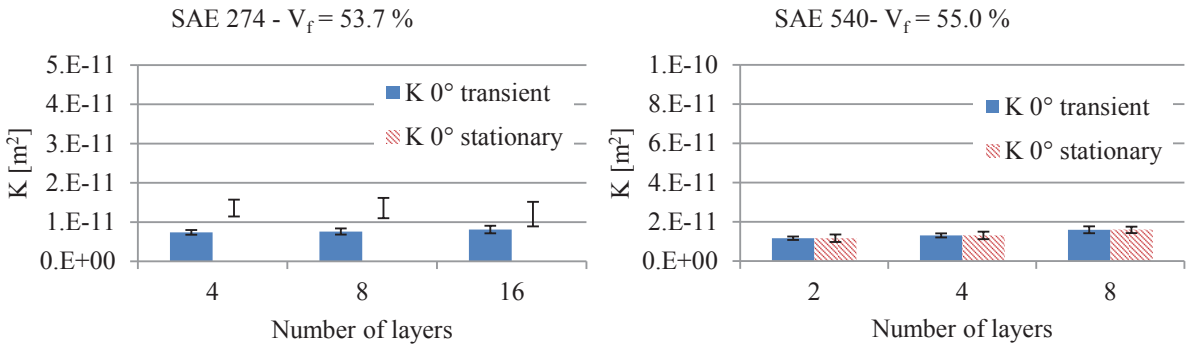

Figure. 3.14: Overview of results for $V_f > 50\%$

3.3.3 Influence of Areal Weight

As was already illustrated in the results overview, both fabrics show a strong difference in permeability when V_f and lay-up thickness are kept constant. In this section, these results are presented in greater detail. Figure 3.15 depicts K_{0° normalized to a $V_f = 50\%$ for lay-up thicknesses of $1.2mm$, $2.4mm$, and $4.8mm$ for both transient and stationary test methods. Normalization of the test results to $V_f = 50\%$ shows a difference between SAE 540 and SAE 274 by a factor ranging from 1.91 to 2.33 for steady state testing and 2.22 to 2.76 for transient testing.

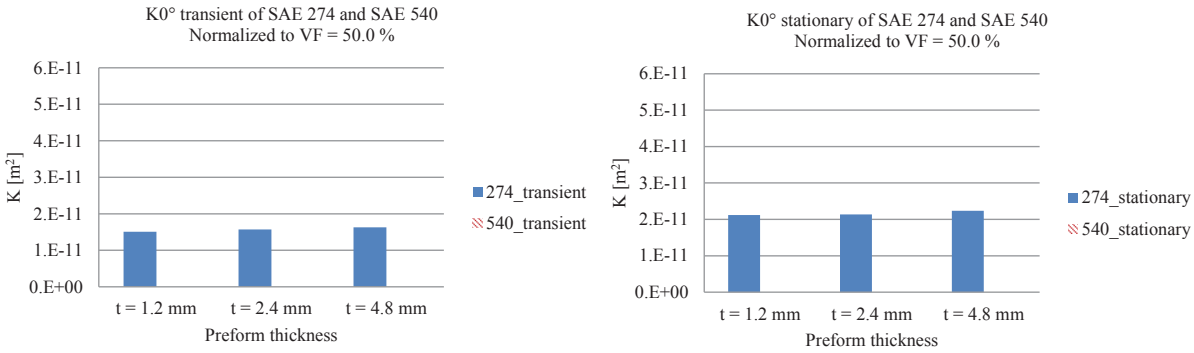

Figure. 3.15: Comparison of permeability results for fabrics with different areal weight

At a first glance, this effect might be surprising because what previous publications indicate is the strong impact of V_f on permeability and not the impact of areal weight when investigating fabrics of equal construction. A reasonable explanation can be provided by a relation known as the Hagen-Poiseuille equation that puts the diameter of a cylindrical pipe and the resulting pressure loss for a certain flow rate in a relation. The Hagen-Poiseuille equation [111](p.B48) states the following:

$$\Delta p = \frac{128 \mu L Q}{\pi d^4}, \tag{3.8}$$

where Δp is the pressure loss, L the length and d the diameter of a cylindrical pipe.

Figure 3.16 illustrates the gap distribution for a lay-up of SAE 274 and SAE 540 assuming equal V_f and stack thickness. To obtain an equal stack thickness, twice as many layers are needed for fabrics with half the areal weight to achieve the same V_f. Assuming equal V_f for both stacks leads to an equal area of the gaps for a certain cross-section, neglecting difference in intra-yarn porosity.

In the Hagen-Poiseuille equation the pressure is proportional to the inverse of d^4. Clearly, a higher number of pipes with a smaller diameter will lead to a significantly higher pressure loss (lower permeability) as a lower number of pipes with bigger diameter when total cross section of all pipes is equal. This explains why the stack of SAE 274 exhibits a lower permeability compared to the stack of SAE 540.

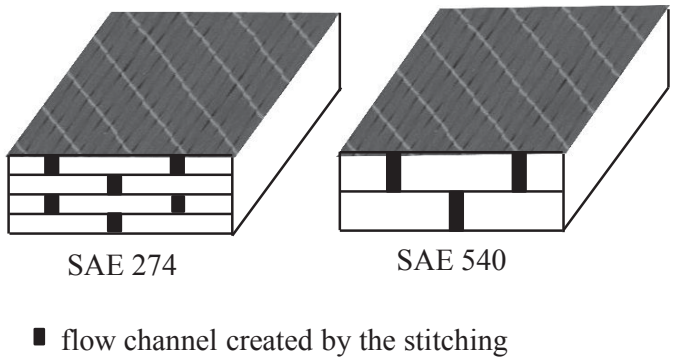

Figure. 3.16: Visualization of gap distribution for lay-ups of SAE 274 and SAE 540 assuming equal V_f and stack thickness

Due to a lack of information about actual capillary dimensions and intra-yarn porosity, the explanation may serve as an initial guess. The correct quantities to compare are the permeability of the pipe normalized by the cross-sectional area. This dimensionless quantity is called Darcy number (Da) [114]. The stitch used for SAE 540 has a bigger linear density (76dtex instead of 48dtex), i.e. larger in-plane gaps are created. Moreover, a heavier ply means a thicker ply, so the off-plane dimension of the gaps is higher as well. To conclude, Da should be considered for permeability evaluation because the hydraulic conductivity depends on the dimension and shape of the pipe. This level of information here does not allow to set up a general law for prediction of permeability as function of areal weight. On the other hand, it is a valuable hint for manufacturers who have to decide about the construction of a lay-up with respect to areal weight and number of layers. Without any doubts, this effect should be investigated further.

3.3.4 Influence of Layer Number

Figure 3.17 depicts principal permeability values K_1 and K_2 for both fabrics and both test methods, stationary and transient, for $V_f(SAE274) = 50.1\%$ and $V_f(SAE540) = 50.5\%$.

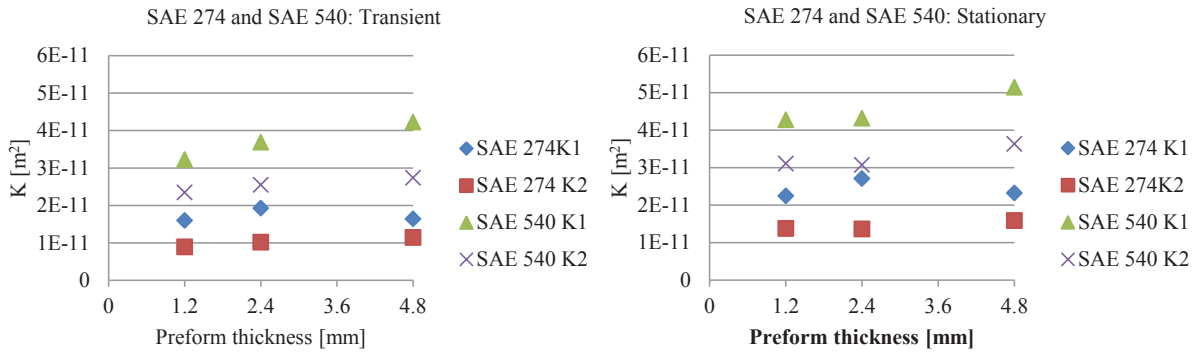

Figure. 3.17: Comparison of permeability results for different lay-up thickness

The influence of lay-up thickness / number of layers is not as significant as the influence of areal weight. Independently from the test method, there is a slight trend for higher permeability values the higher the lay-up thickness is for the SAE 540. For the SAE 274 this trend was not observed. Results indicate that a maximum permeability was observed for a lay-up thickness of 2.4 mm.

3.3.5 Comparison of Methods to Obtain Principal Permeability

In this thesis a new approach to determine principal permeability tensor components K_1 and K_2 and the rotation angle θ is proposed. This section will introduce an approach for coordinate transformation based on least-square curve fitting. The results were also compared to the results obtained with analytical schemes available, such as those from Gebart [20] and Weitzenboeck [21].

Analytical schemes require a mean value from a number of individual tests in each direction. Variability within this set of experiments is completely neglected for evaluation of principal permeability. In the proposed method, the principal permeabilities are evaluated from the individual tests (e.g. five experiments in the directions 0°, 45° and 90° as was done in the previous section) without prior averaging.

A literature review on ellipse fitting revealed that two techniques are commonly used: clustering and least-squares fitting. Clustering was used by Leavers [115], Yuen [116] and Rosin [117]. All of these solutions have one trait in common, their complexity for solving numerically. Least-square techniques, as proposed by Taubin [118] and Fitzgibbon [119] are easy to implement and will be followed in this section. In some cases, ready-to-use scripts are available on the open file exchange platform MatlabCentral[2]. The core task of least-square fitting is to find a set of parameters minimizing the distance between data points and the ellipse itself is minimized. Note that both least-square techniques presented here suffer from the fact that they will return hyperbola instead of an ellipse for the case that the data points a better fitted.

[2] `http://www.mathworks.de/matlabcentral/`

In the following a parameter study is presented comparing these algorithms. Presented tables are a joint work with Y. Shen who conducted a master thesis under my supervision [120].

The parameter study is conducted as follows:

1. Definition of an ellipse
2. Calculation of 20 data points that lie on the ellipse
3. Creation of 10 normally distributed artificial data points for each data point with a coefficient of variation (CoV) between 0.1 and 0.3.
4. Application of ellipse fit algorithms
5. Comparison of obtained ellipse equation to the initial one.

The algorithms employed here are

- a self-written algorithm applying least-square fitting denoted as *General ellipse fit*,
- an approach based on the *Direct ellipse fit* by [119] and
- an algorithm denoted as *Ellipse fit by Taubin* by [118].

Initially, an ellipse equation is chosen that could be from a real permeability experiment, see Table 3.7. As shown in Table 3.8, the interpolated geometry parameters are in good agreement for a coefficient of variation (CoV) below 10%. Naturally, errors increase with increasing CoV. Higher CoVs grow the interpolated semi axes except for the semi-major axis computed by the direct ellipse fit algorithm. Direct ellipse fit shows the best overall performance. The maximum errors for the prediction of semi-major and minor axis are 2.56% and 13.67%. For the general ellipse fit method the maximum errors of semi-major and minor axis go to 14.11% and 25.17% respectively. The errors of semi-major and minor axis with Ellipse fit by Taubin are 12.44% and 4.67%. In general, the quality of all these algorithms is not very different.

In a second step, an ellipse with an aspect ratio of 10 is fitted, as shown in Table 3.9. This phenomenon can happen while shearing fabrics that commonly leads to a stretch of the flow ellipse.

Semi-major axis	9
Semi-minor axis	6
Orientation [°]	5

Table. 3.7: Standard ellipse

CoV	Algorithm	Semi-major axis	Semi-minor axis	Orientation [°]
0.1	General ellipse fit	9.42	5.98	44.33
	Direct ellipse fit	9.23	5.89	44.50
	Ellipse fit by Taubin	9.46	5.77	44.83
0.2	General ellipse fit	9.52	6.70	38.21
	Direct ellipse fit	8.82	6.31	46.10
	Ellipse fit by Taubin	9.42	6.00	49.23
0.3	General ellipse fit	10.27	7.51	39.68
	Direct ellipse fit	8.80	6.82	44.75
	Ellipse fit by Taubin	10.12	6.28	48.80

Table. 3.8: Interpolation of the ellipse in Table 3.7 for different algorithms and coefficients of variation (CoV)

Semi-major axis	60
Semi-minor axis	6
Orientation [°]	45

Table. 3.9: Ellipse with high aspect ratio

CoV	Algorithm	Semi-major axis	Semi-minor axis	Orientation [°]
0.1	General ellipse fit	65.73	6.34	44.74
	Direct ellipse fit	55.33	6.29	45.27
	Ellipse fit by Taubin	75.22	6.05	44.61
0.2	General ellipse fit	63.19	7.33	44.38
	Direct ellipse fit	50.86	6.83	44.79
	Ellipse fit by Taubin	103.69	5.90	44.54
0.3	General ellipse fit	75.11	7.20	44.61
	Direct ellipse fit	57.94	6.60	45.31
	Ellipse fit by Taubin	181.20	6.08	44.03

Table. 3.10: Interpolation of the ellipse in Table 3.9 for different algorithms and coefficients of variation

Table 3.10 shows the results fitting the ellipse equation presented in Table 3.9. The interpolation of semi-major axis of ellipse fit by Taubin's method gives unrealistic results with increasing CoV. The maximum errors of semi-major and minor axis reach 202.00% and 1.67% when CoV of 30% are used. The other two algorithms still show reliable quality as before. The maximum errors of semi- major and minor axis amount to 25.18% and 20.00% for general ellipse fit method meanwhile 3.43% and 10% for direct ellipse fit method.

From these results, it my be concluded that, direct ellipse fit method shows the best performance with a maximum error of about 10%. The general ellipse fit also shows good results by keeping the error around 25%. Ellipse fit by Taubin's method will not be further considered due to the poor interpolation quality of ellipse with high aspect ratios.

As stated in previous sections, for permeability testing three directions are measured, commonly 0°, 45° and 90°. For the interpolation, this means there are only three data points along with three mirrored points. The mirroring of the data points is based on the assumption that the permeability of a perform in one direction is equal to that when flow is happening in the reverse direction. This step is necessary, because otherwise the ellipse would not be centered around the coordinate system's origin. It would also be possible to restrict the ellipse equation itself to a point-symmetric ellipse with respect to the origin. Here however, the impact on quality and efficiency of the algorithms is not ensured anymore.

In the following, six data points from the orientations 0°, 45°, 90°, 180°, 225° and 270° are used for interpolating the ellipse parameters to represent a more realistic case.

Table 3.11 shows the fit results of the ellipse described in Table 3.7. As there are less data points, the quality of interpolation is lower compared to what was previously observed. The maximum errors of semi-major and minor axis is 48.89% and 8.17% for general ellipse fit method and 32.11%, 4.17% for direct ellipse fit.

CoV	**Algorithm**	**Semi-major axis**	**Semi-minor axis**	**Orientation** [°]
0.1	General ellipse fit	9.28	5.72	44.89
	Direct ellipse fit	9.10	5.59	45.17
0.2	General ellipse fit	9.23	6.13	42.32
	Direct ellipse fit	8.80	5.75	42.26
0.3	General ellipse fit	13.40	6.49	43.29
	Direct ellipse fit	11.89	5.90	46.19

Table. 3.11: Interpolation of the ellipse in Table 3.7 for different algorithms and coefficients of variation

The parameter study showed that changes in ellipse orientation do not affect interpolation quality. In the following, ellipses with different orientations angle are fitted, because the 45°-orientation is a special case and it shall be shown that choice of orientation does not affect fit quality.

Semi-major axis	9
Semi-minor axis	6
Orientation [°]	60

Table. 3.12: Standard ellipse with 60° orientation.

CoV	Algorithm	Semi-major axis	Semi-minor axis	Orientation [°]
0.1	General ellipse fit	8.97	5.80	53.95
	Direct ellipse fit	8.87	5.71	53.76
0.2	General ellipse fit	9.27	6.99	68.92
	Direct ellipse fit	8.95	6.58	65.92
0.3	General ellipse fit	12.22	7.05	53.47
	Direct ellipse fit	10.72	6.34	53.28

Table. 3.13: Interpolation of the ellipse in Table 3.14 for different algorithms and coefficients of variation

Results in Table 3.13 are fitted parameters from the ellipse shown in Table 3.12 and are quite similar to table Table 3.11 showing that the changed orientation has a negligible influence on ellipse fits. The maximum errors of semi-major and minor axis are 35.78% and 16.67% for general ellipse fit method, they add up to 19.11% and 5.67% for direct ellipse fit method.

Analogously to what was done in the previous section, an ellipse with high aspect ratio is also defined here, as shown in Table 3.14.

Semi-major axis	60
Semi-minor axis	6
Orientation [°]	60

Table. 3.14: Ellipse with high aspect ratio and 60° orientation.

Direct ellipse fit method is not a suitable method here (Table 3.15). The predicted semi-major axis has an error of 63.75%. In contrast, interpolation of the general ellipse fit method is very good with the biggest error of 19.95% for calculation of the semi-major axis.

CoV	Algorithm	Semi-major axis	Semi-minor axis	Orientation [°]
0.1	General ellipse fit	67.33	6.13	60.60
	Direct ellipse fit	28.80	6.51	58.18
0.2	General ellipse fit	60.73	6.21	59.81
	Direct ellipse fit	23.86	6.62	55.41
0.3	General ellipse fit	48.03	7.27	59.75
	Direct ellipse fit	21.75	7.17	54.12

Table. 3.15: Interpolation of the ellipse in Table 3.14 for different algorithms and coefficients of variation

In conclusion, the general ellipse fit method gives the best regression quality and shows the best overall quality for regression analysis. The error of predicted semi-major axis

lies between 20% and 25% while the error of semi-minor axis is kept at around 20%. The orientation of ellipse can be captured accurately. Thus, in the next sections, the general ellipse fit method is used for interpolation of principal permeability.

In the following section, general ellipse fit is employed to interpolate principal permeability tensor orientation for the experimental results previously presented in this chapter. Figures 3.18, 3.19 and 3.20 show the values obtained for K_1 and K_2 and the rotation angle θ for cavity thickness of $1.2mm$ (Fig. 3.18), $2.4mm$ (Fig. 3.19) and $4.8mm$ (Fig. 3.20).

Differences between curve fitting and analytical determination are small for all cases. This shows that the curve fitting technique employed is equally suited for the determination of principal permeability tensors.

For the $1.2mm$ case depicted in Figure 3.18, K_1 is overestimated by the curve fit. An explanation to that case is straightforward. A look to the results tables in the Appendix reveals that an individual permeability result had to be rejected from evaluation due to race-tracking. Then, the curve fit algorithm has to deal with imbalanced input date, five test results for two test directions and just four valid results for the third direction. This has an influence on the results of the fit. Here, the result from analytical determination seems to be more realistic. The reason is that averaging test results of each direction prior to evaluation blurs the impact of rejecting tests.

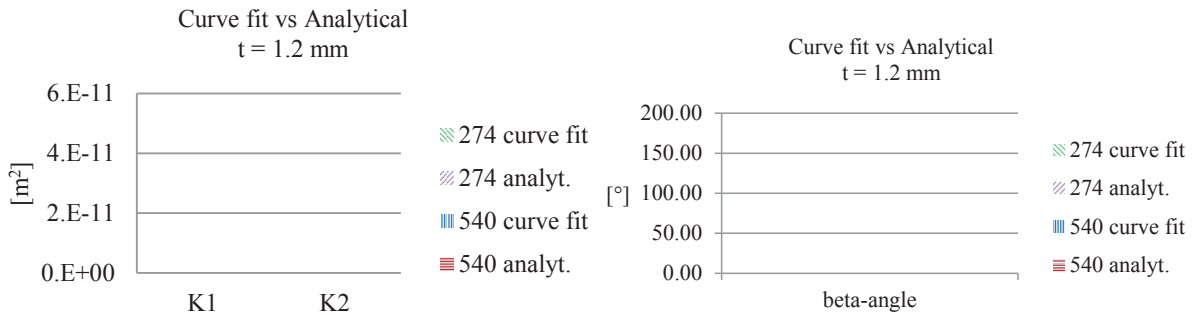

Figure. 3.18: Comparison of principal permeability obtained with ellipse fit and analytic schemes for $t = 1.2mm$

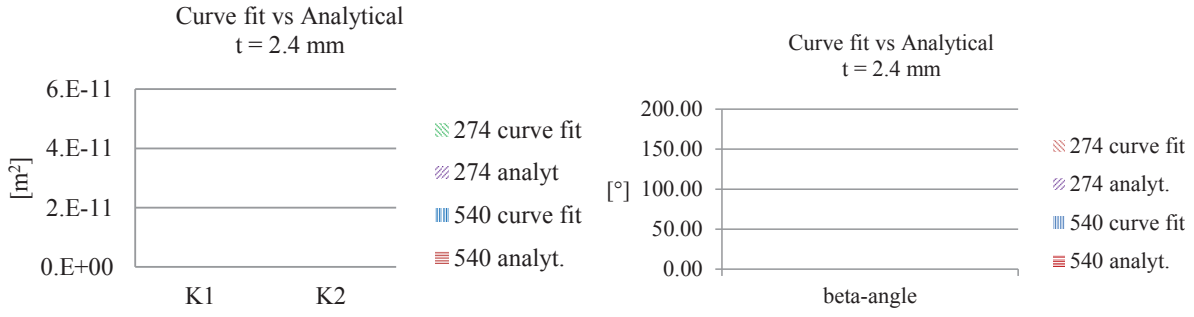

Figure. 3.19: Comparison of principal permeability obtained with ellipse fit and analytic schemes for $t = 2.4mm$

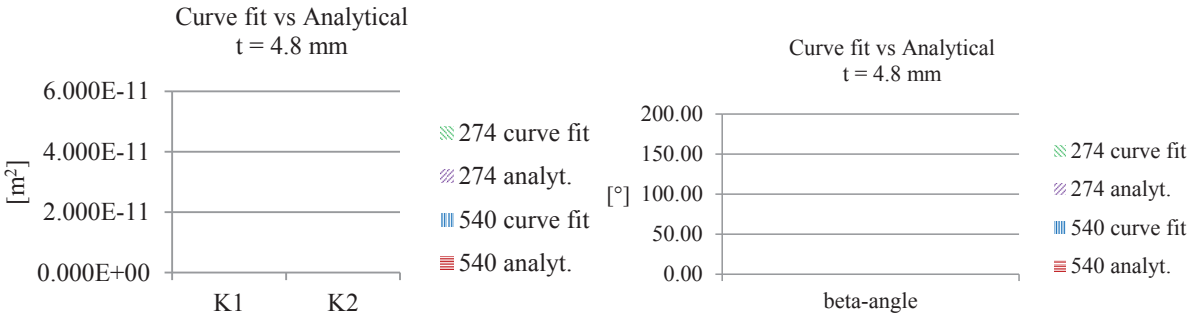

Figure. 3.20: Comparison of principal permeability obtained with ellipse fit and analytic schemes for $t = 4.8mm$

3.3.6 Permeability Tensor Rotation

Results for both fabrics show that the β (angle between $K_{0°}$ and K_1) is positive as can be seen in Table 3.16, i.e. that the permeability tensor is rotated towards the rear-side fibers. The rotation angle is very sensitive to the test conditions and varies between 10.20° and 31.15° with a coefficient of variation of 40.2%. The structure of the fabrics would suggest that K_1 or K_2 is oriented parallel or perpendicular to the stitching because the fabric is symmetric (equal amount of fibers in front- and rear-layer) and no other feature is present that could explain that asymmetry.

Configuration		**Rotation angle**
SAE 274, $V_f = 52.6\%$,	4 layers	17.70°
	8 layers	31.15°
	16 layers	16.60°
SAE 540, $V_f = 50.8\%$,	2 layers	31.61°
	4 layers	10.20°
	8 layers	20.06°
MEAN		21.22°
STD		8.52°
CoV		40.2%

Table. 3.16: Orientation of principal permeability tensor with respect to the test directions

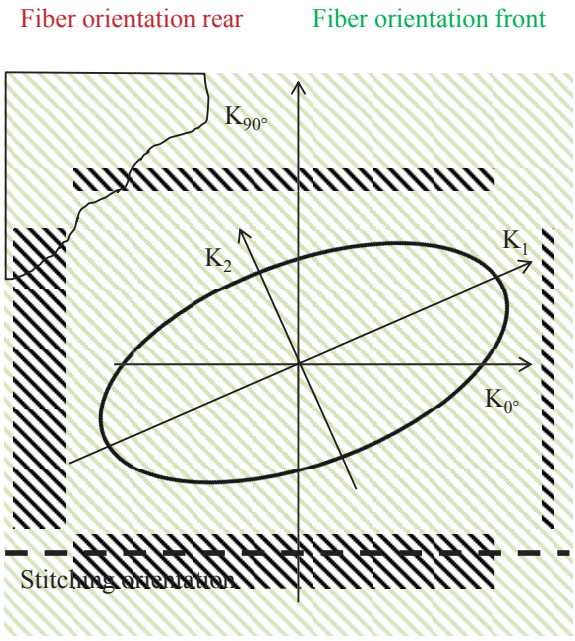

Figure. 3.21: Rotation angle of principal permeability tensor

Figure 3.21 illustrates the tensor rotation effect in relation to the fiber orientation of front and rear-side. A straightforward explanation for this result cannot be given by the fabric construction. However, a closer look at the fabric scans in Figure 3.11 reveals the reason for the asymmetry. The gaps introduced to the fabrics by the stitching seam to be bigger on the rear-side.

Digital processing of the scanned images using a standardized procedure confirms this observation. Front and rear-side images of both SAE 274 and SAE 540 have been processed using the following functions (part of the Matlab image processing toolbox):

- gray-level thresholding (extract 0-75 from 255 gray-levels),
- morphological filtering (imfill, bwareaopen)

and the resulting fraction of gap area compared to the area of the entire image has been evaluated. Details on image processing can be gleaned in Chapter 4.

Material		Gap fraction	Image size
SAE 274	Front	6.4%	3477 x 3981 px
	Rear	6.9%	3477 x 3981 px
SAE 540	Front	3.1%	3477 x 3981 px
	Rear	8.0%	3477 x 3981 px

Table. 3.17: Gap fraction evaluated from front and rear-side scans of SAE 274 and SAE 540

Table 3.17 shows that for the SAE 540 the fraction of gaps on the rear-side is significantly higher than on the front-side. These gaps act as preferred channels for the fluid to faster impregnate the fabric and they are the reason for enhanced permeability in this direction.

3.3.7 Influence of Test Method

The investigations performed in the previous section are all consistent in terms of the test method. I.e. all conclusions that are drawn are valid for both transient and stationary testing. However, stationary testing provides results that are higher with factor of 1.25 and 1.42 depending on the material as already mentioned on Section 3.3.2. In the following section this phenomenon will be investigated more in-depth.
Figure 3.22 depicts exemplarily transient and stationary permeability values of lay-ups of equal thickness (16 layers of SAE 274, and 8 layers of SAE 540) including a further stationary value evaluated at the same pressure as the transient experiment has been conducted.

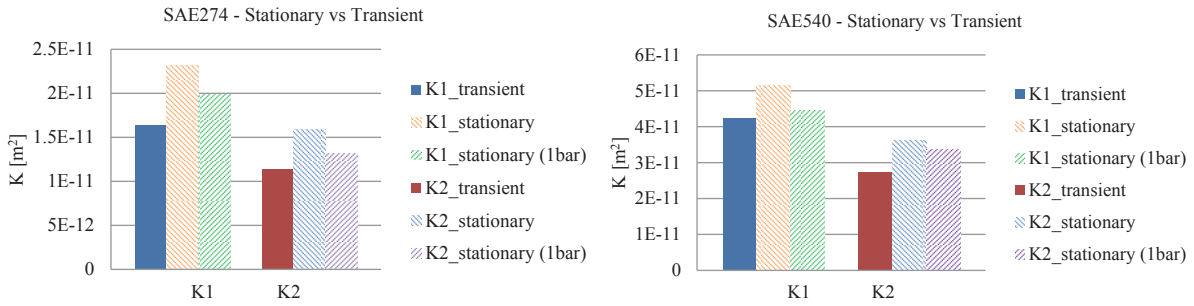

Figure. 3.22: Comparison test method

As Figure 3.22 indicates, the stationary permeability evaluated at the injection pressure of transient testing ($p_{inj} = 1.0bar$) is lower compared to the stationary permeability that are evaluated at injection pressures $p_{inj,1} = 1.0bar$, $p_{inj,2} = 2.0bar$ and $p_{inj,3} = 3.0bar$. As already stated, a stationary test is conducted after a transient test in the same mold with the same preform. Also, it has always been assessed whether the preform has moved during testing, in these cases both tests - stationary and transient - haven't been further progressed. Apart from strain in the fiber bed due to compaction, there is no movement of the fibers. With these information at hand, it is most likely that the difference of permeability between transient and stationary testing arises from mold deflection. That hypothesis also can explain, why the results from stationary evaluation with one pressure step are lower than these with regular evaluation. Furthermore, it can be explained why the transient results are lower than any stationary results.

During transient testing, the injection pressure is never acting on the entire mold, apart from the last moment of the experiment when the preform is completely impregnated. Because the injection pressure is kept constant during the experiment, the averaged deflection will be smaller for a transient test compared to a stationary tests with the same injection pressure.

Another origin for the difference between steady-state (stationary) and transient testing is the influence of capillary pressure. Capillary pressure will help the resin to flow for transient testing, i.e. the capillary pressure will act as additional driving force. Capillary pressure does not exist anymore when the air is removed and the preform is completely saturated. Since transient conditions are a mix between saturated (far behind the flow front) and transient flow (in the vicinity of the flow front), capillary effects are less influential when the flow extend increases. In conclusion, the additional driving force due to capillary pressure is overcompensated by the deflection of the mold that has occurred for all stationary experiments conducted here.

4 Simulation Approach of Permeability Prediction

This chapter focuses on the concept and design of an approach to determine fiber fabric permeability exclusively through the application of simulation methods. Section 4.1 introduces the simulation approach technique. The literature review in Chapter 2 is reviewed and detailed goals are presented here. Section 4.2 discusses the facilities developed and used to obtain high-definition digital images of fiber fabrics that will be processed to set-up fabric models. In Section 4.3, an image processing suite that has been developed is presented and the capabilities are demonstrated. Section 4.4 discusses recent developments that have been implemented to WiseTex. An outline of the work presented here has been already published in the *Journal of Composite Materials* togehter with Lomov et al. [121]. A number of conference proceedings [122, 123, 124] have focused on different aspects of the simulation approach. Finally an image processing suite called *FASTER*, representing 'Fiber Architecture and STructurE Recognition' has been developed. *FASTER* is a Matlab based software tool that allows users to perform the image processing by interacting with an easy to use GUI and store the extracted information in various formats so that they can be further processed for fabric modeling or fabric quality assurance. The effort of developing a software tool of that complexity cannot be done alone and was supported by several students under my supervision whose works are acknowledged here; J. Geisenhofer [125] has provided support in coding, C. Zeller [126] has improved usability and the documentation and E. Winterstein [127] added the batch-processing functionality.

4.1 Introduction

Frishfeld et al. [109] first introduced the concept of applying a simulation approach in order to determine fiber fabric permeability. There it was discussed that all relevant information for modeling can be stored in images taken from a fabric. Furthermore, they state that as long as the image acquisition is robust and repeatable, one can employ digital image processing to extract desired quantities for modeling. As intrinsic permeability has the unit $[m^2]$, it is a geometric characteristic of the porous medium. Thus, image processing in order to analyze the geometry seems natural. Here, an implementation of that idea is developed based on algorithms and mathematical tools such as Fourier transformation and new developments.

Theoretical background and available tools presented in Chapter 2 have been evaluated and the following sections outline the techniques used to incorporate preexisting tools with tools developed specifically for this work. Following research goals were defined taking into account previously published work:

- Development of a comprehensive tool for image processing to obtain all information relevant for fabric modeling
- Embedding the image processing into a tool chain capable of evaluating fabric permeability for RTM modeling from fabric images using textile modeling

Research institutes and companies have developed a number of tools for image processing with particular capabilities. For example, the sensor developed by Profactor [108] may be used efficiently to determine fiber orientation and as well as textile irregularities. Table 4.1 lists all quantities required for modeling in WiseTex[1], including those that are not known a priori or cannot be calculated. So far, no comprehensive tool is available to perform all the relevant image processing tasks. This manifests the need for development of a new tool.

Textile modeling tools, such as those developed by Lomov and Long [72, 73, 74] provide a good basis for fabric modeling. WiseTex has excellent capabilities to model NCFs and may be used in conjunction with FlowTex to determine permeability of fabric models. However, WiseTex format is open yet allowing model manipulation using text editors. Furthermore, the WiseTex engine can not be operated from outside using e.g. command line prompts.

Domain	**Symbol**	**Description**	**Unit**	**Source**
Fiber	V_f	Fiber volume fraction	[%]	known a priori
	t_i	Thickness of ply	[mm]	from V_f
	a_i	Orientation of ply	[°]	known a priori
	d_{fil}	Fiber diameter	$[\mu m]$	datasheet
	ρ_{fil}	Fiber density	$[g/cm^3]$	datasheet
	tex	Fiber linear density, tex	$[g/km]$	datasheet
Stitching		Pattern		datasheet
	L	Spacing length	[mm]	datasheet / fabric analysis
	W	Spacing width	[mm]	datasheet / fabric analysis
	d_{yarn}	Yarn diameter	[mm]	datasheet / fabric analysis
Gaps	a	Aspect ratio	[-]	fabric analysis
	k_f/k_b	Size ratio for gaps	[-]	fabric analysis

Table. 4.1: Input required for a WiseTex STM model

Based on the information from the previous section, a scheme has been developed with the focus of using available tools, developing what has to be developed and bringing it together in a clever way. Figure 4.1 provides a conceptual overview of the simulation approach. The overall framework implies tools to execute four main steps: image processing, fabric modeling, permeability determination and post-processing. Matlab has been

[1]WiseTex requires additional information for specifiying the stitch yarn that have no influence and are not mentioned here for the sake of compactness. Detailed information can be found in the WiseTex documentation [76].

chosen as coding language for certain reasons. Firstly, it is a very common and powerful programming language. A large library of ready-to-use functions is available in the fields of image processing, signal processing and curve fitting. Especially the image processing toolbox is a great benefit compared to other languages like Python or C++. Matlab provides wizards to compile routines to stand-alone executables. This allows to use tools on computers without Matlab installation. Finally, Matlab's ability to interact with tools running on Windows, e.g. execute command-line prompts allows straightforward embedding of external tools.

The main path in the framework is to input fabric images and to obtain a material card for a Darcy solver such as PAM-RTM or SimLCM. However, it must be clear that as a result of complexity the tool cannot be considered as black box requiring no user interaction. Thus, the image processing requires user interaction because the variety of fabrics is huge. As Table 4.1 has shown not every information for fabric modeling can be created in the tool. So, the tool requires a default material model containing all a priori known information. Also, the FlowTex solver requires adjustments depending on the fabric.

Furthermore, the results from image processing can be used for purposes such as quality inspection or assessment of variability of fiber fabrics, both providing an added value additional to the core task of permeability prediction.

Within the next sections, the modules of the framework are presented in detail.

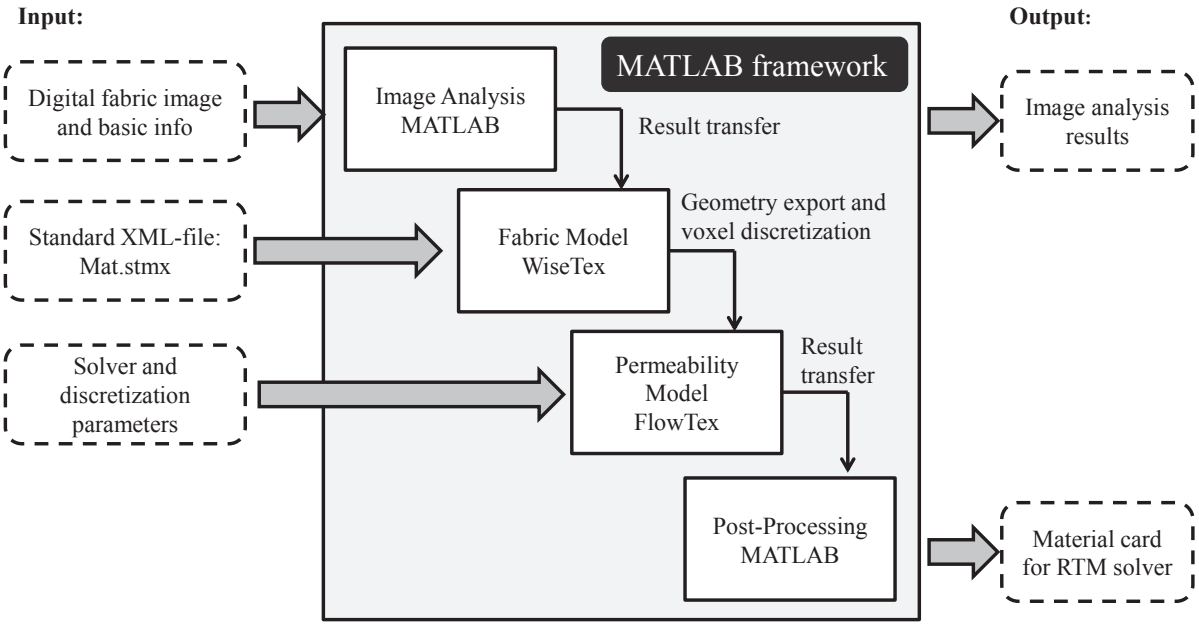

Figure. 4.1: Simulation approach for permeability prediction

4.2 Image Acquisition

In this section, a scanning technique together with the associated equipment is presented. Obtaining high-quality images is crucial as the entire prediction process relies on the information obtained from this. It is very important to scan the fabric in a state that resembles the environment of fabrics during RTM processing.

Therefore a compaction mold was designed fulfilling the following requirements:

- V_f can be adjusted with the cavity thickness of the mold
- The material of the compaction mold is transparent.
- The fabrics can be scanned from both sides
- For a front and rear scan, the mold should be closed only once to avoid altering the fabric structure
- The mold should be able to be rotated so that possible negative effects due to exposure to light, such as reflections may be avoided.
- The mold must not deform due to fabric compaction.

A rigid compaction mold has been developed that allows to scan single layers of carbon fiber fabrics in the *in-situ* state. Each mold half consists of a $10mm$ thick glass plate to avoid deformation due to fabric compaction. The clamping devices are flash mounted, so fabrics can be scanned from both the front and rear-side. In analogy to the mold for experimental permeability testing, cavity thickness, and hence V_f may be adjusted using distance shims. These shims are available in thickness increments of $0.05mm$ over a sufficient thickness range at tool retailers. Figure 4.2 depicts the compaction mold with distance shims for thickness adjustment, screws and nuts to keep it compacted and a fabric to be analyzed on top of a scanner.

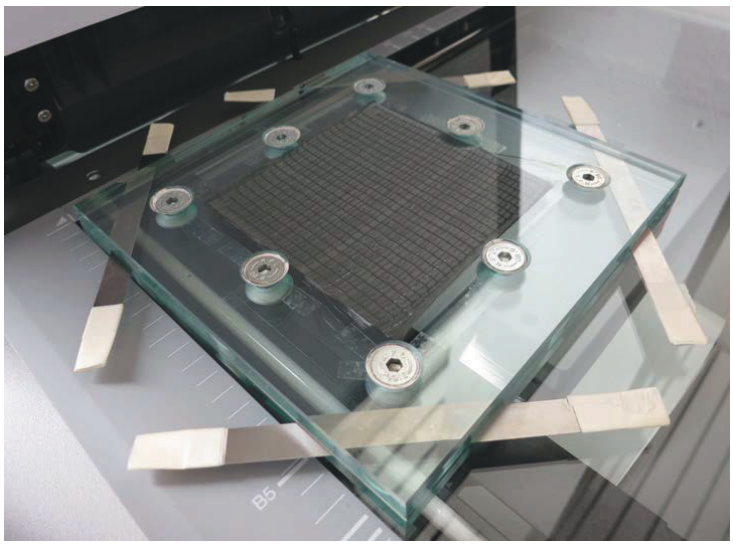

Figure. 4.2: Compaction mold for fabric scanning

To ensure high image quality and scanning repeatability using a flatbed scanner was favored over a camera system. Two scanners were used, a *Canoscan 9000F* and a *Epson 10000XL*. For creation of the high-grade images for processing only the *Epson 10000XL* was used because of its autofocus option which enables to compensate for the glass mold thickness, and its uniformity in illumination. The Epson scanner has a physical resolution of 4800 dots per inch (dpi) which results in a resolution of $5.3\mu m/px$.

Trials in scanning have shown that fiber orientation with respect to the scanner field has a huge impact on image quality. The best images were obtained when the fabrics was scanned with the fibers oriented perpendicular to the feed direction of the scanner head. A resolution of $1200dpi$ has proved to be the best trade-off between CPU time and quality for image processing. Images were stored in tagged image file format (*.tiff) because data is not compressed and meta data such as color space information can be stored.

4.3 Image Processing

This section presents the research conducted on the field of image processing. Section 4.3.1 gives an overview about the capabilities and the GUIs of FASTER. Section 4.3.2 gives a detailed explanation of the employed functions. Algorithms are summarized and the reader is referred to the source code of the FASTER tool for greater detail. Section 4.3.3 presents an image processing study performed on six fabrics and shows the capabilities and limitations of the FASTER tool.

4.3.1 Overview Image Processing

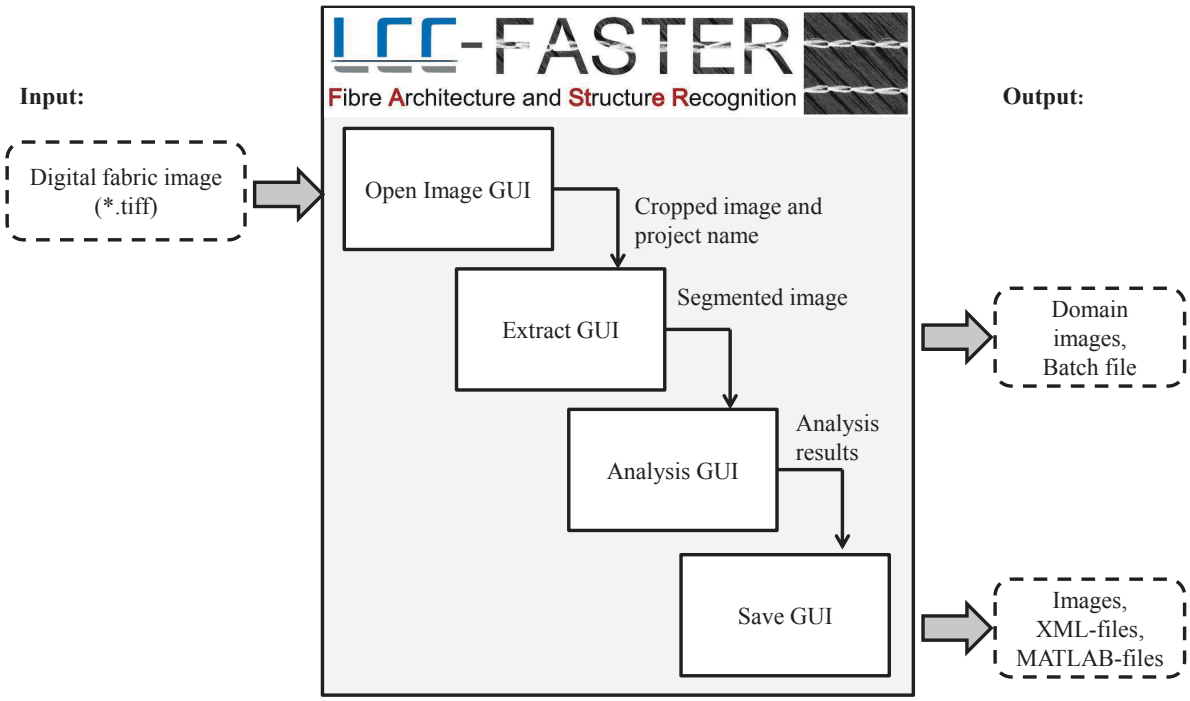

Figure. 4.3: FASTER overview

Figure 4.3 shows the structure of the FASTER image processing tool. The image processing procedure can be clustered into four main steps:

- Loading scanned images and performing preliminary checks
- Extracting image domains
- Analyzing the domains
- Exporting results to the desired format

In the following section, this procedure will be presented by exemplarily investigating a fabric with the FASTER toolbox. A detailed user manuals is provided with the documentation of FASTER.

Executing the main file in Matlab starts the OpenGUI (Figure 4.4). Here, the scanned image of the fabric can be opened for processing and is always depicted in the left area of the GUI within a grid showing the pixels. The field *Image Properties* depicts the EXIF information that is extracted from the image file. Additionally, the field *Examine Image* grants access to functions that can be used to perform preliminary checks on the image. Here, angles and dimensions can be measured directly in the images. While loading an image, it is converted to an 8-bit gray-level image (256 gray levels) to increase efficiency. All image processing algorithms can be used along with graylevel images, hence it was

not necessary to work with color images. This significantly reduces the amount of data that is manipulated. Furthermore, a gray-level histogram can be created, allowing the assessment of validity of gray-level thresholding.

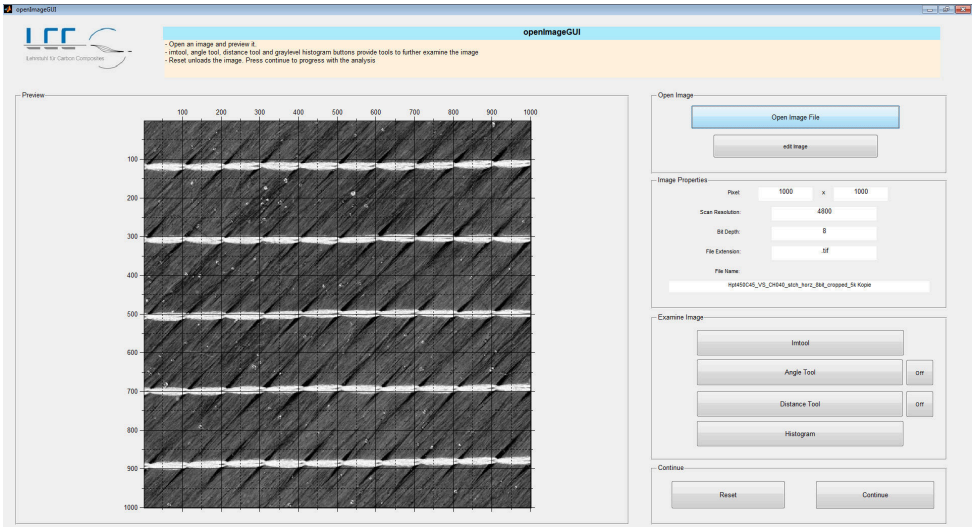

Figure. 4.4: FASTER start screen

The button *Edit Image* allows to manipulate the image. These functions, are presented in Figure 4.5. Images can be rotated with arbitrary angles. Rotation allows to align the images with respect to a pre-defined reference direction. Orientation of a horizontal line is defined as 0°. A cropping function is implemented for restricting the analysis to certain areas of interest. By finishing these two steps, one gets back to the OpenGUI and the analysis on the manipulated images may be pursued.

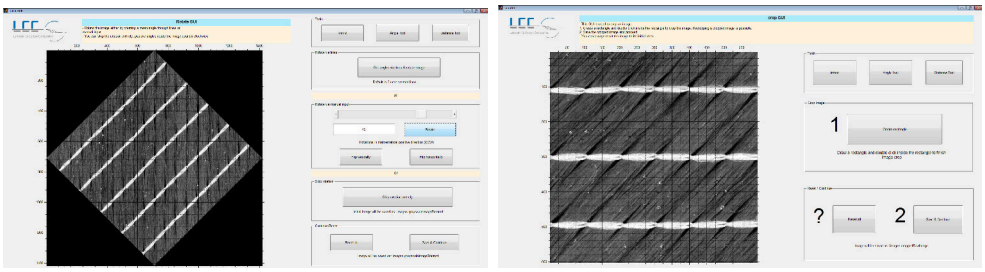

Figure. 4.5: FASTER GUI for image manipulation

The main function of the ExtractGUI (Figure 4.6) is to segment the image into its domains, i.e. to separate and group pixels that represent a domain such as fibers, stitching or gaps. Arbitrary names for the domains can be given. The number of segmented domains is not limited, hence saving several states of an individual domain with iterations of parameters is possible. The segmentation results can be reviewed or deleted at any time.

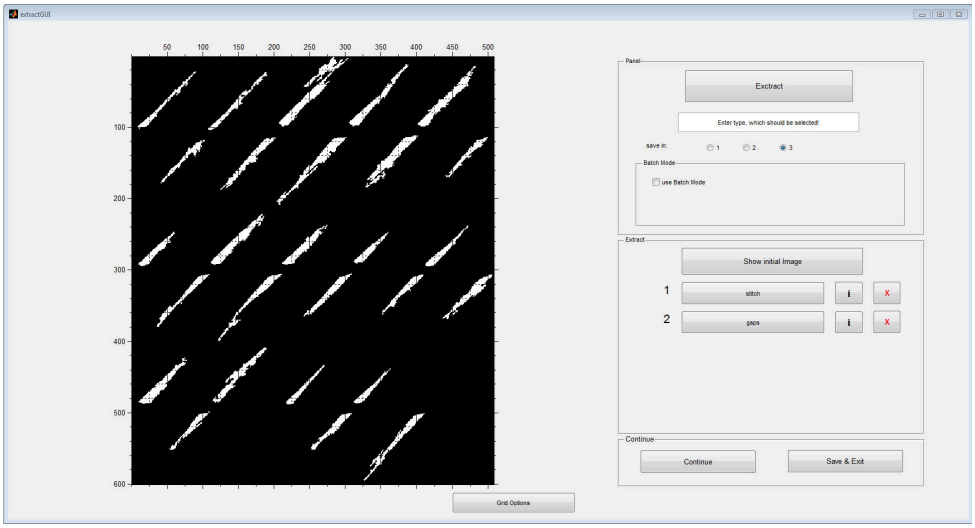

Figure. 4.6: FASTER GUI to extract domains

The segmentation in FASTER is comprised of the following three main steps:

- Gray-level thresholding
- Morphological filtering (optional)
- Add- / subtract-mode (optional)

Assessing the degree of gray-level within an black and white image and choosing pixels within a certain range, denoted as gray-level thresholding, is a very common procedure to segment images.

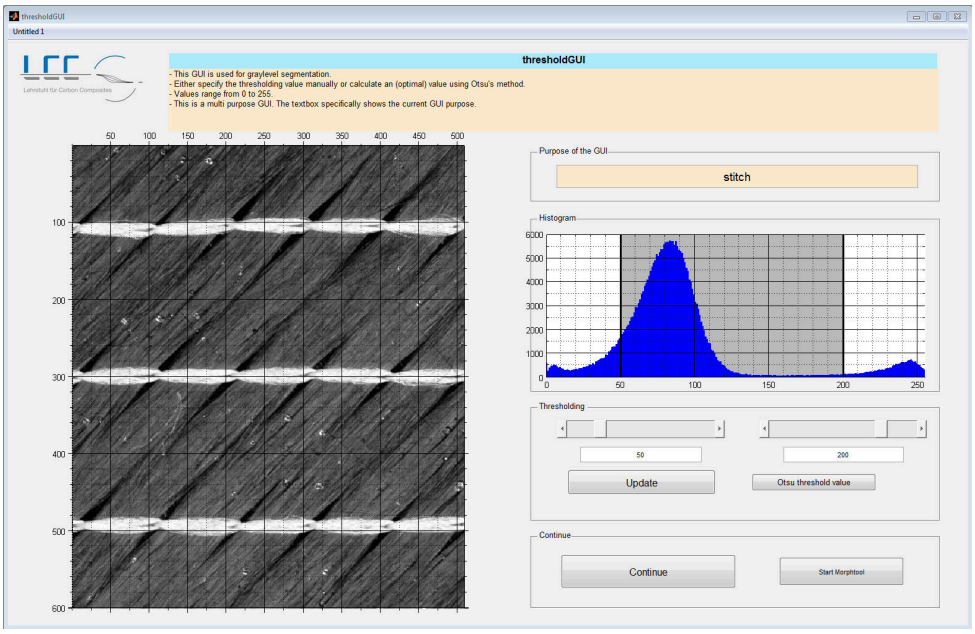

Figure. 4.7: FASTER GUI used to apply gray-level thresholding to segment images

In the ThresholdGUI (Figure 4.7), the image to be processed and its gray-level histogram are plotted. This allows to select a certain range of gray-levels by entering the appropriate limit values either by dragging the box over the histogram or by entering the values. By clicking *Update*, the segmentation results is visualized on the left as a binary image - containing only black or white pixels. To assess quality of the segmentation results, the original image can be overlaid and depending on the brightness of the image, the results from gray-level segmentation can be visualized in black or white pixels.

The second step of segmentation using FASTER is morphological filtering.

This is a crucial step as in the majority of the cases segmentation results after gray-level thresholding are of insufficient quality). That phenomenon is quite obvious as not all features to be extracted are represented solely by gray-levels. Morphological functions can be used to filter image noise by employing mathematically rigorous operations on binary images. The Morphtool, that is shown in Figure 4.8, developed by Brett Shoelson [128], utilizes most of the commonly-used functions.

Functions available in the Matlab image processing toolbox such as *imfill* are capable of filling holes, i.e. a group of foreign pixel within another domain can be switched. Furthermore, filtering tasks can be achieved, such as depicted in Figure 4.8. Here, agglomerations of false stitching pixels, that result from binder content can be cleared using *bwareaopen*.

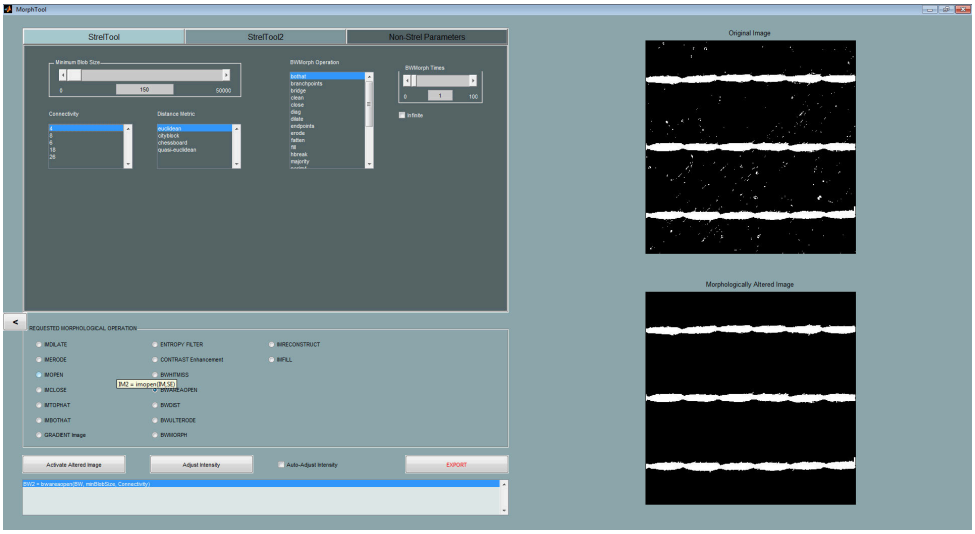

Figure. 4.8: Morphtool [128] for morpological filtering operations

After conducting morphological filtering, a GUI pops up asking the user whether it is desired to delete any unconnected part of the domain, such as a defect. For this two methods are available. The user can either subtract parts of the domain (*subtract mode*) by clicking on them or use the *add-mode* and hence has to add all domain parts that are considered as valid.

After the three steps of segmentation one gets back to the ExtractGUI where the procedure can be repeated as many times as desired.

Another very important feature of the ExtractGUI is the option for batch processing. During a segmentation run, every single adjustment is saved and exported to a text file. Within the ExtractGUI this text file can be loaded and a segmentation with exactly the same parameters can be repeated for a set of images. Here again, the reproducibility of the image acquisition procedure presented in Section 4.2 is of great help.

After segmenting the image into its domains, commonly fibers, stitching, gaps and foreign particles such as binder (optional), the image and all results information are ready for analyzing.

To allow measuring quantities in SI units, such as distances in meter, pixel information obtained from the images have to be converted using the correct image resolution. While loading every image the Exif information are extracted from the image. Exif data commonly contains the resolution, this value is used as default value in the ResolutionGUI depicted in Figure 4.9 but can also take any values. Images obtained with mold and scanner presented in Section 4.2 contain the correct resolution, in case the images have been taken with different systems resolutions may not be correct.

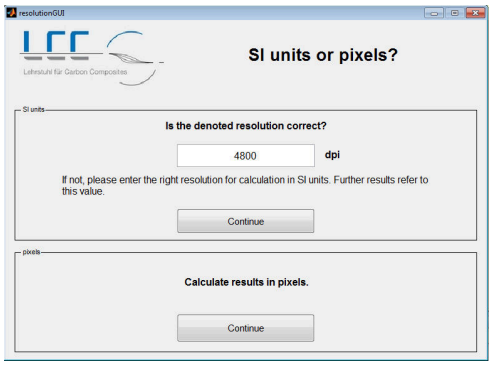

Figure. 4.9: FASTER GUI for conversion pixel to metric information

The analysis is conducted in the AnalysisGUI with its submenus, that are depicted in Figures 4.10 to 4.13. The AnalysisGUI provides the option to choose an image to be analyzed. The results of segmentation, stored as binary images, as well as the images available from the beginning of the FASTER run may be analyzed.

In fact, any analysis can be applied to any domain. However, it is not always meaningful. For the fiber domain the most important parameter to determine is the orientation. The window for Fourier analysis, depicted in Figure 4.10 provides several options that may be used prior to the determination of orientation in the *Edge Detection* section. In case the domain for analysis has not been segmented it can be caught up by applying a subtract operation. The fiber domain can be created by subtracting stitching and gaps from the original image. As will be explained more in detail in the next section, the algorithm in FASTER to determine fiber orientation is a combination of Canny edge detection followed by a Fourier transformation. For the edge detection small frazzles of lines can be suppressed which might result from foreign particles. The result of edge detection can be visualized. For determination of fiber orientation a grid is superimposed (Figure 4.10) onto the image. Fiber orientation is evaluated for each tile. These values are presented

by cross-fading grid and orientation lines onto the image in the visualization section on the left side of the GUI. Furthermore, a mean value is calculated and the values is shown. All results obtained during the analysis (even those not depicted in the GUI) are saved and can be exported to several formats (Figure 4.14).

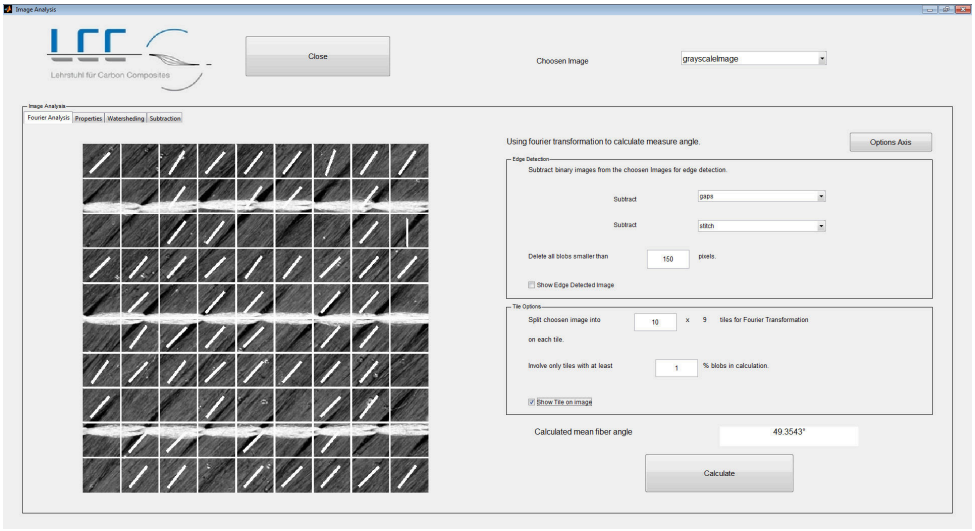

Figure. 4.10: FASTER GUI used to calculate fiber orientation

Images can be created by applying a subtract operations to the already existing images. The respective submenu is depicted in Figure 4.11. The new domain can be given a name, the result is visualized and the newly obtained can be consulted for further analysis same as the other images.

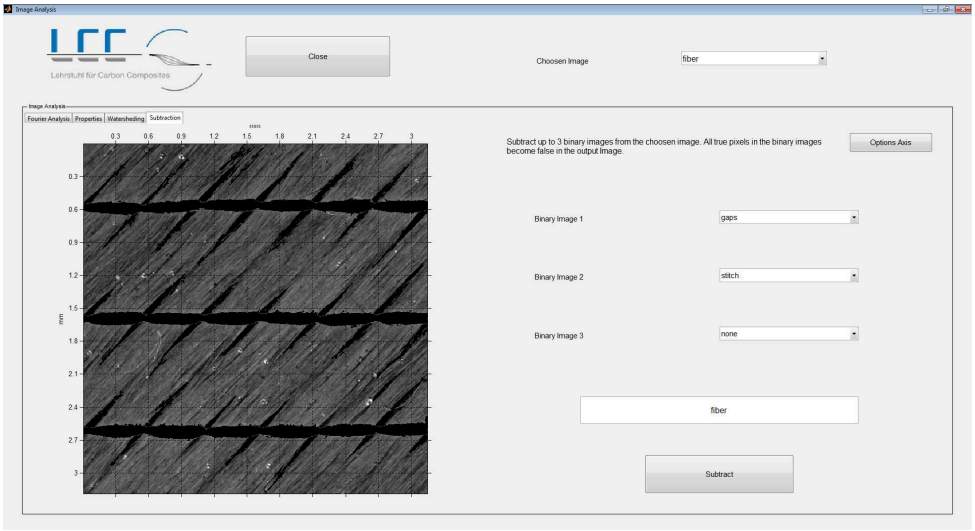

Figure. 4.11: FASTER GUI domain creation by applying a subtract operations

The PropertiesGUI provides functionality that can be applied to any domains, and is of great importance for analyzing gap and stitch domain (see Figure 4.12). The number of

items such as number of gaps is counted, their area, aspect ratio etc. are calculated. A curve fit is conducted for any item where orientation and length along major and minor axis are determined. Every pixel of an item is considered as a data point with coordinates x and y. The curve fit uses least-square fit technique to determine the gradient $\Delta y/\Delta x$ of a linear function that represents the orientation. The property analysis is important for calculating the number, dimensions and orientation of gaps.

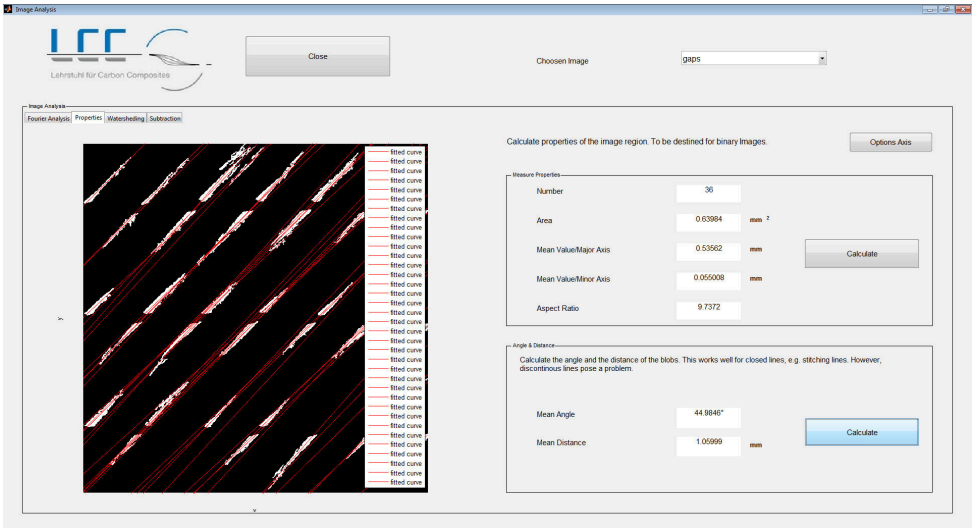

Figure. 4.12: FASTER GUI used to calculate domain properties

A function dedicated to examining the stitch domain is presented in Figure 4.13. The WatershedGUI can be used to determine the distance between the stitch lines. However, up to now it is not possible to segment stitch lines into its loops. To segment individual stitch loops, a watershed algorithm is employed that allows to segment the stitch lines and hence to determine the length of stitch loops.

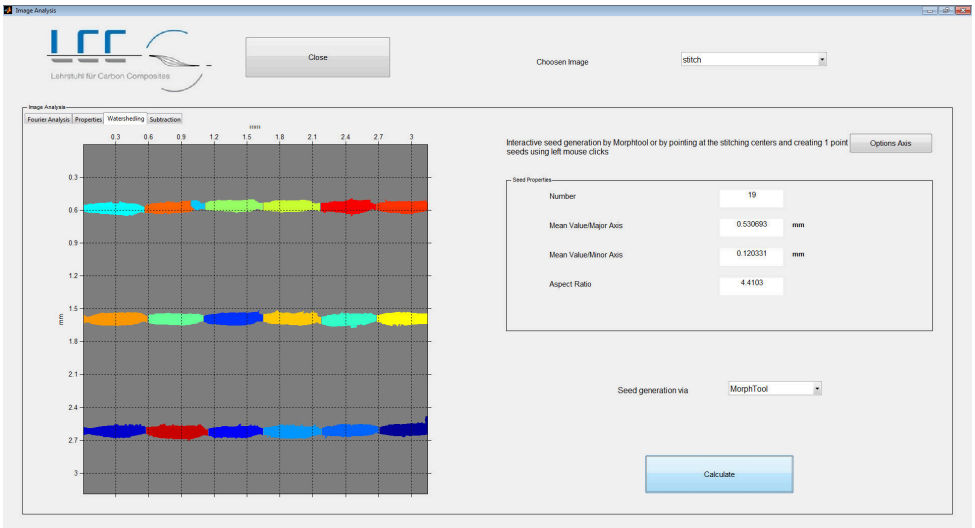

Figure. 4.13: FASTER GUI used to segment stitches by watershed transformation

The principle of watershed algorithms has been introduced in Chapter 2.5.2. The main advantage is that segmentation may be performed independently from the orientation of the respective domain. The only information required for applying watershedding are the starting points, called seeds. The GUI provides automatic determination of the seeds using the MorphTool. The seeds can also be set manually by clicking. The results of the watershed transformation, as visualized in Figure 4.13, are the stitch lines segmented into the loops, marked with different colors. A property analysis is conducted where the items are counted and their dimensions and orientations are calculated, similar to the PropertiesGUI.

No information is lost during the analysis. The SaveGUI, depicted in Figure 4.14, provides several options to save the information. Results from segmentation and analysis can be stored into XML-format as well as into a Matlab file (*.mat). XML-format has the advantage that it can be processed by any programming language and results can be visualized in any text editor. The results stored in Matlab format have the big advantage that they can be directly used in case one wants to proceed in Matlab and keep everything in the same environment. The images obtained during analysis, which can also be considered as results, can be stored in XML- and Matlab-format for the same reason as for the classic results. Additionally, it is also possible to save them in an uncompressed picture file in TIFF-format. The *Save Data* option usually comes along with big amount of data because all the entire workspace that has been used during the FASTER run is save to XML- or Matlab-format. Nevertheless, this can be useful in case one wants to study the functionality of the algorithms more in detail.

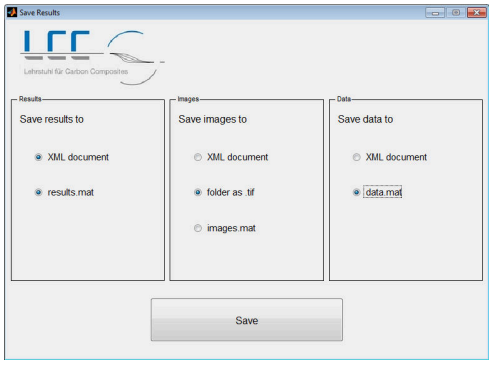

Figure. 4.14: FASTER GUI exporting results to certain formats

4.3.2 Image Processing Functions

In this section the algorithms implemented in the FASTER toolbox are presented in detail. The elementary steps are depicted in short format. For Matlab specific details refer to the source code of the FASTER toolbox.

Canny Edge Detection

Applying Fourier transformation to high-resolution gray-level images is computationally intensive. Fourier analysis searches for gradients in all orientations of an image. Detected gradients can be described using trigonometrical function in the frequency domain. For analysis of fiber orientation of FASTER a pre-processing step has been developed. Gradients are magnified using an algorithm for edge detection. For Fourier transformation the binary result image from edge detection can be employed. So, the computational cost for determination of fiber orientation is reduced significantly.

```
Averaging of input image using imfilter
Detection of edges using [103]
Creating binary image
Reinforcing edges using imdilate
Filtering of edge results using bwareaopen
```

Fourier Analysis for Determination of Fiber Orientation

The Fourier transformation has been optimized for performance. Depending on the grid size specified by the user, the Fourier transformation is applied to sub-sections of the image. After transformation, a curve fit is employed on the Fourier spectrum (such as in Figure 2.21, right) to determine the displayed orientations and thus the average fiber orientation for that sub-image.

```
Creation of square shape tiles for the analysis
While tile count > 0
  Fourier transformation using fft
  Fit of Fourier spectrum using fit
  Calculation of angle for each tile
  Tile count = Tile count - 1
Calculation of mean angle
Drawing results to the image
```

Watershed transformation

Although the functionality of watershedding is straightforward, coding the algorithm for high-performance requires special considerations. The image processing toolbox in Matlab provides an efficient function which has been employed here. However, in case Matlab is not available, a watershed algorithm can be set-up manually or found in literature such as Meyer [95].

```
Seed generation
   Manual:  Seeds are created by the user
   Automatic:  Morphological operation (i.e.  imerode) are employed
               to divide the loops
Perform watershed transformation using watershed
Result visualization
```

Curve fitting

Again, a function from the image processing toolbox in Matlab was employed here. The `regionprops` function is particularly suited for binary images and measurements on shape and pixel values can be performed. Quantities such as area, orientation, centroid, bounding box and various others may be determined by applying that function. All relevant geometric parameters for fabric modeling can be obtained by curve fitting assumed the segmentation results are available.

4.3.3 Parameter Study on Image Processing

Six non-crimp biaxial fabrics with different orientations, varying stitching patterns and differences in regularity are investigated. Table 4.2 provides an overview of the tested materials fabric characteristics. Scans of one layer of the fabrics are shown in Figures 4.15, 4.17 (front) and 4.16, 4.18 (rear).

Short-Name	**Manufacturer**	**Construction**		m_a $[g/m^2]$	t $[mm]$	V_f [%]
SGL 45	SGL Kümpers	Biax	$-45°$ / $+45°$	450	0.40	63.92
SGL 90	SGL Kümpers	Biax	$0°$ / $90°$	449	0.40	63.78
SAE 45-1	Saertex	Biax	$-45°$ / $+45°$	408	0.35	66.23
SAE 90	Saertex	Biax	$0°$ / $90°$	406	0.35	65.91
SAE 45-2	Saertex	Biax	$-45°$ / $+45°$	540	0.50	61.30
SIG 45	Sigmatex	Biax	$-45°$ / $+45°$	300	0.30	56.82

Table. 4.2: Overview of processed materials

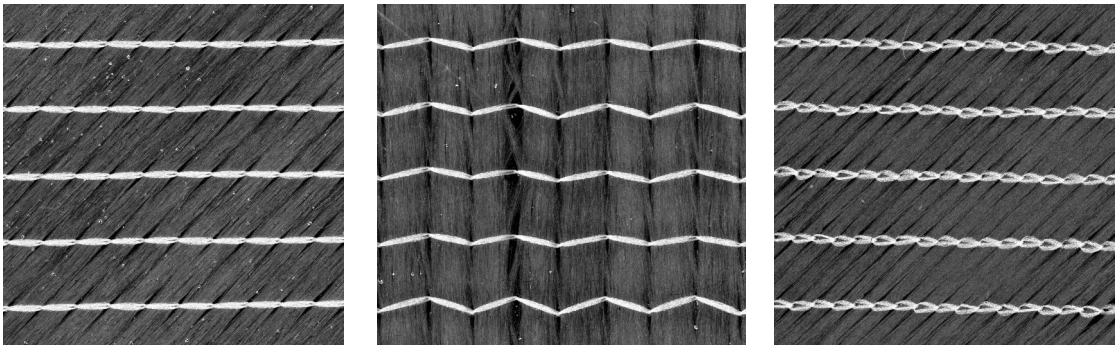

Figure. 4.15: Front sides: SGL 45 | SGL 90 | SAE 45-1

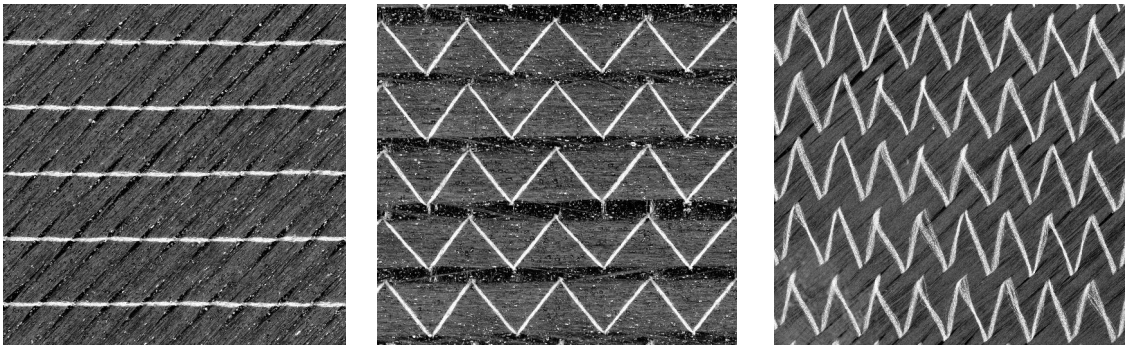

Figure. 4.16: Rear sides: SGL 45 | SGL 90 | SAE 45-1

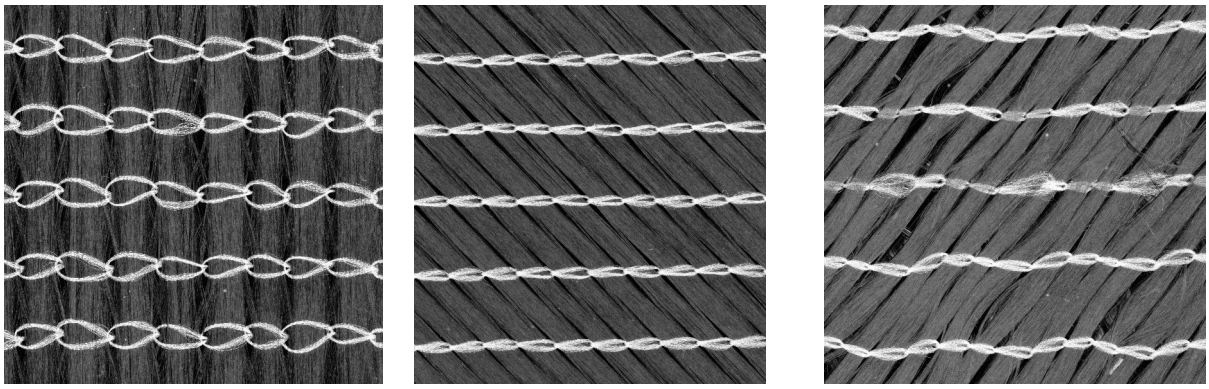

Figure. 4.17: Front sides: SAE 90 | SAE 45-2 | SIG 45

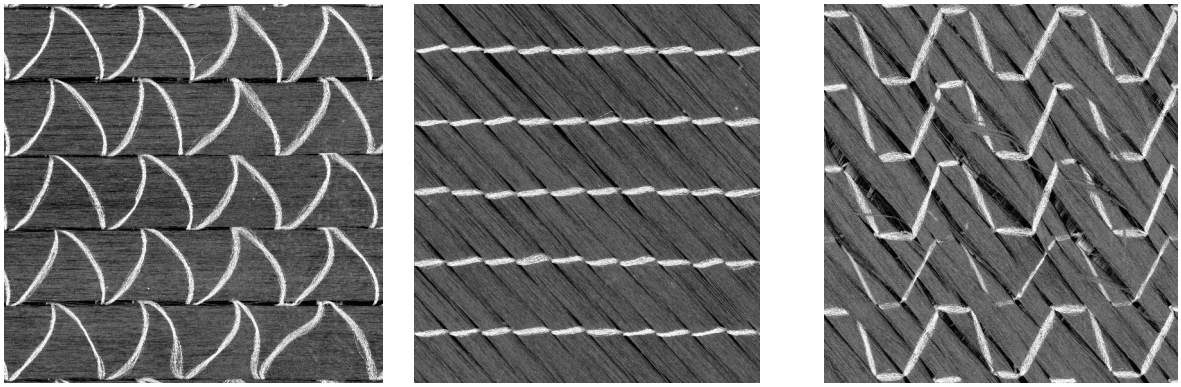

Figure. 4.18: Rear sides: SAE 90 | SAE 45-2 | SIG 45

Image Processing Result Format

In the following section, the results of image processing are shown in both tabular and image form. and as results images. Exemplarily, for all result images (see Figures 4.19 to 4.30), an explanation of the treatment realized is given:

- The respective images denoted with **(a)** show the fiber orientation results of the Fourier analysis. The images are overlaid with a grid, for each tile the fiber orientation of the fiber domain is evaluated and mean value as well as coefficient of variation are denoted in the respective results tables.
- Images labelled with **(b)** show the edges resulting from Canny edge detection that are used for Fourier transformation.
- Images denoted with **(c)** show the extracted stitch lines plus the individual stitches in different colors. The orientation of the stitching is shown by dotted lines fitted to the stitch lines. Furthermore, the gap domain is visualized in blue color.

SGL 45

The distinction of the stitch domain can be nicely achieved by gray-level thresholding, with a small amount of noise having to be cleared using morphological filtering. The results for the rear-side are influenced by the binder content, stitching shows to be jagged. This can be smoothed using morphological closing. The gaps appear to be very small. However, the image resolution is high enough that they can be segmented. The small size causes holes within the gaps which can be closed morphologically. Generally, the gap size varies significantly, with deviations from the mean value of 120% occur. For further analysis based on unit cells, it is recommended to use mean values from a wide homogenization area (see Tables 4.19c and 4.20c). The canny image comprises mostly long edges which suits the Fourier analysis. Although, there are round and oval objects, the orientation can be determined robustly. The coefficient of variation is smaller than 2.5% for front- and rearside (see Figures 4.19 a/b and 4.20 a/b). All measures are reported in Table 4.3.

Property	**Front**	**Rear**
Fiber orientation (CoV)	$+45.6°(2.4\%)$	$-44.5°(1.6\%)$
Gap fraction	3.8%	1.6%
Mean gap length	$2.2mm$	$2.9mm$
Gap aspect ratio	10.0	10.0
Stitch fraction	10.0%	5.9%
Stitch length	$5.1mm$	$5.1mm$
Stitch distance	$2.8mm$	$2.8mm$

Table. 4.3: Analysis results for material SGL 45

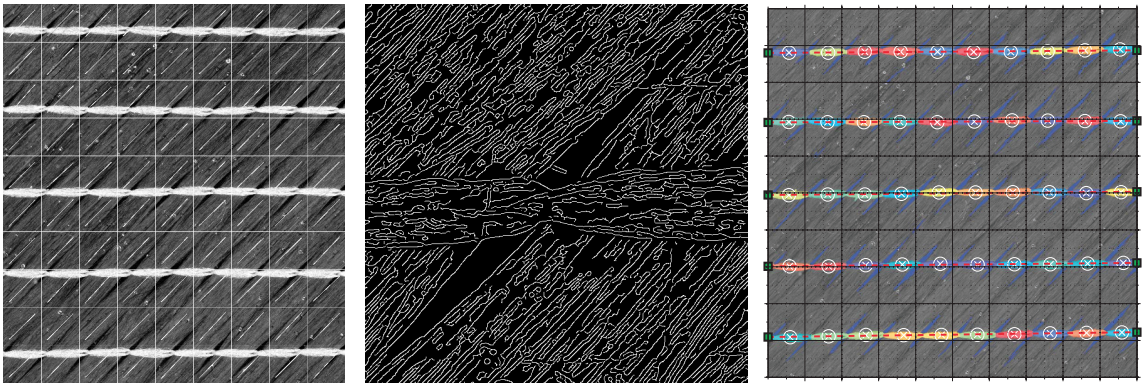

(a) (b) (c)

Figure. 4.19: Results images for front sides of material SGL 45

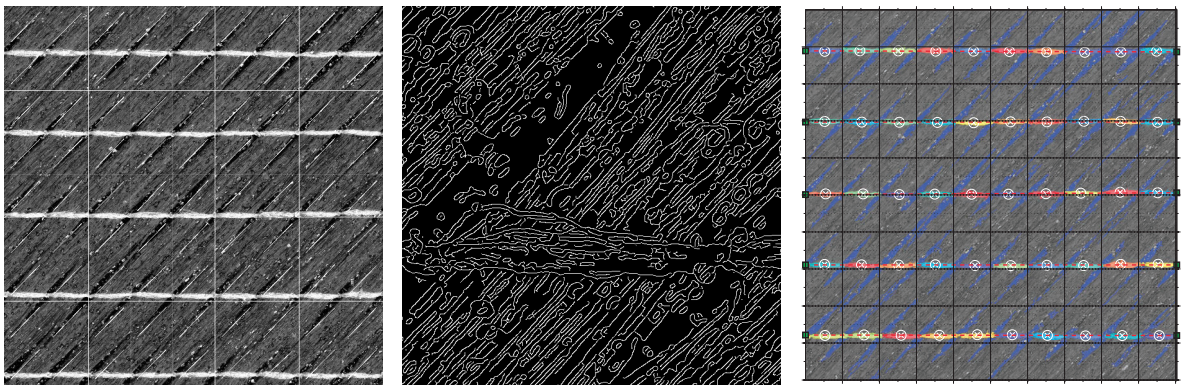

(a) (b) (c)

Figure. 4.20: Results images for rear sides of material SGL 45

SGL 90

For SGL 90 segmentation of stitching works well. At the edges where stitch loops meet morphological closing has to be employed, especially for the rear side. Extraction of individual loops is a little tricky for the backside. Due to the change of orientation, the seed points for water shedding have to be specified manually. This causes the loops to 'fill' irregularly and hence the size of the loops is calculated slightly different for each one. However, calculation of the mean value cleans that issue. At the front side, there are two types of gaps. Firstly, there are bigger continuous channels and secondly smaller individual gaps. It is hard the segment the two types together. It is crucial to find suitable parameters for morphological operations, that the smaller gaps do not vanish. At the backside, just continuous channels can be found which comes along with the type of stitching. Here, segmentation of the gap domain is easier as for the front side (see Figures 4.21c and 4.22c). The determination of the fiber orientation works robust for the front side. For the backside, however, big problems arise. The fiber bundles are quite regularly which caused the canny algorithm not to find enough edges (gradients). Secondly, the

binder leads to big round and oval edges that have a huge impact on the calculated fiber orientation (see Figures 4.21 a/b and 4.22 a/b). All measures are reported in Table 4.4.

Property	**Front**	**Rear**
Fiber orientation (CoV)	$+91.7°(2.9\%)$	$-66.4°(28.1\%)$
Gap fraction	4.4%	15.7%
Mean gap length	$1.8mm$	$6.7mm$
Gap aspect ratio	4.6	7.5
Stitch fraction	8.7%	8.3%
Stitch length	$5.1mm$	$5.1mm$
Stitch distance	$3.8mm$	$6.1mm$

Table. 4.4: Analysis results for material SGL 90

(a) (b) (c)

Figure. 4.21: Results images for front sides of material SGL 90

(a) (b) (c)

Figure. 4.22: Results images for rear sides of material SGL 90

SAE 45-1

For SAE 45-1 segmentation of stitching works well. The shapes are quite regular on both sides; just on the backside some stitch bundles are jagged which can be cleaned morphologically. The gaps are small on both sides but rather regular and they have a clear triangular shape. On the front side segmentation works well. On the backside gray levels of fibers and gaps are very similar; this causes some difficulties for extraction (see Figures 4.23c and 4.24c). Segmentation and analysis of the fiber domain is straightforward here. The values for front and backside as well as the low CoV show that nicely (see Figures 4.23 a/b and 4.24 a/b). All measures are reported in Table 4.5.

Property	**Front**	**Rear**
Fiber orientation (CoV)	$+44.3°(3.8\%)$	$-45.9°(6.6\%)$
Gap fraction	10.0%	10.0%
Mean gap length	$2.1mm$	$2.2mm$
Gap aspect ratio	11.9	7.6
Stitch fraction	12.7%	22.3%
Stitch length	$5.1mm$	$5.1mm$
Stitch distance	$1.7mm$	$4.4mm$

Table. 4.5: Analysis results for material SAE 45-1

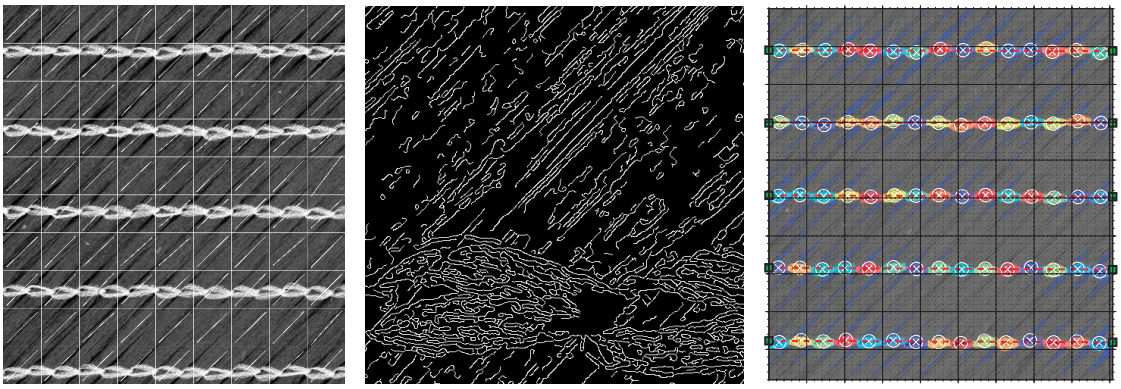

(a) (b) (c)

Figure. 4.23: Results images for front sides of material SAE 45-1

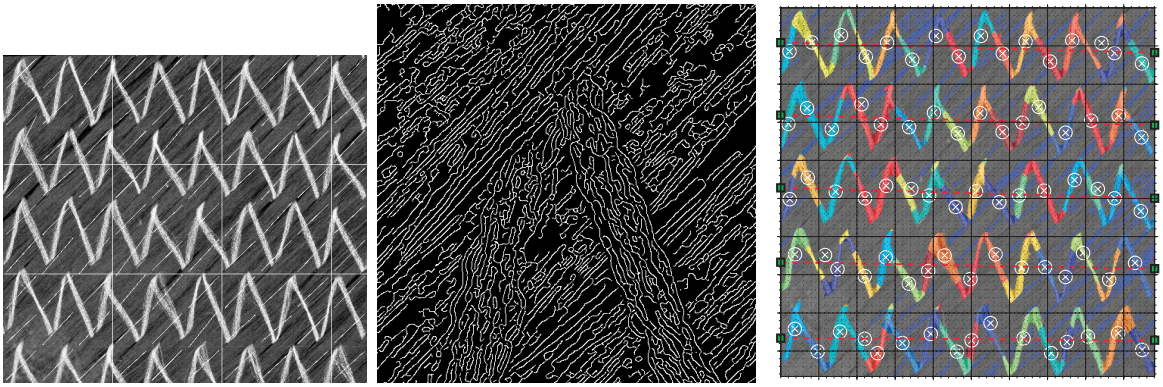

(a) (b) (c)

Figure. 4.24: Results images for backsides of material SAE 45-1

SAE 90

For both sides, the stitching can be clearly separated from the two other domains due to the difference in brightness (gray-levels between 250 and 255). On the backside the endpoints of the loops have to be closed manually. The gaps on the front side are hard to detect. At first, they are not clearly defined, a lot of filaments are crossing the gaps and the gaps are inhomogeneous. On the backside, the same problem occurs, but segmentation is possible. The segmentation results can be reviewed in Figures 4.25c and 4.26c. The inhomogeneity on the front side that causes problems for the gap analysis is advantageous for the fiber orientation analysis. Here, irregularity means a lot of gradients which simplifies edge detection and Fourier transformation. On the <e bundles are very homogeneous, but orientation analysis is possible (see Figures 4.25 a/b and 4.26 a/b). All measures are reported in Table 4.6.

Property	**Front**	**Rear**
Fiber orientation (CoV)	$+91.0°(4.3\%)$	$-3.9°(45.0\%)$
Gap fraction	34.9%	2.9%
Mean gap length	$2.6mm$	$1.0mm$
Gap aspect ratio	2.1	8.1
Stitch fraction	31.0%	16.3%
Stitch length	$5.0mm$	$5.1mm$
Stitch distance	$3.2mm$	$6.0mm$

Table. 4.6: Analysis results for material SAE 90

(a) (b) (c)

Figure. 4.25: Results images for front sides of material SAE 90

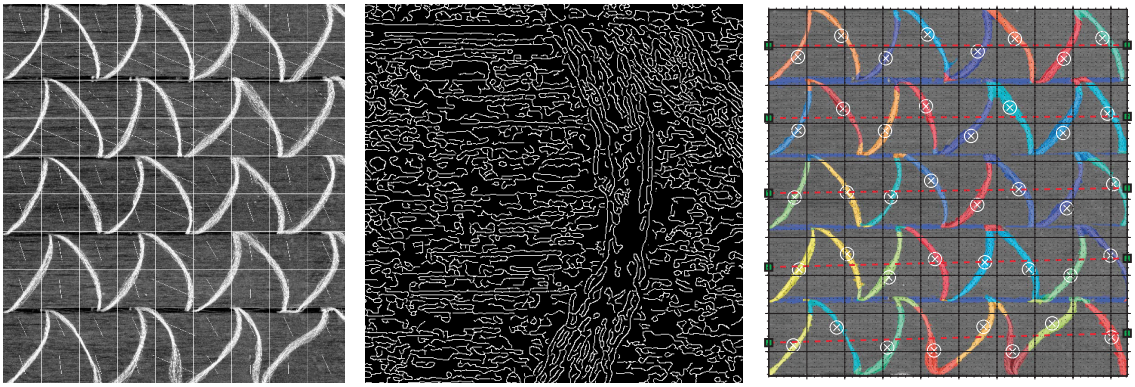

(a) (b) (c)

Figure. 4.26: Results images for backsides of material SAE 90

SAE 45-2

For material SAE 45-2 an efficient image processing is possible. All methods can be applied in automatic mode and the analysis is robust, the results are of high quality (e.g. COV for fiber orientation smaller 0.6%) and are highly credible. Initially, the gray level histogram shows an almost perfect tri-modal shape, i.e. three disticnt peaks representing the three domains. There are similarities to material SGL 45, but SAE 45-2 has no binder.

So, there is no negative influence on the segmentation at all. Based on the segmentation of the entire stitching domain, the loops can be separated easily. Even the automatic seed generation for water shedding can be employed. The results can be reviewed in Figures 4.27 and 4.28. All measures are reported in Table 4.7.

Property	**Front**	**Back**
Fiber orientation (CoV)	$+43.0°(0.6\%)$	$-49.6°(0.5\%)$
Gap fraction	4.5%	32.0%
Mean gap length	$3.7mm$	$3.5mm$
Gap aspect ratio	16.6	19.8
Stitch fraction	13.7%	7.4%
Stitch length	$5.1mm$	$5.2mm$
Stitch distance	$2.7mm$	$2.6mm$

Table. 4.7: Analysis results for material SAE 45-2

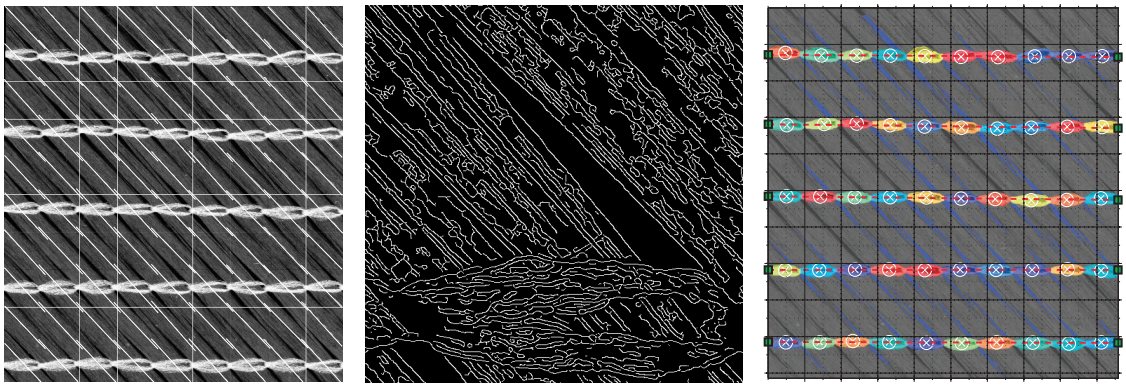

(a) (b) (c)

Figure. 4.27: Results images for front sides of material SAE 45-2

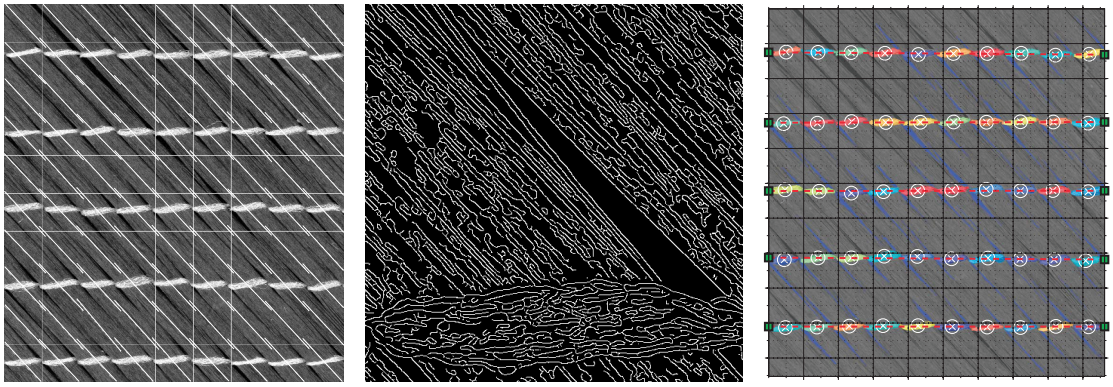

(a) (b) (c)

Figure. 4.28: Results images for backsides of material SAE 45-2

SIG 45

Material SIG 45 is very inhomogeneous which can be seen clearly at the scans. For the gray level histogram that has no influence, so segmentation is possible. The binary images show the inhomogeneities very well gaps have different sizes and completely different shapes. The stitches show the same which complicates calculation of geometrical properties. That's why this step is suspended for the analysis. The distance between the stitch lines as well as their orientation can be measured because the values are based on the mean values of the geometry of the individual stitches. The results can be reviewed in Figures 4.29 and 4.30. All measures are reported in Table 4.8.

Property	**Front**	**Back**
Fiber orientation (CoV)	$+52.0°(0.6\%)$	$-52.0°(0.5\%)$
Gap fraction	–	–
Mean gap length	–	–
Gap aspect ratio	–	–
Stitch fraction	14.5%	15%
Stitch length	$5.5mm$	–
Stitch distance	$2.3mm$	–

Table. 4.8: Analysis results for material SIG 45

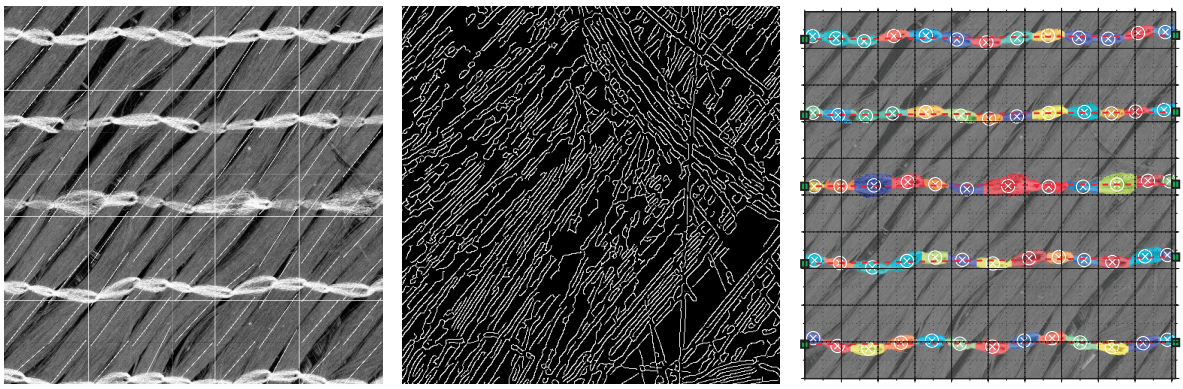

(a) (b) (c)

Figure. 4.29: Results images for front sides of material SIG45

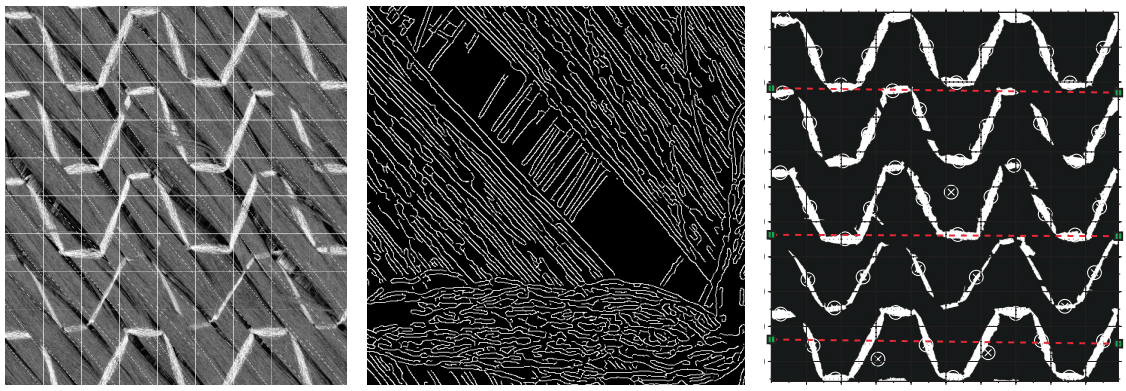

(a) (b) (c)

Figure. 4.30: Results images for backside of material SIG 45

Summary

The algorithms prove to work robustly with most of the tested fabrics and are capable of extracting all information required for textile modeling. In general, the more homogeneous a fabric is, the easier it is to analyze. The segmentation of the domains is always possible so that all relevant quantities for textile modeling can be approximated. Only geometric quantities such as dimensions and angle properties cannot necessarily be determined for all fabrics. Due to the inhomogeneity of fabrics the question comes up how big the sample size (image size) has to be so that representative quantities can be determined. The size of the representative volume depends on the overall property to homogenize. This topic is of great importance and should be addressed in future research. The calculation of fiber orientation is well possible and robust.

4.4 Unit Cell Modeling and CFD Analysis

4.4.1 WiseTex XML Interface

In collaboration with Lomov et al. [121], an XML- and a scripting interface has been developed and added to WiseTex.

WiseTex and FlowTex are handled using the GUIs. Model manipulation using external tools has not been possible so far. The new XML interface provides the option to save / read any fabric model to / from XML text files. Hereby, adaptions to models, such as the variation of yarn-with for a parameter study, can be performed using a text editor and together with the scripting interface the models can be processed efficiently. Figure 4.31 shows the hierarchical structure of a WiseTex model visualized in an XMl text editor.

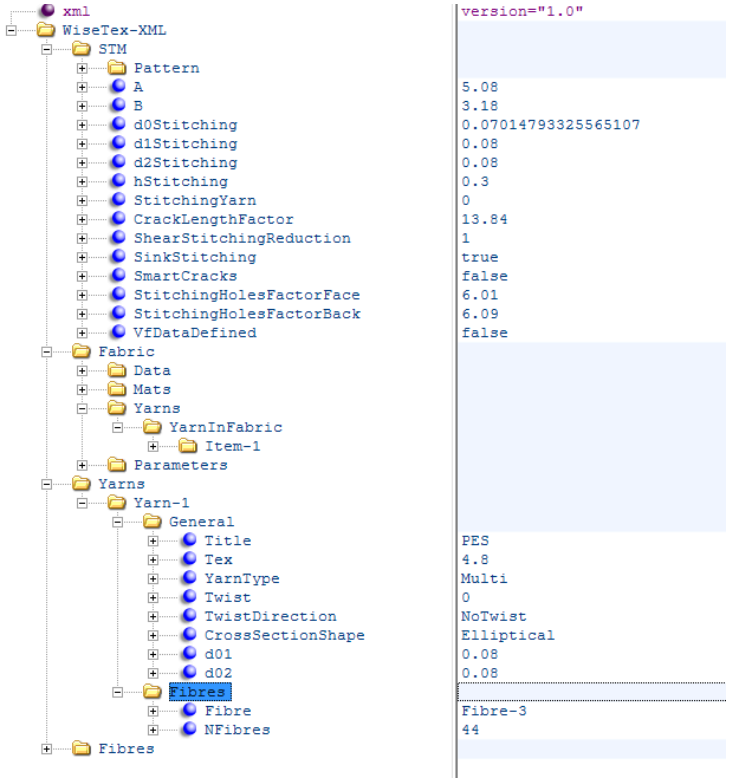

Figure. 4.31: WiseTex stitched mat model (stm) in XML format shown in XML Notepad editor

4.4.2 WiseTex Scripting Interface

With the ability to execute commands in a script, it is now possible to program complex calculation tasks. Table 4.9 and the following enumeration present essential tasks of the software tools WiseTex, TexComp and FlowTex and the respective syntax for scripting. A more-into-detail collection is given by the WiseTex documentation files that are provided with every WiseTex installation package.

Software	Function	Command Syntax
WiseTex	Generic command syntax[2]	WiseTexCL <TEX file> <GEO file> <mode>[:<options>]
	Create a geometrical model of relaxed fabric	WiseTexCL <TEX file> <GEO file> build
	Create a geometrical model of compressed fabric[3]	WiseTexCL <TEX file> <GEO file> compress:<p>[,<p>] ...
	Create a geometrical model of the fabric, deformed in plane[4]	WiseTexCL <TEX file> <GEO file> in_plane: <gamma>,<epsX>,<epsY> [;<gamma>, <epsX>,<epsY>] ...
	Write a voxel file[5]	WiseTexCL <GEO file> <VOX file> voxels:<Nx>,<Ny>,<Nz> [;D]
TexComp	Calculate a stiffness matrix of the composite[6]	TexCompCL <GEO file> <matrix data> <stiffness file> [CS:<phi>] [VF: <vf>]
FlowTex	Calculate permeability of the fabric[7]	FastFDFlowTex W <VOX file> WX [WA <angle>]
		< ... > text string to be specified [...] parameter can be omitted ... repeat of the previous element.

Table. 4.9: WiseTex command line interface

4.4.3 FlowTex Voxelization Algorithm

Together with De Greef et al. [123], a new algorithm for voxel discretization of WiseTex models has been developed. The old algorithm investigated all yarns and mats to determine the actual membership of a voxel. This takes an unnecessarily large amount of time as it scaled particularly poor with an increasing number of yarns.

[2]The command creates GEO model of the <output file> based on TEX data in the <input file>. <mode> specifies the function and/or deformations applied to the unit cell; <options> are the model and computation parameters

[3]p is the applied pressure in MPa; if more than one p-parameter is given, then a set of GEO files is generated with p-values added to the file names

[4]gamma is the shear angle in degrees, epsX and epsY are tensile deformations in X- and Y-directions

[5]Voxel file: the name of the text file, which will contain description of the voxels Nx, Ny, Nz: number of divisions of the unit cell in three directions if D is specified, then local permeabilities for Brinkmann calculations are written to the voxel file

[6]Matrix data: XML file containing values of Young modulus and Poisson coefficient for the matrix stiffness file contains the result of the calculation: stiffness and compliance matrices and engineering constants in the co-ordinate system CS defined by angle phi of the in-plane rotation; vf is the FVF if different from the one defined by GEO data

[7]WX specifies the flow direction (could be also WY or WZ) WA specifies the angle of the unit cell of the GEO model. The results of the calculation (permeability values) are written in the ASCII file FlowTex_results.txt

The new algorithm is based on a flooding fill or tint fill algorithm which is perfectly suited for geometric shapes that are quite complex as a whole but have clearly defined local shapes as borders, such as yarns. The algorithm to flood the yarns reads as follows:

```
For each yarn in fabric
   Create voxel queue containing starting voxel
   Create index queue containing the corresponding yarn section index
   While queue is not empty do
      Pop voxel and index from queues
      Determine S-value of voxel by trigonometry
      If s < smallest s then
        Push voxel back on voxel queue
        Push index-1 on index queue unless index = 0
      Else if s > largest s then
        Push voxel back on voxel queue
        Push index+1 on index queue unless index = N
      Else
        If voxel is within local yarn-dimensions then
          Store data in voxel
          Push neighbours of voxel on queues
```

5 Application

This chapter discusses the simulation approach with particular emphasis placed both on the sensitivity of mesh refinement and deviations of model parameters. The resulting permeability values from the simulation approach are presented. Following this, the results of RTM experiments including detailed process monitoring are presented. These form the basis for comparison of the simulation approach to real-world RTM manufacturing.

5.1 Application of the Simulation Approach for Permeability Prediction

5.1.1 Parameter Study on FlowTex Non-Crimp Fabric Models

Sensitivity Study

Prior to modeling non-crimp fabrics based on input data from image processing, a parameter study has been conducted investigating the influence of model variations on permeability. Table 5.1 shows the specifications of the employed non-crimp fabric model used in these simulations.

Model specification	
Type	STM[1]
RVE Size $[mm]$	3.250 x 5.17 x 0.58
$n_{Voxel}(x,y,z)$	202208 (89 x 142 x 16)
V_f [%]	52.6
Solver[2]	Stokes
precision	10^{-4}
max. iterations	300
iteration restart	250

Table. 5.1: STM model specifications for parameter study

The model denoted as *reference* in Table 5.2 is a non-crimp fabric model set-up in WiseTex for parameter studies and is not an exact representation of one the tested fabrics in that

[1]Stitched mat model (STM), WiseTex specific wording

[2]Solver adjustments are specialized commands for the Stokes solver implemented in FlowTex. Their denotation in detail can be reviewed in the FlowTex users guide [129].

work. The results presented in Table 5.2 highlight the parameters that have a significant influence on the resulting permeability calculation. Neglecting stitch yarns in the model, hence reducing the model complexity to an uni-directional ply (UDP) model has the biggest influence on permeability; The permeability compared to the reference model is more than five times higher. However, this parameter will not be considered as neglecting the stitching yarns significantly alters the model structure. Neglecting intra-yarn flow also results in a big difference in permeability. Accounting for intra-yarn flow means that the fiber domain is considered as permeable in FlowTex and a permeability value is calculated analytically based on the packing density using the model provided by Gebart [27]. The result seems to be realistic because restricting the fluid from flowing within the fiber bundles would reduce the permeability significantly, which is also represented by the model where the permeability values is 78% lower compared to the reference configuration. Variations on geometrical features in the model such as crack[3] width and length have an influence. The permeability adapts almost linearly to changes of crack width whereas permeability is more sensitive to changes of the crack length. The influence of the tow dimensions is low. This is expected as maintaining all model parameters constant and only changing tow height or width will alter the model dimensions but not so much permeability.

Parameter Set	$\mathbf{K_{xx}}$ $[10^{-10}\ m^2]$	$\mathbf{\Delta}$[%]
Reference	8.22	-
No stitching	52.5	+554
No intra-yarn flow	1.73	−78.4
Gap width +10%	9.11	+13.5
Gap width -10%	7.06	−12.0
Gap length +10%	10.1	+26.2
Gap length -10%	6.08	−24.3
Tow thickness +10%	8.15	+1.56
Tow thickness -10%	7.87	−1.85
Tow width +10%	8.15	+1.57
Tow width -10%	7.90	−1.52

Table. 5.2: Results of a parameter study conducted on a WiseTex STM model

In conclusion, the biggest changes on permeability can be observed by changing the entire model structure or the solver, i.e. neglecting stitching or intra-yarn flow. Gap dimension have a influence, and thus they have to be carefully determined. Tow dimensions can be neglected.

[3] *Crack* is used in WiseTex terminology and can be seen as synonyme for the expression *gap* that is also used in this thesis.

Mesh Refinement Study

The previous study has shown the dependency of permeability results on geometrical variations. The study assesses the dependency of the results on the discretization level used and therefore the number of voxels. A very similar STM model is set-up in WiseTex and permeability is calculated based on meshes with a voxel number ranging from 10^4 to $1.2 \cdot 10^6$ which can be followed in Table 5.3.

Model specification									
Type	STM								
Size $[mm]$	3.25 x 5.17 x 0.58								
n_{Voxel} $[10^3]$	10	19	46	806	1466	234	353	619	1212
V_f [%]	53.78	53.65	53.69	53.70	53.69	53.70	53.71	53.71	53.71
Discr. step $[mm]$	0.1	0.08	0.06	0.05	0.04	0.035	0.03	0.025	0.02

Table. 5.3: Parameters for a mesh refinement study on a WiseTex STM model

Figure 5.1 depicts the results of the mesh refinement study. It is clear that the number of voxels has a significant impact the on calculated permeability. Calculations of models by neglecting intra-yarn flow (no IYF) can be performed on meshes up to $1.2 \cdot 10^6$ voxels. For that adjustments the result is still dependent on the discrezization but the impact of element size is significanlty lower for meshes with more than $6 \cdot 10^5$ elements compared to more coarse discretizations. For calculations accounting for intra-yarn flow (IYF), problems with the solver begin to occur for meshes with $6 \cdot 10^5$ voxels. The FlowTex users guide [129] suggests to alter the *iteration restart* value to obtain convergence. Thus, for the calculations of models with voxel numbers higher than $2.3 \cdot 10^5$ the *iteration restart* value has been reduced from its default values 250 so that the solver could obtain a result. The finest discretization where it was possible to obtain a results was for a mesh with $6.19 \cdot 10^5$ voxels. $6 \cdot 10^5$ was therefore the voxel number chosen for the models including intra-yarn flow in this chapter.

The current Stokes solver implemented in FlowTex version doesn't provide an option to parallelize solving over multiple cores. Conversion of FlowTex voxel files to common multi purpose CFD solvers, hence enabling the analysis of bigger models due to parallelization is part of ongoing research. Scripts to convert a FlowTex voxel file to an Ansys compatible format have been developed and first results will be presented at ECCM-16 conference [130].

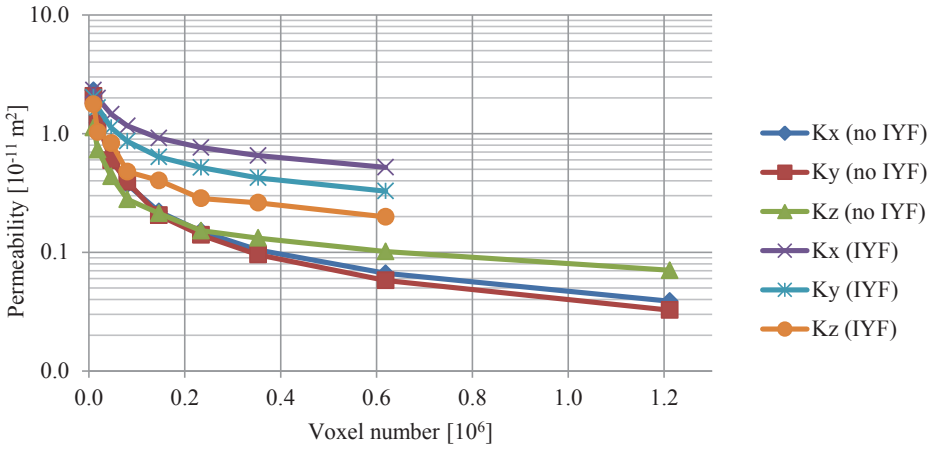

Figure. 5.1: Results of a mesh refinement study conducted on a WiseTex STM model

5.1.2 Comparison with Experimental Results

The main goal of the following section is to model the SAE 274 and SAE 540 fabrics and predict their permeability by applying the simulation approach as presented in Chapter 4. Both of these fabrics have been experimentally tested and hence their permeability values are known.

Model Specifications

Based on a priori known quantities such as V_f and resulting thickness of the lay-up, all properties specifications have been determined based on results from the simulation approach. Table 5.4 summarizes the model specifications. Before assessing the permeability results, one can state that all relevant information for modeling can be determined with the simulation approach or are known a priori.

Domain	Symbol	Description	Unit	SAE 274	SAE 540
Fiber	V_f	Fiber volume fraction	[%]	50.3 / 53.6	50.5 / 55.1
	t_i	Thickness of ply	[mm]	0.30 / 0.275	0.60 / 0.55
	a_i	Orientation of ply	[°]	-45 / 45	
	d_{fil}	Filament diameter	$[\mu m]$	7	
	ρ_{fil}	Fiber density	$[\frac{g}{cm^3}]$	1.77	
	tex	Fiber linear density, tex	$[\frac{g}{km}]$	12	
Stitching		Pattern (Notation [76], [69])		Franse ("1:/0")	
	L	Spacing length	[mm]	5.08	
	W	Spacing width	[mm]	3.18	
	d_{yarn}	Yarn diameter: $d_{01} = d_{02}$	[mm]	0.08	0.10
Gaps[4]	a	Aspect ratio	[-]	13.84	21.56
	k_f	Size ratio for gaps front	[-]	6.01 / 5.93	2.89 / 2.50
	k_b	Size ratio for gaps back	[-]	6.09 / 5.98	3.90 / 3.72

Table. 5.4: Model specification for SAE 274 and SAE 540

Rotation of FlowTex Models

A constraint within FlowTex is that permeability may only be evaluated along the main axes of the cartesian coordinate system X, Y and Z. Hence, in-plane only two orientations can be evaluated. However, a principal in-plane permeability tensor requires three permeability results along independent directions, e.g. 0°, 45° and 90°.

Rotating models directly at their origin in WiseTex is not possible. Hence, an algorithm has been developed that creates a rotated voxel file for the FlowTex solver based on an initial input voxel file.

The routine executes the following steps:

```
Create a 3D binary array from the text string in the voxel file
Extend array using repmat
Rotate and Crop the array using imrotate and imcrop
Write a new (rotated) voxel file
```

This procedure is straightforward for models that neglect intra-yarn flow.

The vox-file contains a string of either `S` (solid domain) or `F` (fluid domain) and during the rotation procedure, this string is re-arranged. Therefore, the model is not altered structurally but reoriented. It has to be ensured that the rotated models contain at least one complete unit cell to provide representative information.

[4] All specifications of the gap domain have been calculated based on the results from image processing using FASTER

Rotation of a model accounting for intra-yarn flow is more complex as the voxel contains `F` fluid voxels and Brinkmann points `B` followed by another string containing orientation information of that voxel; six tensor entries representing a 3D symmetric orientation tensor. This tensor could be rotated, however this has been omitted here due to significantly increased computational cost.

For the results shown in the following sections, the rotate procedure has been applied to the models neglecting IYF and the resulting factor between K_0 and K_{45} of the models neglecting IYF has been applied to models with IYF.

Comparison of Results

The models employed for a comparative study have been discretized using $\approx 430{\cdot}10^3$ voxels and taking into account intra-yarn flow. This degree of mesh refinement assured that all models could be solved properly without any iteration problems or memory overflow. Periodic boundary conditions were employed along all coordinate axes.

Figure 5.2 depicts the results for the SAE 540 material and Figure 5.3 the results for the SAE 274. At first glance the difference between the results is low when considering that they have been obtained using completely different techniques. Results denoted as *experimental* have been obtained with the setup described in Chapter 3 whereas the results denoted as *simulated* are solely based on fabric models created using the output from image processing and the entire simulation approach presented in Chapter 4. This highlights the suitability of the use of simulation approaches to determine fabric permeability.

Assessing the results in greater depth reveals that the simulation approach overestimates the difference between results for the different test directions. The difference of 0° and 90° results is lower for the experimental results. Moreover, the simulation approach underestimates results for the SAE 540 and overestimates the results for the SAE 274, particularly in the 0°-direction. The trend for decreasing permeability with increasing V_f is reflected in both materials. The differences between experimental results and those from the simulation approach mainly arise from two sources: textile modeling and the fact that 2D images are used for 3D modeling. Unit cell modeling of non-crimp fabrics using WiseTex introduces certain simplifications that cause deviations of the model from the real fabric architecture. For example, the cracks in the fabric introduced by the stitches are modeled as wedge shaped volumes with planar bounds.

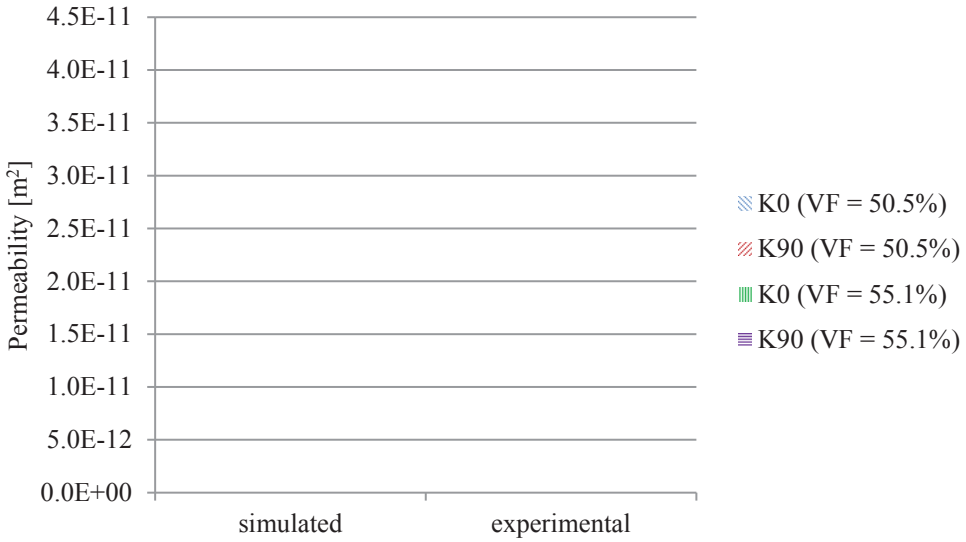

Figure. 5.2: Simulated and experimental permeability results of SAE 540

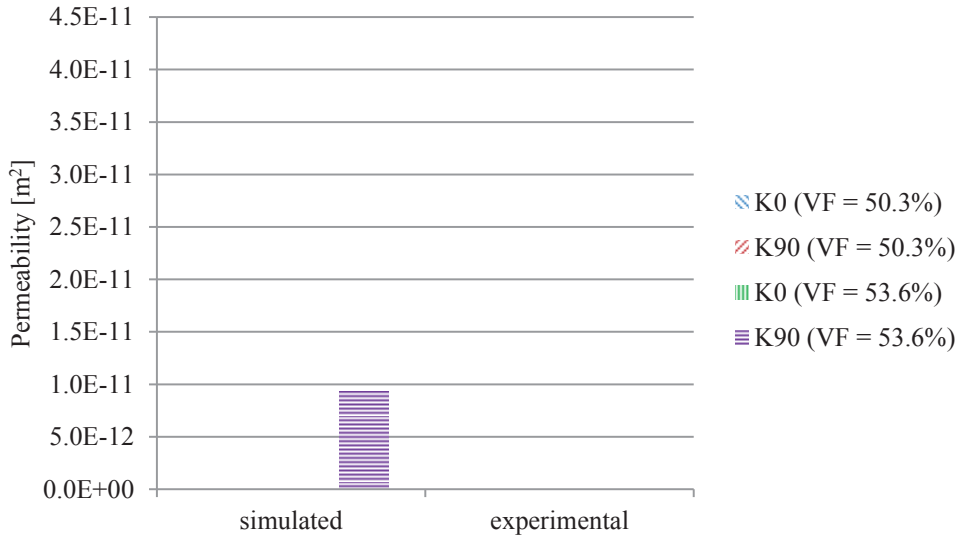

Figure. 5.3: Simulated and experimental permeability results of SAE 274

As a concluding remark, it has to be stated that although the comparison of experimental results and those obtained using the simulation approach showed good results for the employed materials, it cannot be considered as universally correct. Precaution and critical assessment of the results when applying the simulation approach to other materials is highly recommended.

5.2 RTM Experiments on Part Level for Comparison to RTM Modeling

A number of RTM experiments were performed in order to obtain a basis for comparing the experimental results with ones obtained through the simulation approach. The mold that was used was developed by M. Arnold, a colleague at the IVW at TU Kaiserslautern, within his PhD thesis. Its dimensions (approximately 700 x 700 mm) and particularly the level of complexity, with a dome and a exaltation containing edges with radii in a range typical for automotive bodywork components, make it suitable for the application of the simulation approach.

The main goal of this study was to obtain a measure of how well resin flow during RTM manufacturing along a complex geometry can be predicted by applying the simulation approach for permeability prediction. For this, not only the RTM experiments were conducted but also a study was carried out assessing the increase of resin viscosity over time for different processing temperature. Furthermore, the preforms used for injection were optically assessed to determine the repeatability of the preforming. Additionally, the optical assessment provided the fiber orientation that was mapped onto the injection mesh and included in the RTM simulation.

5.2.1 Preforming Experiments and Preform Inspection

Preforms comprising of four layers of the SAE 274 fabric, used for experimental permeability testing (cf. Chapter 3.3.1), together with 3 layers of an adhesive web (Spunfab PA 1541, $m_a = 6\,g/m^2$) as intermediate layers for fixation were created. Those were manufactured using a preforming tool in a hydraulic press following the thermal activation to a temperature in the stack center of $T = 125°$ with infrared light. The adhesive web consists of a polyamide with a melting temperature of approximately 200°. Therefore, one can assume that the adhesive web remains in the fabric stack as a solid during injection. Hence, it is considered as additional volume of the fiber domain for calculation of the V_f.

With the density of polyamide ($\rho = 1.14\,g/m^3$), the fiber volume fraction of the components can be calculated as $V_f = 43.79\,\%$ for those with thickness $t = 1.45mm$, and $V_f = 40.97\,\%$ for those with $t = 1.55mm$.

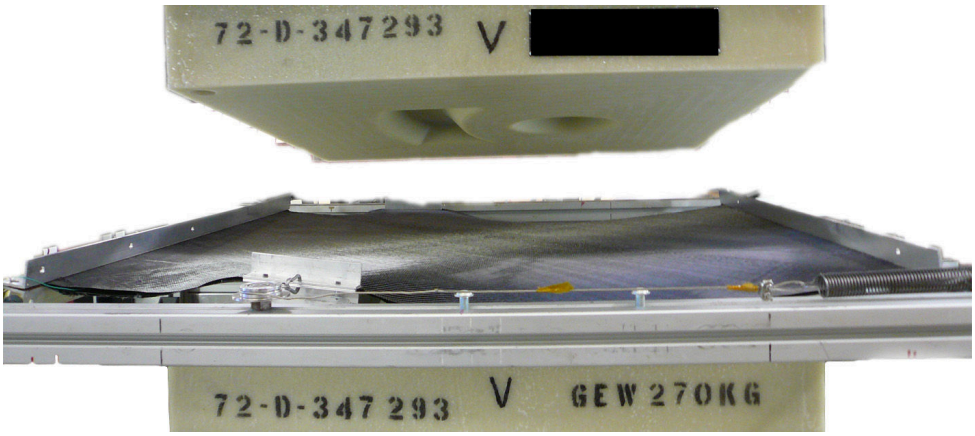

Figure. 5.4: Holding frame for the preform and preforming tool in a hydraulic press

Fiber Orientation Testing

In order to obtain accurate information about fabric shear deformation and repeatability of preforming itself, the preforms as well as the resin transfer molded component were investigated optically using the ProFactor sensor already introduced in Chapter 2.5. Hereby, it can be ensured that the actual fiber orientation is captured for further use in process simulation. In the context of a simultaneous engineering approach, it will be possible to determine fiber orientation by simulation means. For the presented application study, validated results from forming simulation were not available. Another big benefit of having optically inspected fiber orientation on an entire component is the opportunity to use those results for validation of forming simulation.

Experimental testing of fiber orientation was conducted in a two-stage approach. At first, the fiber orientations of the preforms were scanned at seven dedicated positions to obtain information about the repeatability of preforming. In a second step, the injected components were scanned completely to obtain a shear angle map that can be mapped on the RTM mesh.

Optical Inspection of Preforms

The preforms were scanned at seven dedicated positions to obtain a measure for the repeatability of preforming. This step was important as it provided information on how the variability of the preforms influences resin flow.

Figure 5.5 depicts one of the preforms and the scanning device. It also shows the scanned positions 1 to 7.

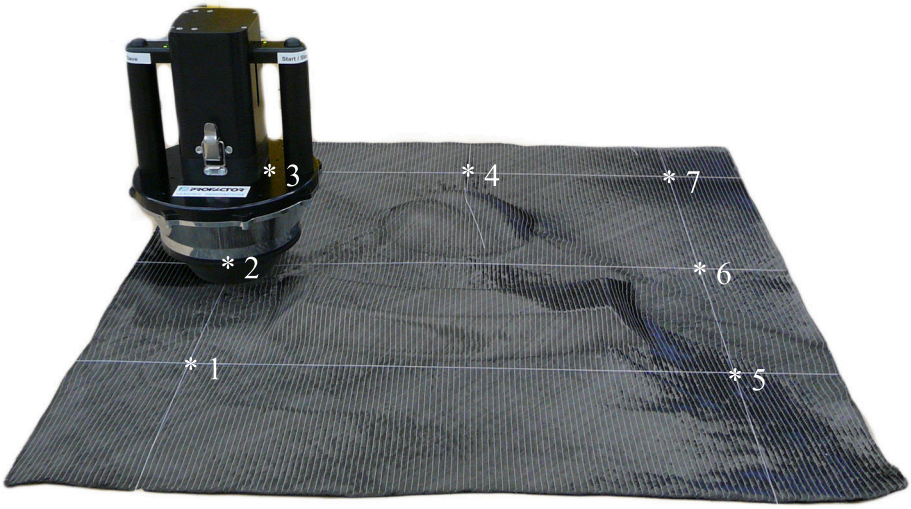

Figure. 5.5: Preform scanning using the ProFactor optical sensor

Five RTM components were manufactured in total. Each of them is comprised of four fabric layers. The optical inspection was performed on all of the five preforms. The images taken at the dedicated positions were segmented into a 10-by-10 grid resulting into a results matrix of 10-by-10 values. The maximal coefficient of variation is below 5% for most of the tiles. It must be stated that the sensor positioning on the preforms was done manually where a misalignment of $\pm 1°$ could be obtained. These errors contribute to the scanning results. Finally, it can be concluded that the preforming is highly reproducible.

Optical Inspection of Injected Component

A grid was drawn on the component as can be seen in Figure 5.6. Apart from the inclined areas of the ring segments (depicted in the left illustration of Figure 5.6) every part of the component, including the dome, was scanned and the image set was given a unique name containing coordinate information. In the latter, the Matlab script could load the image sets and extract the positions within the component coordinate system.

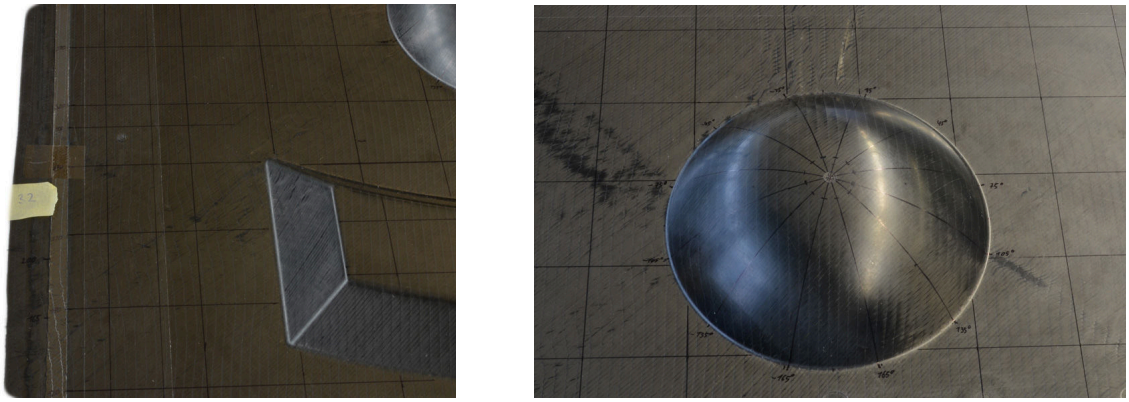

Figure. 5.6: Component with grid for scanning

The component was scanned with a grid of 12-by-12 images in the flat areas of the component, see Figure 5.7. At the non-flat areas, such as the dome and the trapezoidal exaltation, additional scans were made to capture the fiber orientation of these areas. In the context of simultaneous engineering it would be straightforward to attach the optical sensor to a robot and scan the entire components following pre-defined paths.

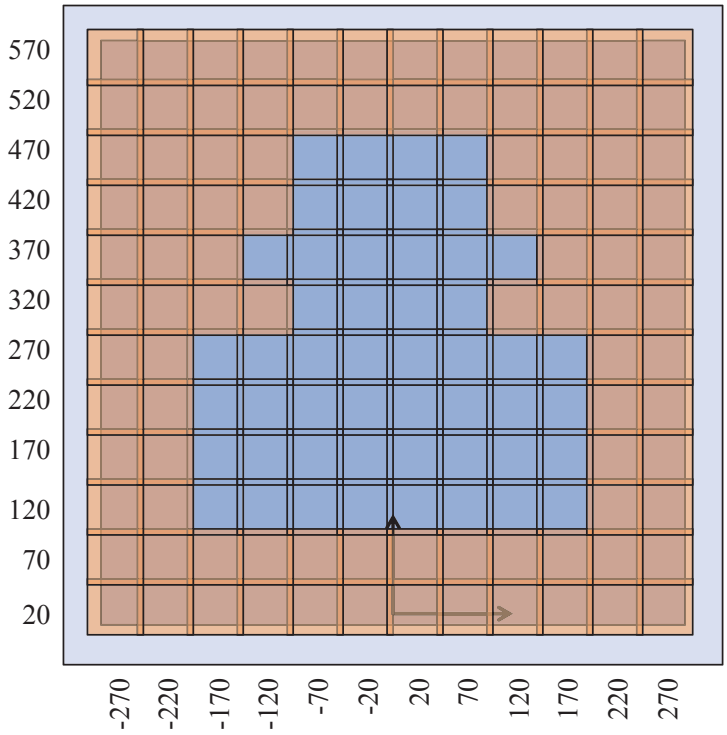

Figure. 5.7: 12-by-12 scanning grid of the flat areas of the RTM component

Result Transfer to RTM Simulation

The result transfer from scanned orientation information of the RTM component to the mapping onto the RTM mesh consists of several steps. The procedures has been coded using Matlab not only because the ProFactor sensor is able to export scan information directly to a Matlab compatible file format (*.mat) but also due to the image processing capabilities of Matlab. The individual steps are presented in the following:

Cropping: The ProFactor sensor has problems to correctly represent fiber orientations at the edges of the image. Primarily, the employed object lens distorts the images whose impact is more dominant the bigger the distance from the image center. Because scans have been taken with overlap, as can be seen in Figure 5.7, the defective areas are cropped.

Setting angles positive: Angles are set to a range from 0° to 179° using a simple `IF`-query

Filtering orientation data: Every cell (pixel) of a ProFactor results matrix (scan) carries an orientation information. A scan contains orientation information of both the fibers and the other items in the image such as stitches or gaps. To filter orientation information of solely the fiber domain, the maximum within a histogram plot of the orientation is

determined using `histc` and `max`. Then, all orientations that deviate from the maximum more than a certain threshold are deleted from the image. This approach is robust if the fibers represent the majority of pixels in an image. Alternatively, the working images of the ProFactor sensors depicting the reflecting and absorbing fraction of the original image can be employed to distinguish domains. This has been suspended here to maintain simplicity and and minimize CPU efforts. Figure 5.8 illustrates result images after filtering using various threshold values. The top-left image is unfiltered, whereas the others are filtered using threshold values of $\pm 10°$ (top-right), $\pm 20°$ (bottom-left) and $\pm 30°$ (bottom-right). The higher the threshold values, the more of the orientation values are kept at the original value as opposed to being set to `NaN` ('not a number', depicted as $0°$ in the plots). A threshold of $\pm 10°$ shows to be too low because it resets orientations that are actual fiber orientations. Using $\pm 30°$ is too coarse, because pixels not representing fiber are not properly filtered. So, $\pm 20°$ is taken as threshold to filter the images.

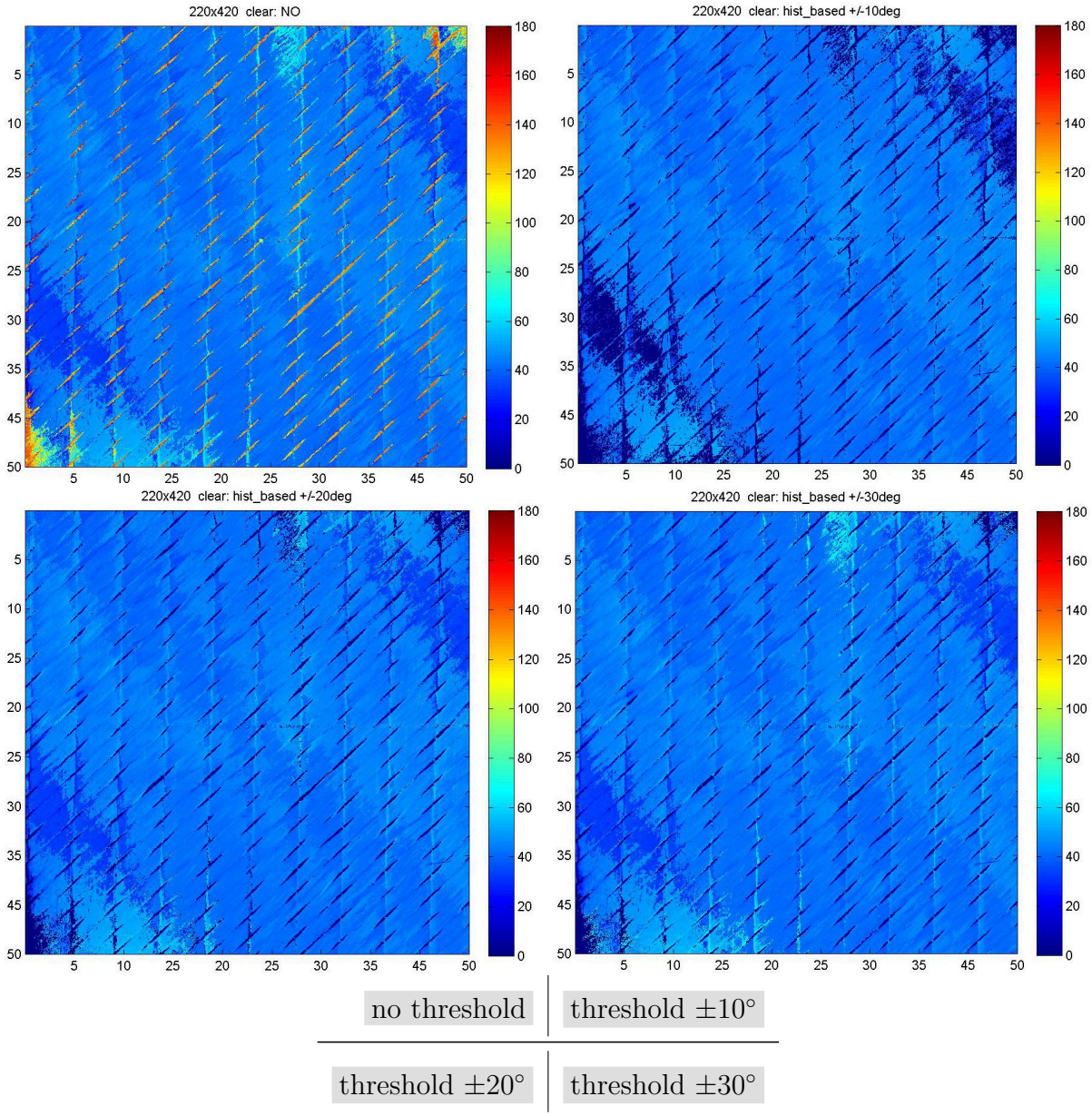

Figure. 5.8: Histogram based filtering using different threshold

Reducing matrix size: Orientation information is provided with a resolution of 28.6 px/mm which is too fine for mapping onto a component with dimensions of approximately 700 mm by 700 mm. The size of the matrices is reduced using `nanmean`. It is important however, to account for the fact that reduction factors can only be chosen so that the number of rows and columns of the resulting matrix are natural numbers.

The mapping tool implemented in PAM-RTM has an associated drawback. Starting from the center of gravity of an injection mesh element, the algorithm searches for an orientation mesh element along the normal vector of the injection mesh [131]. Thus, a maximum of one element can be found in the orientation mesh. Since there is no averaging procedure of

values from neighborhood elements in the target mesh, there is no benefit from providing a high-resolution orientation mesh.

For a given element size of the injection mesh the choice for the element number orientation mesh has to be made. In the following, a parameter study was conducted to find the correct adjustment of the reduction factors (RF) to obtain the best mapping results. Table 5.5 gives an overview about the data resolution along the processing chain and shows the optimal reduction factors for mapping.

Resolution $[px^2]$	**Step**
1600^2	
$\downarrow$	Cropping scan
1428^2	
$\downarrow$	Reducing resolution of scan with $RF_{scan} = 21$
68^2	
$\downarrow$	Assembling orientation matrix for mapping
898^2	
$\downarrow$	Reducing resolution of BM with $RF_{OM} = 13$
69^2	

Table. 5.5: Parameters study for reduction of matrix size

Assembling component orientation map: For setting up the orientation map of the entire map, a Matlab routine was employed that referenced a list containing all paths to the image sets from scanning and the respective positions. Based on these two information, the matrices from scanning were located in the component matrix.

Figure 5.9 shows the component orientation map. A fiber orientation of 45° is set at any place where no or insufficient data from scanning could be provided. Figure 5.10 shows how in-plane fiber waviness is represented by optical scanning. Fiber orientations still seem to be unrealistic at the edge of the tiles which arises from the distortion of the sensor lens. Cropping the scanned images however would cause gaps between the tiles containing no orientation information. The unrealistic values will be averaged by reduction of the orientation matrix prior to mapping.

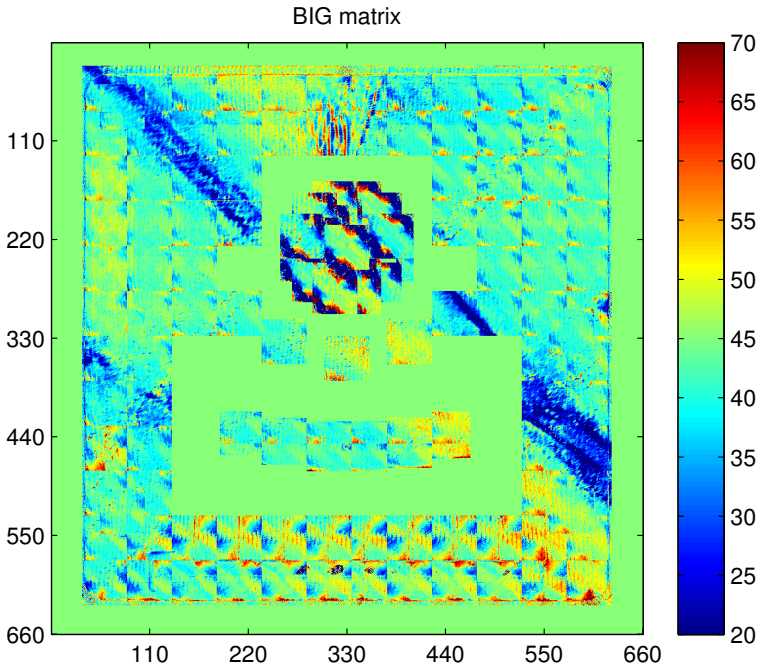

Figure. 5.9: Fiber orientation map of the RTM component

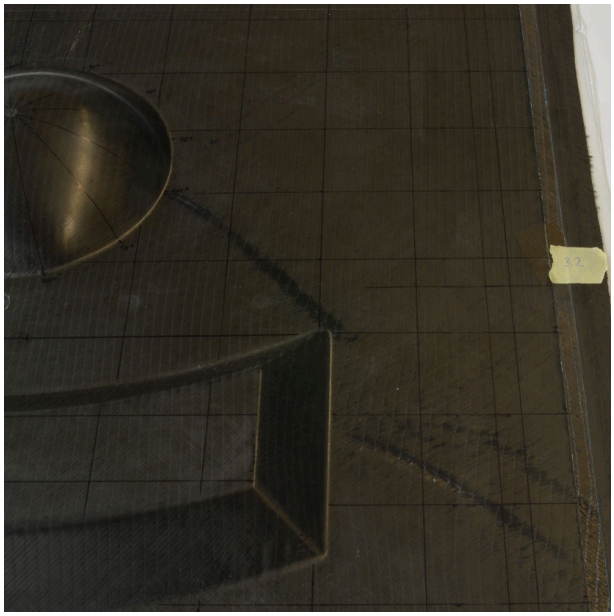

Figure. 5.10: Illustrating fiber in-plane waviness of the RTM component

Calculate shear angle: Figure 5.11 illustrates the definition and sign convention of shear deformation of a biaxial fabric as it is commonly applied, e.g. by Pickett [132]. The shear angle for this study is based on the assumption that the fiber orientation on the front-side, measured by the optical sensor, happens analogously on the rear side of the fabric, but in the opposite direction. Hence, the shear angle itself is calculated as

$$\delta = 2 \cdot (\theta_0 - \theta_m) \tag{5.1}$$

where θ_m is the measured fiber orientation and θ_0 the initial fiber orientation of the fabric (here: 45°) and the factor 2 originates from the fact that front and rear side are considered.

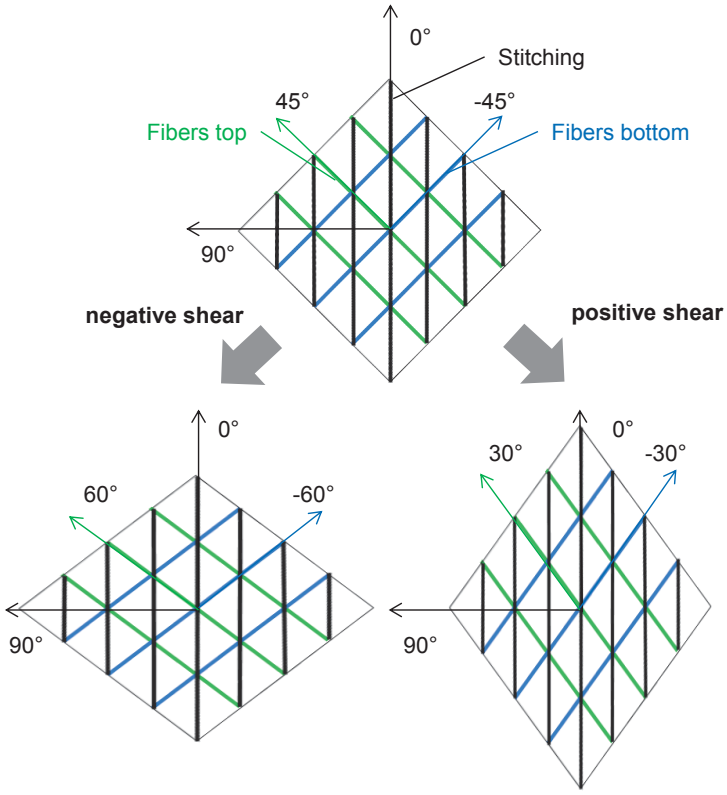

Figure. 5.11: Definition of shear

Calculating input data for drap3D.ps: The employed solver for RTM modeling, PAM-RTM, has an interface to the in-house forming simulation tool PAM-Quickform using a text file, as can be seen in Figure 5.12. This file resembles a FE-mesh file containing additional orientation information.

Starting from the matrix containing the shear angles, a mesh file has to be created. Here, two algorithms were used, which are presented in the following. Quadrilateral elements have been chosen for mapping because these require no additional conversion of the shear information available in a second order tensor. Listing 5.1 shows the code fragment to calculate the shell data. Based on a chosen discretization, the element identifier as well as the involved nodes and the orientation information are calculated

Listing 5.1: Script employed to obtain shell element data for mapping

```
%% Create shells

% BM_sr is the matrix containing the shear angles
  size_BM_sr = size(BM_sr);
  comp_dimension = 660;
  elem_size = comp_dimension/size_BM_sr;
  n_elem = size_BM_sr^2;
  shell = NaN(n_elem,8);

for n = 1:n_elem
% Current row in BM_sr resulting from n
    row = 1 + floor((n-1)/ size_BM_sr);
% Writing number of element n, and 4 nodes attached to elem n
    shell(n,1) = n; % element ID
    shell(n,2) = 1; %
    shell(n,3) = n+(row-1); % top left node
    shell(n,4) = n+(row-1)+1; % bottom left node
  shell(n,5) = n+size_BM_sr+row+1; % bottom right node
    shell(n,6) = n+size_BM_sr+row; % top right node
% Writing shear angle to Id_matrix
% Position of shear anlge in BM_sr based on n
    pos_BM_sr_row = ceil(n/size_BM_sr);
    a = n;
    while a > size_BM_sr
        a = a-size_BM_sr;
    end
    pos_BM_sr_col = a;
% Calculation of angles for drap3d.ps so that shear angle fits
    shell(n,7) = -BM_sr(pos_BM_sr_row,pos_BM_sr_col);
    shell(n,8) = BM_sr(pos_BM_sr_row,pos_BM_sr_col);
end
```

The code presented in Listing 5.2 calculates node data and saves it to the nodes variable based on the element data.

Listing 5.2: Script employed to obtain node data for mapping

```
%% Create nodes

nr_of_nodes = shell(n_elem,5);
nodes = NaN(nr_of_nodes,4);

for m = 1:nr_of_nodes
% Node ID
    nodes(m,1) = m;
% x-coordinate
    edge_hor = ceil(m/(size_BM_sr+1));
    nr_of_edges = size_BM_sr+1;
    nodes(m,2) = ((edge_hor-1)/(nr_of_edges-1))*comp_dimension;
% y-coordinate
    b = m;
    while b > nr_of_edges
        b = b-nr_of_edges;
    end
    edge_vert = b;
    nodes(m,3) = ((edge_vert-1)/(nr_of_edges-1))*comp_dimension;
% z-coordinate
    nodes(m,4) = 0;
end
```

After calculating all relevant node and shell data, this information is written to a mesh file as can be seen in Figure 5.12. Nodes are denoted as `NODE` followed by the ID and the coordinates. Quad elements are denoted as `MEMBR` including an ID, a zone ID, the used nodes and the fiber orientation on front and back side. For mapping orientation results from optical scanning, this format provided by ESI has been used and a the respective *.ps-files have been mimicked. It is crucial to have the information at the correct positions of the text line, e.g. fiber orientation can only read by the solver when they are at position 72 and 80.

```
$ Mapping of Fiber Orientation
$
$ To be used for IMPORT DRAPING RESULTS -> PAM-QUICKFORM
$ -> *.ps in PAM-RTM
$
$ Time:  18:10:46
$ Date:  04-Nov-2013
$
$ This file is generated by Matlab scripts that evaluate fiber
$ orientation data
$ Author:  Christoph Hahn, hahn@lcc.mw.tum.de
$
$---5---10----5---20----5---30----5---40----5---50----5---60----5---70----5---80
[...]
NODE  /     2601      353.913043       95.652174        0.000000
NODE  /     2062      353.913043      105.217391        0.000000
NODE  /     2063      353.913043      114.782609        0.000000
[...]
MEMBR /     2494       1    2530    2531    2601    2600             -43      43
MEMBR /     2495       1    2531    2532    2602    2601             -42      42
MEMBR /     2496       1    2532    2533    2603    2602             -42      42
[...]
ENDDATA
```

Figure. 5.12: *.ps file

5.2.2 RTM Experiments and Flow Front Detection:

RTM experiments were conducted and five components manufactured. An RTM press was used for clamping the tool halves together and to adjust the cavity thickness. The injection was performed with constant injection pressure using a pressure pot. Figure 5.13 shows the lower mold half with one of the components prior to demolding.

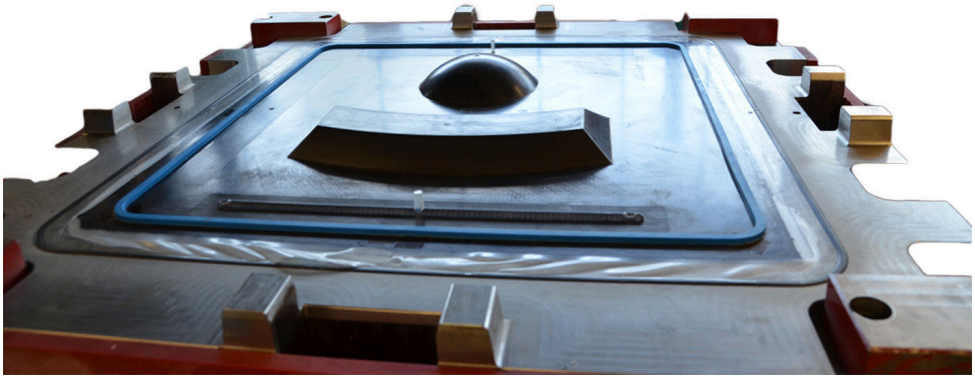

Figure. 5.13: Component before demolding

Determination of Viscosity

For the RTM injection a commonly used infusion resin system, RIM 135 with RIMH 136.6 hardener shipped by Momentive, was used. For that resin system viscosity development under certain thermal conditions has been tested which is presented in the next section.

An Anton Paar (MCR 302) rheometer was used with samples as depicted in Figure 5.14. The rotation plates have a diameter of $d = 25mm$. All test results depicted in the following were obtained by rotational testing with a rotational speed of $n = 7.64\frac{1}{min}$ which corresponds to a shear rate of $\dot{\epsilon} = 10\frac{1}{s}$. This shear rate was chosen to minimize the influence of shear rate on viscosity. It was also ensured that the measured torque was at least an order of magnitude higher than the machine precision.

Figure. 5.14: Specimen holder for viscosity measurement

Tests with different temperature and different pre-heating configurations were tested as shown in Figures 5.15 and 5.16. The time between sample preparation and the beginning of each test in the rheometer was kept constant to $t = 15min$. During this time the resin was degassed.

Figure 5.15 shows the results for test temperature $T_1 = 60°$ and $T_2 = 80°$. The three repeats for each configuration show that the test procedure itself is highly repeatable. The difference between the two processing temperatures is significant which is supported by the information given in the data sheet [133]. The graphs show that curing at a higher temperature results in a lower viscosity level during the first 200 seconds of the test, later in the test this effect is overcompensated by the faster curing reaction. From the tests conducted, it was not possible to deduce a correction scheme for viscosity evolution just by shifting the graphs in y-direction. This comes mainly from the fact that the viscosity drop in the early stage of the test has lower impact at a preheating temperature of $T_{PH} = 60°$ than at $T_{PH} = 50°$.

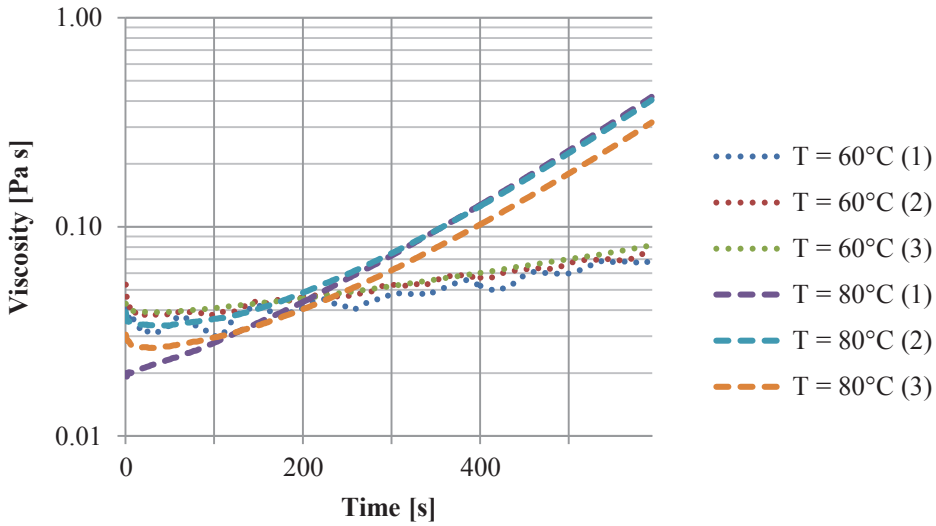

Figure. 5.15: Viscosity-time-curves at $T_1 = 60°$ and $T_2 = 80°$

The impact of preheating the samples was investigated, the preheating time was set to $t_{PH} = 10\ min$ for all configurations. Figure 5.16 indicates that the influence of pre-heating can be clearly measured. The impact on viscosity development is higher for preheating at $T = 60°$. Preheating at lower temperatures has a much lower impact.

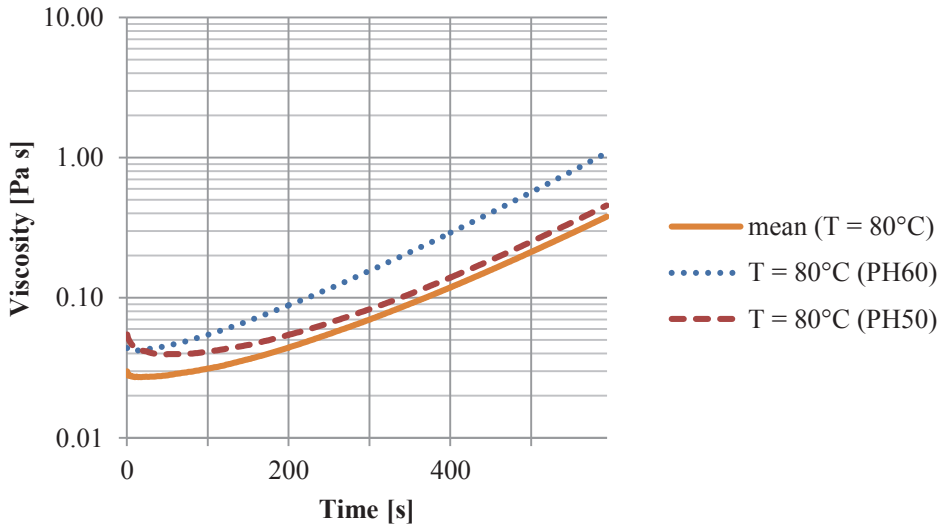

Figure. 5.16: Viscosity-time-curves at $T = 80°$ with different preheating configurations

Figure 5.16 shows the mean value of the graphs for $T = 80°$ and additional the mean value graphs for test with the same processing temperature and an additional preheating of the sample. The description *PH60* denotes a preheating in the rheometer for 10 minutes at $T = 60°$, respectively *PH50* at $T = 50°$.

Based on the test results for processing at $T = 80°$ without preheating, which ideally resemble the true RTM processing conditions, an exponential curve fit was carried out. The increase of viscosity while curing is a result of the chemical reaction between resin

and hardener. In the course of the reaction, the mobility of the already linked chains and the number of reactive groups decreases over-proportionally which can be described best by an exponential increase of viscosity over time. Using an exponential function to fit the viscosity-time relation is a straightforward approach, particularly valid for the chosen constant processing temperature. Because it is not desired to set-up a general material law for degree of cure and viscosity of epoxy resins, this approach is admissible here.

The parameters a and b for the exponential function

$$\eta(t) = a \cdot e^{b \cdot t} \tag{5.2}$$

were determined as $a = 3.2504 \cdot 10^{-2}$ and $b = 2.3638 \cdot 10^{-2}$ when fitting over a time span of $t_{exp} = [0s; 300s]$ which covers the time to fill of the components.

Flow Front Detection

Bobertag et al. [134] developed and put into service a capacitive sensor that is able to detect flow front arrival. The RTM tool for the experiments was equipped with 20 of these sensors, as can be seen in Figure 5.17. Similar to the pressure sensors employed to track the flow front for the experiments presented in Chapter 3, the capacitive sensors proved to work robustly. The signals over time showed two levels and a clearly visible step indicating the arrival of the flow front.

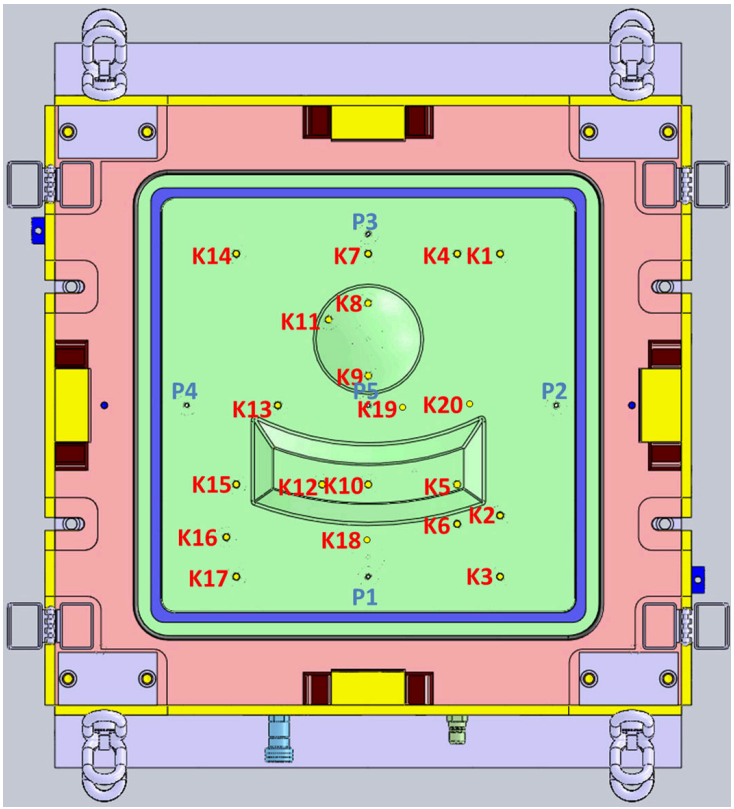

Figure. 5.17: Sensor positions in the validation tool

Three components were manufactured with the same boundary conditions that are depicted in Table 5.6. The thickness of the components was measured at six positions and the mean values are depicted.

	TTW 40	**TTW 41**	**TTW 43**
Resin	Hexion RIM 135 + RIMH 136.6		
$T_{Tool}[°]$	80		
$p_{Inj}[bar]$	3.0		
$T_{Resin}[°]$ before injection	25.5	23.0	25.0
t $[mm]$ of component	1.45	1.45	1.55

Table. 5.6: Experimental data RTM manufacturing

The results from evaluation of the flow front sensors are depicted in Table 5.7. The coefficient of variation (CoV) is plotted. For the sensors that are located in the second half of the flow distance, the variation coefficient is below 10%. This shows the good repeatability of the RTM process.

Sensor	**Time to sensor [s]**			**CoV [%]**
	TTW 40	TTW 41	TTW 43[5]	
K_1	172	161	167	2.7
K_3[6]	0	0	0	-[7]
K_4	156	146	133	6.4
K_5	11	13	17	17.3
K_6	3	4	6	–[3]
K_7	111	109	96	6.2
K_8	77	77	78	0.4
K_9	54	53	56	1.9
K_{10}	14	14	20	18.6
K_{11}	86	83	81	2.3
K_{12}	13	14	20	20.6
K_{13}	31	32	39	10.3
K_{14}	176	165	157	4.6
K_{15}	19	18	22	9.1
K_{16}	4	5	6	–
K_{17}	−1	0	2	–
K_{18}	1	3	4	–
K_{19}	35	36	43	8.8
K_{20}	30	33	41	13.0
			Mean	8.3

Table. 5.7: Flow front sensor data

Based on the information from Table 5.7 an approximate scheme of flow front progression were derived and is plotted in Figure 5.18. Sensors K3 and K17 as well as K13 and K20 have almost no time shift in their signal. In combination with the information given by K6, K10 and K19 a consistent conclusion can be derived. The flow front seems to be linear and parallel to the injection gate until it reaches the dome. The time shift between K19 and K13/K20 is very small 2s/4s, so one can conclude that the trapezoidal geometry does not induce any local flow front delays. The dome, especially in the area close to the center line in flow direction seems to cause race-tracking as sensor K8 is impregnated before K11. The race-tracking phenomenon can also nicely explain why K7 is impregnated long before K1 / K14. These two get impregnated at almost the same time which leads to the conclusion that the flow front is progressing symmetrically. The race-tracking most likely results from the manufacturing tolerances at the tooling. Optical inspection showed that the shear deformation at the dome is not higher compared to the area right of the trapezoidal exaltation, where the flow front is barely influenced.

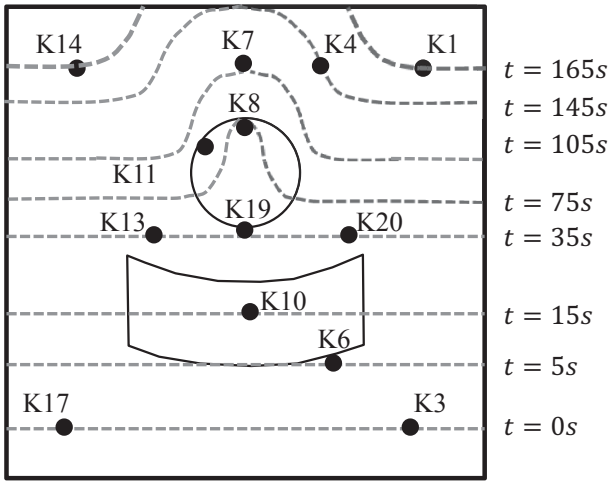

Figure. 5.18: Qualitative sketch of flow front distribution over time

The time to fill the entire component assuming that the dome does not create race-tracking can be estimated: Sensors K1 and K14 have a distance of $d_1 = 485mm$ to the injection port and the undisturbed flow arrives after $t_1 = 165s$. The remaining flow distance is $d_2 = 66mm$. Using equation,

$$t(x) = \frac{\mu \cdot (1 - V_f) \cdot x^2}{2 \cdot K \cdot p_{inj}} \tag{5.3}$$

[5]TTW 43 could not be compacted by the RTM press to the same extend and has a higher thickness as TTW 40 and TTW 41. Hence it has a lower V_f and shorter fill time. The value of K_1 was chosen as the mean value of TTW 40 and TTW 41. This gives a correction factor of 1.85 which was applied to all values.

[6]K_3 was used as reference to normalize the time to sensor.

[7]Variation coefficients for $t < 10s$ were not calculated.

derived from Darcy's law and continuity equation, the fill time can be calculated to $t_{fill} = 213s$. This is defined as the target fill time for the RTM simulations presented in the next section.

5.3 RTM Modeling

In the following section, permeability results obtained from both the simulation approach as well as experimental results are used for RTM modeling on the validation component. The influence of fabric shear using the information from orientation testing earlier in this chapter is considered. This leads to four different configurations that are evaluated.

5.3.1 Model Setup

The component was modeled using two-dimensional elements. The relation between thickness $t = 1.4mm$ and in-plane dimensions with a maximum flow distance of $d \approx 550mm$ together with the lay-up being comprised of the same material with the same orientation, where through-thickness flow is very unlikely to happen, legitimate the 2D simplification. The component model is comprised of 9560 triangular elements with an average element length of $10mm$, as can be seen in Figure 5.19. This resolution is fine enough to represent the geometry accurately while ensuring that CPU times for solving remain $< 1min$. The parallel solver (DMP) implemented in PAM-RTM was used. All simulations were conducted using two processors.

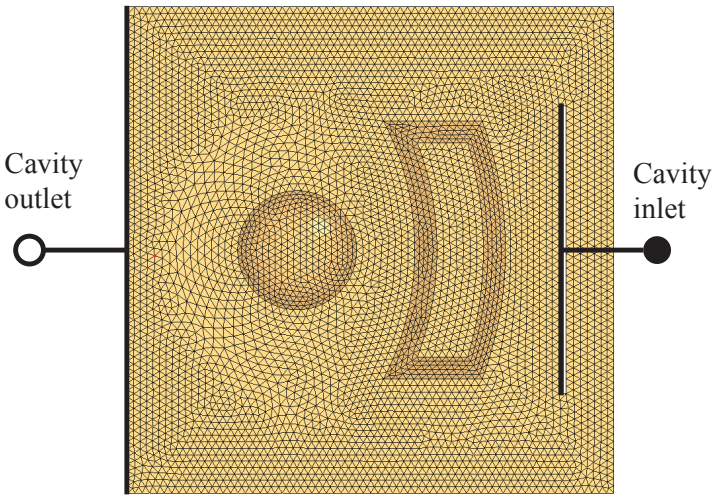

Figure. 5.19: RTM mesh of validation component

The viscosity-time relation from the tests conducted at $T = 80°$ were employed for the model. It is not possible to apply an exponential functions for the $\mu(t)$ relation in PAM-RTM as the experimental results would require. Hence, the relation was modeled using ten piecewise linear functions for the time span $[0s; 400s]$. The option *material age* was

used, which gives every amount of resin entering the mold the initial viscosity value at $t = 0s$ independent of the injection time. This represents the reality a lot better compared to applying the same viscosity law on the entire resin domain independent of position and time.

The permeability values presented in Table 5.8 are the transformed principal permeability values from experimental testing (SAE 274, 4 layers, steady-state testing) and those obtained by the simulation approach, where K_1 and K_2 are the principal permeability tensor entries and β is the rotation angle between K_{0° and K_1.

		experimental	simulated
K_1	$[10^{-11}\, m^2]$	5.07	6.02
K_2	$[10^{-11}\, m^2]$	3.08	1.30
β	$[^\circ]$	-17.8	$+9.0$

Table. 5.8: Principal Permeability values of SAE 274

The orientation of K_1 and K_2 with respect to the component coordinate system were modelled by specifying the element orientation of the RTM mesh depending on which material has been used.

The influence of fabric shear on permeability is considered for the simulations by correcting unsheared permeability element-wise with a V_f-dependent factor. Figure 5.20 shows a quadrangle with unsheared area A and shear deformation by angle δ. The sheared quadrangle's area can be expressed by

$$A_{sheared} = A \cdot cos(\delta) \tag{5.4}$$

Following the assumption that the fiber mass in the sheared area remains constant, the decrease of V_f follows the relation

$$V_{f,sheared} = \frac{V_f}{cos(\delta)}. \tag{5.5}$$

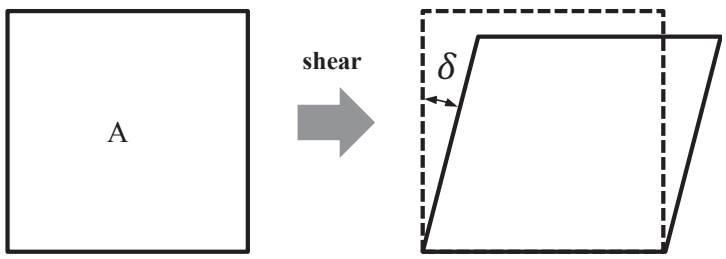

Figure. 5.20: Shear induced change of area

PAM-RTM provides two options to account for the influence of shear deformation on permeability. The sheared permeability information can be written to the material card

directly. This requires sheared permeability test results that are hard to determine and usually show a bigger scatter compared to unsheared test, mostly because it is demanding to apply shear deformation homogeneously to a sample, see Arnold [135].

Secondly, there is a model implemented based on the work conducted by C. Demaria [136, 137]. This approach was validated on woven fabrics and showed promising results with that class of materials. However, no investigations have been performed on NCFs which is the main reason why this approach was not considered for simulations in the next section.

Additionally, PAM-RTM allows to read in and export text files containing element information, such as shear angle, porosity, thickness and permeability, denoted as scalar field files. This approach has been followed for the RTM simulations presented in Section 5.3.2. The shear influence was accounted for by mapping the shear angles on the RTM mesh and a exporting a shear angle scalar field file. Then permeability of every element was corrected using Equation 5.5 and was written to a permeability scalar field file which was considered by the RTM solver.

5.3.2 Simulation Results

Table 5.9 lists the four model configurations that were modeled. Firstly, the differences arising from the two types of permeability results - experimental and simulated - are compared. Secondly, the influence of shear deformation on the filling will be investigated.

Model	Specification
1	$K_{experimental}$
2	$K_{experimental}$, including shear
3	$K_{simulated}$
4	$K_{simulated}$, including shear

Table. 5.9: Overview of models for RTM simulation

Fill Time Results

The simulations have been conducted and the fill time has been evaluated at the same positions as for the RTM experiments from Section 5.2.2, see the black marks in Figure 5.21. Table 5.10 summarizes the fill times from simulation compared to the RTM experiments. The simulations based on experimental permeability values (model 1 and 2) overestimate the fill time. Consideration of shear always results in an increased fill time since including shear comes along with local decrease of permeability due to increased V_f. The fill times of the models (3 and 4) that are relying on simulated permeability show good correlation, especially the model including fabric shear which can be seen as the more realistic case.

Model	$\mathbf{t_{Fill}}$ $[s]$	$\mathbf{\Delta}[\%]$
Exp.	213	-
1	232	+8.9
2	268	+25.8
3	134	−37.8
4	218	+1.4

Table. 5.10: Time to reach flow end of cavity

Figure 5.21 gives an overview of the calculated flow front propagation. The permeability values depicted in Table 5.8 show a clear preferred direction, for both materials.

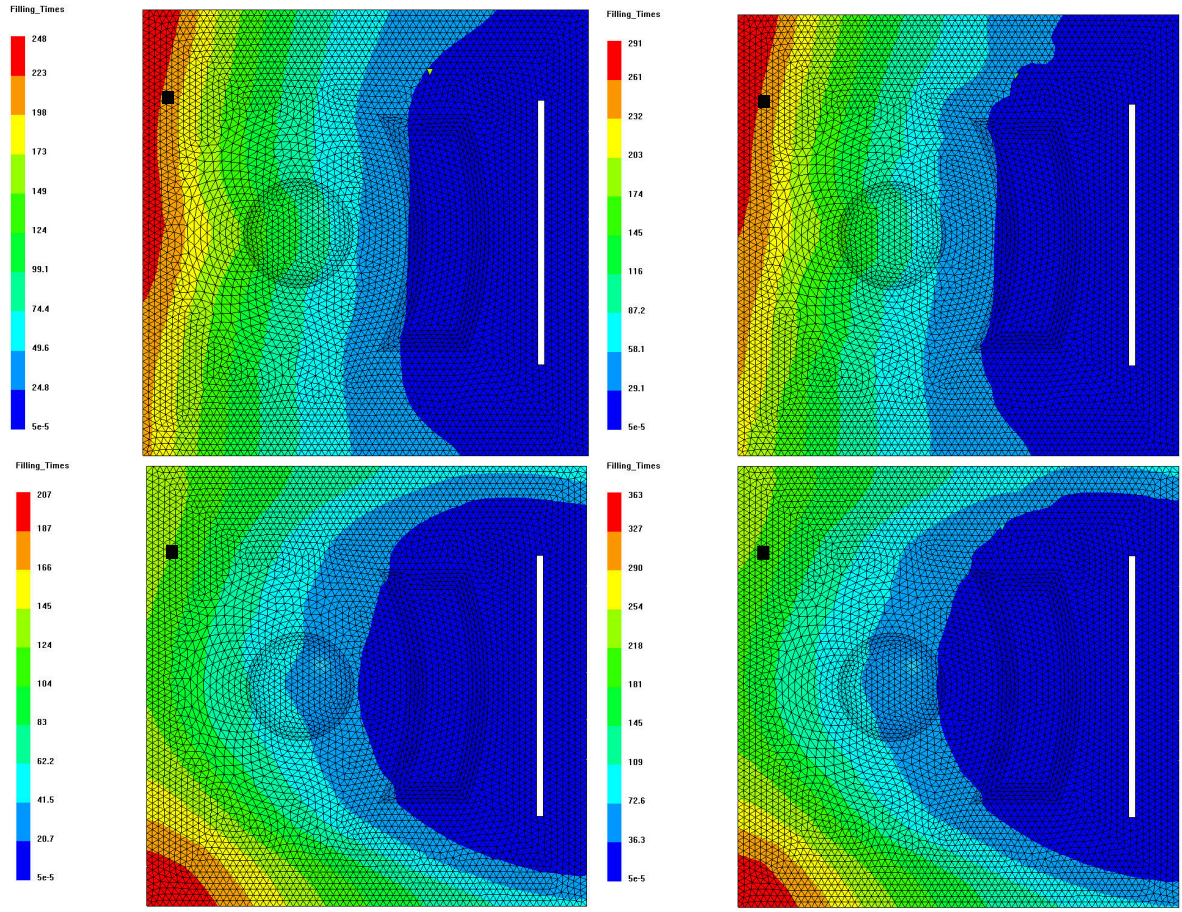

Model 1 | Model 2

Model 3 | Model 4

Figure. 5.21: Fill time contour plots

Flow Front Results

The 1-direction is approximately oriented from injection port to the vent and the ratio K_1/K_2 is 1.7 for the experimentally determined permeability and 4.6 for the simulated one. This causes a flow front advancement that is oriented more in the vent direction than sideways. The impact of shear is clearly visible for both model types and causes a slower flow front progression in the shear prone areas resulting in an increased fill time. The smaller K_1/K_2-ratio of $K_{experimental}$ results in a rather linear flow front shape which represents the real flow front shape better than the models based on $K_{simulated}$. The large K_1/K_2-ratio for the simulated permeability causes a curved flow front shape that drags behind at the cavity edges.

Conclusion

In conclusion, it is evident that simulated permeability results are suitable to predict fill times and to a lesser extend the flow front shape for the tested material.

For a component manufacturer, a prediction for the fill time is the more important information. Based on this measure, the pressure required to fill the component in the desired time is known. This is very important for all decisions with respect to hardware such as injection pump, tooling and press. A precise prediction of the flow front shape is also of big interest for manufacturers, especially when decisions about position and number of outlets have to be made. However, manufacturing tolerances, that always can occur, have huge impact on the flow front shape as was observed for the dome area of the component. A conservative approach for designing the outlet system is recommended.

It also has to be stated that the main focus of the presented approach was put on a fast prediction of permeability. It provides a tool to predict manufacturability in the design phase of a component. When a final design of a component is freezed and it is required to provide a 100% process simulation further investigations, especially for the permeability characterization at complex geometries, are recommended.

6 Conclusion and Outlook

6.1 Experimental Permeability Testing

/ Chapter 3 /

A test bench for experimental permeability evaluation was developed. The 1D test method was employed: using this method, transient and steady state testing is possible with the same setup on a single sample.

The setup can account for both flow scenarios without visual flow front inspection. The flow front inspection was conducted using pressure sensors. In this context a new approach was developed and tested to detect the flow front using the pressure-time-signal. The results of this approach are robust and represent the flow front progression reasonably well.

Participation in the second international benchmark exercise has demonstrated the robustness of the test method. There was good correlation to the other participants and hence the results obtained with the setup can be considered as highly credible.

A test campaign was conducted using two NCFs with the same fabric structure but different areal weight. Results indicate that areal weight has a dominant influence on fabric permeability. The relation of permeability as function of V_f can be nicely described by existing schemes such as Kozeny-Carman. The number of layers has a minor impact on permeability in the tested thickness range of 1.0 mm to 4.8 mm. Steady-state permeability results generally showed a higher permeability compared to transient test results which can be explained by cavity deformation. The orientation of the principal permeability tensor generally is aligned in the direction of the fibers on the rear-side of the fabrics. Image processing could explain this coincidence by evaluating the size of the gaps in the fabric induced by stitching.

Furthermore a new scheme for calculation of the principal permeability tensor was introduced based on a least-square fitting approach. It showed very good correlation to existing analytical schemes. A drawback was identified for the case of different number of tests in particular orientations.

6.2 Simulation Approach

/ Chapter 4 /

As a method of fast and robust permeability prediction, a simulation approach based on processing of fabric images is proposed. The fabric images, which can be considered as raw

data are acquired using a transparent compaction mold with a professional office scanner. For the software implementation Matlab was chosen because of its universality and its large library of functions in the field of image processing. In the Matlab framework third-party tools such as the fabric modeling tool WiseTex and the unit cell CFD solver FlowTex, both were implemented using XML interfaces and command line scripting. Development of these interfaces on the side of the external tools has been a joint development with S.V. Lomov at KU Leuven. The image processing itself has been entirely coded in Matlab and merged into a GUI-based tool called *FASTER*. It comprehends all functionality in the context of image segmentation which are:

- Gray level thresholding,
- morphological filtering.

Images processing itself comprises the implementations of:

- Canny edge detection,
- Fourier analysis,
- curve fitting,
- watershed transformation.

A parameter study on the capabilities of image processing was conducted with six fabrics. Segmenting domains such as fibers, stitching and gaps was possible for all fabrics. Deriving image properties such as counting items, calculating size and orientations depends very much on the regularity of the fabrics – the more the regular the more robust the result.

In conclusion, the main goal of speeding-up permeability characterization and having a robust test method at the same time was achieved. All information required for fabric modeling were either known a priori or could be determined using the simulation approach.

6.3 Application

/ Chapter 5 /

To ensure quality of the results an application study was performed on a component-like validation geometry. Beforehand, a sensitivity study as well as a mesh refinement study was conducted using the unit cell CFD solver FlowTex. Neglecting stitching in the model has a significant influence on the permeability results and alters the entire model structure. Omitting intra-yarn flow (IYF) also has a significant impact, but comparisons with experimental tests have shown that it cannot be neglected despite the higher computational cost. Changes to gap properties are important, which is straightforward: altering the dimensions of the main flow geometry will affect permeability. Changes to properties of the fiber bundle have a low influence on permeability. The mesh refinement study has shown that permeability is influenced by the discretization: for a voxel number $> 10^6$

it can be neglected. Models with intra-yarn flow can be solved up to a voxel number of $6 \cdot 10^5$ elements. For NCFs, this number can also be considered as value that should not be undercut. A restriction of WiseTex that just two orientations can be tested that are perpendicular to each other, was resolved by expanding the voxel model, rotating it and then cropping the model again at the desired size by applying a script that has been developed.

Simulated permeability results correlate well to the experimentally-determined values. The SAE 540 can be better represented than the SAE 274 due to the fact that the gaps are smaller for the SAE 274 and correct representation of the gaps is highly dependent on the discretization.

Optical preform inspection revealed very good repeatability of the preforming itself. The impact of preform variability on scatter in RTM processing was neglected. Full-component orientation scanning using the same optical device allowed the actual fiber orientation to be extracted without having to rely on forming simulation results. Additionally, the obtained information could be used for validating forming simulation. For the latter, scripts have been developed to derive the shear deformation and map it onto a RTM mesh. Resin viscosity of the system RIM 135 with hardener RIMH 136.6 was fully characterized at different processing temperatures and also the influence of preheating was evaluated. To compare RTM simulation results with actual flow front advancement, a tool equipped with capacitive sensors for flow front tracking has been applied. The RTM experiments proved to be very repeatable and the flow front detection performed robustly under all testing conditions.

For RTM modeling the impact of shear deformation on permeability has been modeled by taking the local change of fiber volume fraction into account. The calculations were performed outside the RTM tool and imported using local element files. Results from RTM simulation showed a very good correlation of fill time from models based on simulated permeability when taking shear into account. Also the flow front shape could be predicted reasonably well.

For the tested materials, permeability can be predicted by simulation means with similar quality as experimentally and the time for material characterization is reduced to the desired extend. The simulation approach for permeability overestimates the ratio between K_1 and K_2 which results in an incorrect prediction of the flow front shape. Furthermore, the simulation approach is not able to forecast the difference in permeability that two similar fabrics with different areal weight showed. For practical application it is recommended to verify the results of the simulation approach with experiments when additional complexity is added to the geometry or the type of fabric is changed.

6.4 Outlook

The goals formulated in Chapter 1 were fully achieved. Nevertheless during a research project usually questions arise that cannot be answered right away.

First of all, the results obtained with the simulation approach cannot be considered as universal. It is part of future research to investigate the applicability to geometries with more complexity or different lay-ups. Furthermore the use of fabrics with different architecture must be validated.

A limiting factor for the simulation approach lies in the model size restrictions of FlowTex. Either one could invest time to further develop FlowTex and add parallelization capabilities or one could follow a more general approach of model conversion to independent formats that are compatible to a larger number of CFD solvers. A paper by Swery et al. [130] presents results of current research on that topic.

As RTM manufacturing often comes along with fluctuating material properties and processing conditions, another very interesting approach is to address variability using the available characterization tools resulting from this work. Fabric, as well as preform, scatter could be evaluated using optical techniques and the influence on the following steps could be investigated. Focus on variability with a global perspective allows distinguishing between errors from simulation or testing and errors arising from variability.

A Appendix

A.1 Thin Shell Approximation

Assumed we have a composite lay-up with thickness t and length l in x-direction. The permeabilities are denoted as K_x and K_z in the direction of the coordinates x and, as it is depicted in Figure A.1.

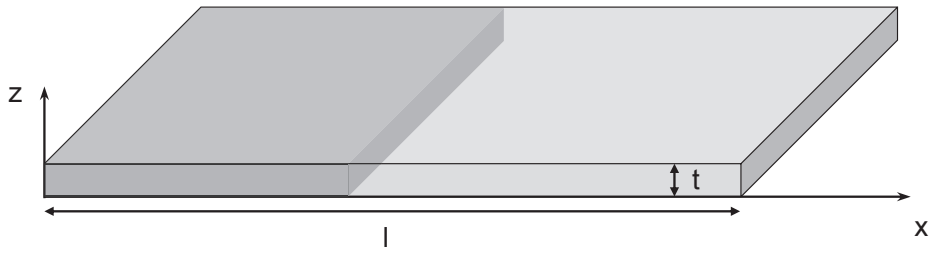

Figure. A.1: Thin shell approximation

Isotropic Preform

For an isotropic preform we have $K_x = K_z$. The continuity equation can be written as:

$$\frac{\partial v_x}{\partial x} + \frac{\partial v_z}{\partial z} = 0 \Rightarrow \left|\frac{\partial v_x}{\partial x}\right| \approx \left|\frac{\partial v_z}{\partial z}\right| \Rightarrow v_z \approx v_x \cdot \frac{t}{l}$$

2D modeling (accounting just for in-plane flow) is admissible, when

$$\frac{l}{t} \gg 1 \tag{A.1}$$

Anisotropic Preform

For an anisotropic preform we have $K_x \neq K_z$. Comparing $\frac{\partial p_x}{\partial x}$ and $\frac{\partial p_y}{\partial y}$ leads to,

$$\frac{\Delta p_x \cdot t}{\Delta p_z \cdot l}$$

which gives after plugging in Darcy's law

$$\frac{l \cdot K_z}{t \cdot K_x}$$

The pressure gradient in z-direction and hence out-of-plane flow can be neglected if,

$$\frac{l \cdot K_z}{t \cdot K_x} \gg 1 \tag{A.2}$$

A.2 Permeability Results

4-cavity 1D test setup
SAE 274 transient tests

274_51p6_4lay_transient
274_51p6_4lay_unsat.xls

	FVF [-]	K [m²]		K [m²]		K [m²]
0°_v1	0.503	1.60E-11	45°_v1	1.04E-11	90°_v1	7.95E-12
0°_v2	0.501	1.40E-11	45°_v2	9.82E-12	90°_v2	9.24E-12
0°_v3	0.496	1.73E-11	45°_v3	8.89E-12	90°_v3	9.73E-12
0°_v4	0.504	1.31E-11	45°_v4	9.73E-12	90°_v4	8.81E-12
0°_v5	0.505	1.50E-11	45°_v5	1.11E-11	90°_v5	1.03E-11
Mean	0.502	1.51E-11		9.98E-12		9.22E-12
StdDev	0.004	1.66E-12		8.13E-13		9.07E-13
VarCoeff [%]	0.71	11.01		8.14		9.84

	K1	K2	angle
curve fit	1.613E-11	8.980E-12	164.14
analyt.	1.594E-11	8.923E-12	164.41

274_56p3_4lay_transient
274_56p3_4lay_unsat.xls

	FVF [-]	K [m²]
0°_v1	0.544	7.096E-12
0°_v2	0.546	7.700E-12
0°_v3	0.526	1.043E-11
0°_v4	0.535	6.681E-12
0°_v5	0.535	8.023E-12
Mean	0.537	7.38E-12
StdDev	0.008	6.02E-13
VarCoeff [%]	1.50	8.16

274_51p6_8lay_transient
274_51p6_8lay_unsat.xls

	FVF [-]	K [m²]		K [m²]		K [m²]
0°_v1	0.509	1.535E-11	45°_v1	9.996E-12	90°_v1	8.911E-12
0°_v2	0.493	1.744E-11	45°_v2	9.283E-12	90°_v2	9.990E-12
0°_v3	0.495	1.432E-11	45°_v3	1.012E-11	90°_v3	1.538E-11
0°_v4	0.504	1.529E-11	45°_v4	1.213E-11	90°_v4	1.190E-11
0°_v5	0.495	1.614E-11	45°_v5	1.089E-11	90°_v5	1.150E-11
Mean	0.499	1.57E-11		1.05E-11		1.15E-11
StdDev	0.007	1.16E-12		1.08E-12		2.46E-12
VarCoeff [%]	1.39	7.41		10.34		21.31

	K1	K2	angle
curve fit	1.994E-11	1.032E-11	147.84
analyt.	1.926E-11	1.016E-11	149.82

274_56p3_8lay_transient
274_56p3_8lay_unsat.xls

	FVF [-]	K [m²]
0°_v1	0.547	6.989E-12
0°_v2	0.546	7.223E-12
0°_v3	0.535	8.936E-12
0°_v4	0.526	7.491E-12
0°_v5	0.532	7.272E-12
Mean	0.537	7.58E-12
StdDev	0.009	7.77E-13
VarCoeff [%]	1.69	10.25

274_51p6_16lay_transient
274_51p6_16lay_unsat.xls

	FVF [-]	K [m²]		K [m²]		K [m²]
0°_v1	0.506	1.562E-11	45°_v1	1.388E-11	90°_v1	1.102E-11
0°_v2	0.502	1.674E-11	45°_v2	1.278E-11	90°_v2	9.902E-12
0°_v3	0.504	1.601E-11	45°_v3	1.306E-11	90°_v3	1.271E-11
0°_v4	0.509	1.619E-11	45°_v4	1.257E-11	90°_v4	1.212E-11
0°_v5	0.495	1.699E-11	45°_v5	1.240E-11	90°_v5	1.783E-11
Mean	0.503	1.63E-11		1.29E-11		1.14E-11
StdDev	0.005	5.55E-13		5.82E-13		1.24E-12
VarCoeff [%]	1.05	3.40		4.50		10.85

	K1	K2	angle
curve fit	1.758E-11	1.257E-11	1.54E+02
analyt.	1.6396E-11	1.13954E-11	173.67

274_56p3_16lay_transient
274_56p3_16lay_unsat.xls

	FVF [-]	K [m²]
0°_v1	0.541	8.806E-12
0°_v2	0.547	6.714E-12
0°_v3	0.533	9.075E-12
0°_v4	0.527	8.330E-12
0°_v5	0.530	7.619E-12
Mean	0.536	8.11E-12
StdDev	0.008	9.56E-13
VarCoeff [%]	1.54	11.79

SAE 540 transient tests

540_50p8_2lay_transient
540_50p8_2lay_unsat.xls

	FVF [-]	K [m²]		K [m²]		K [m²]
0°_v1	0.507	3.215E-11	45°_v1	3.475E-11	90°_v1	2.743E-11
0°_v2	0.501	3.167E-11	45°_v2	2.328E-11	90°_v2	3.350E-11
0°_v3	0.509	3.472E-11	45°_v3	2.532E-11	90°_v3	3.518E-11
0°_v4	0.505	2.823E-11	45°_v4	3.017E-11	90°_v4	2.078E-11
0°_v5	0.503	3.015E-11	45°_v5	2.662E-11	90°_v5	2.346E-11
Mean	0.505	3.14E-11		2.51E-11		2.39E-11
StdDev	0.003	2.41E-12		1.68E-12		3.35E-12
VarCoeff [%]	0.63	7.69		6.71		14.01

	K1	K2	angle
curve fit	3.262E-11	2.830E-11	151.60
analyt.	3.224E-11	2.342E-11	164.41

540_55p5_2lay_transient
540_55p5_2lay_unsat.xls

	FVF [-]	K [m²]
0°_v1	0.554	1.208E-11
0°_v2	0.551	1.435E-11
0°_v3	0.550	1.080E-11
0°_v4	0.555	1.102E-11
0°_v5	0.546	1.261E-11
Mean	0.551	1.16E-11
StdDev	0.004	8.61E-13
VarCoeff [%]	0.65	7.41

540_50p8_4lay_transient
540_50p8_4lay_unsat.xls

	FVF [-]	K [m²]		K [m²]		K [m²]
0°_v1	0.507	3.828E-11	45°_v1	3.298E-11	90°_v1	2.534E-11
0°_v2	0.508	4.199E-11	45°_v2	2.883E-11	90°_v2	2.503E-11
0°_v3	0.504	3.748E-11	45°_v3	3.050E-11	90°_v3	2.902E-11
0°_v4	0.507	2.996E-11	45°_v4	3.262E-11	90°_v4	2.607E-11
0°_v5	0.499	3.440E-11	45°_v5	3.517E-11	90°_v5	2.300E-11
Mean	0.505	3.64E-11		3.20E-11		2.57E-11
StdDev	0.004	4.51E-12		2.43E-12		2.18E-12
VarCoeff [%]	0.73	12.38		7.59		8.49

	K1	K2	angle
curve fit	3.726E-11	2.565E-11	8.75
analyt.	3.686E-11	2.548E-11	189.44

540_55p5_4lay_transient
540_55p5_4lay_unsat.xls

	FVF [-]	K [m²]
0°_v1	0.554	1.244E-11
0°_v2	0.554	1.338E-11
0°_v3	0.551	1.477E-11
0°_v4	0.549	1.229E-11
0°_v5	0.545	1.250E-11
Mean	0.551	1.31E-11
StdDev	0.004	1.04E-12
VarCoeff [%]	0.69	7.94

540_50p8_8lay_transient
540_50p8_8lay_unsat.xls

	FVF [-]	K [m²]		K [m²]		K [m²]
0°_v1	0.507	4.035E-11	45°_v1	3.167E-11	90°_v1	2.517E-11
0°_v2	0.505	4.088E-11	45°_v2	2.927E-11	90°_v2	2.229E-11
0°_v3	0.505	4.193E-11	45°_v3	3.709E-11	90°_v3	2.922E-11
0°_v4	0.506	4.167E-11	45°_v4	3.161E-11	90°_v4	3.125E-11
0°_v5	0.502	4.648E-11	45°_v5	3.490E-11	90°_v5	2.869E-11
Mean	0.505	4.23E-11		3.29E-11		2.73E-11
StdDev	0.002	2.44E-12		3.08E-12		3.56E-12
VarCoeff [%]	0.37	5.77		9.35		13.05

	K1	K2	angle
curve fit	5.122E-11	3.329E-11	1.73E+02
analyt.	4.227E-11	2.732E-11	178.86

540_55p5_8lay_transient
540_55p5_8lay_unsat.xls

	FVF [-]	K [m²]
0°_v1	0.549	1.880E-11
0°_v2	0.555	1.491E-11
0°_v3	0.547	1.640E-11
0°_v4	0.546	1.488E-11
0°_v5	0.545	1.464E-11
Mean	0.548	1.592E-11
StdDev	0.004	1.75E-12
VarCoeff [%]	0.72	10.99

SAE 274 stationary tests

274_51p6_4lay_stationary
274_51p6_4lay_sat.xls

	K [m²]		K [m²]		K [m²]
0°_v1	2.673E-11	45°_v1	1.398E-11	90°_v1	1.333E-11
0°_v2	1.763E-11	45°_v2	1.923E-11	90°_v2	1.170E-11
0°_v3	1.977E-11	45°_v3	9.816E-12	90°_v3	1.529E-11
0°_v4	1.991E-11	45°_v4	1.490E-11	90°_v4	1.451E-11
0°_v5	2.196E-11	45°_v5	1.682E-11	90°_v5	1.635E-11
Mean	2.12E-11		1.49E-11		1.42E-11
StdDev	3.45E-12		3.50E-12		1.80E-12
VarCoeff [%]	16.28		23.44		12.63

	K1	K2	angle
curve fit	2.243E-11	1.409E-11	165.70
analyt.	2.245E-11	1.372E-11	162.30

274_56p3_4lay_stationary.xls
274_56p3_4lay_sat.xls

	K [m²]
0°_v1	1.63116E-11
0°_v2	1.23935E-11
0°_v3	7.07507E-11
0°_v4	1.14156E-11
0°_v5	1.41957E-11
Mean	1.36E-11
StdDev	2.16E-12
VarCoeff [%]	15.87

274_51p6_8lay_stationary.xls
274_51p6_8lay_sat.xls

	K [m²]		K [m²]		K [m²]
0°_v1	2.168E-11	45°_v1	1.428E-11	90°_v1	1.335E-11
0°_v2	2.296E-11	45°_v2	1.329E-11	90°_v2	1.435E-11
0°_v3	1.744E-11	45°_v3	1.407E-11	90°_v3	1.866E-11
0°_v4	2.159E-11	45°_v4	1.404E-11	90°_v4	1.671E-11
0°_v5	2.321E-11	45°_v5	1.435E-11	90°_v5	1.539E-11
Mean	2.14E-11		1.40E-11		1.57E-11
StdDev	2.32E-12		4.20E-13		2.07E-12
VarCoeff [%]	10.86		3.00		13.22

	K1	K2	angle
curve fit	2.784E-11	1.365E-11	148.12
analyt.	2.701E-11	1.361E-11	148.85

274_56p3_8lay_stationary.xls
274_56p3_8lay_sat.xls

	K [m²]
0°_v1	1.12353E-11
0°_v2	1.71182E-11
0°_v3	3.31177E-11
0°_v4	1.37405E-11
0°_v5	1.22004E-11
Mean	1.36E-11
StdDev	2.58E-12
VarCoeff [%]	19.00

274_51p6_16lay_stationary.xls
274_51p6_16lay_sat.xls

	K [m²]		K [m²]		K [m²]
0°_v1	2.019E-11	45°_v1	1.751E-11	90°_v1	1.438E-11
0°_v2	2.067E-11	45°_v2	1.474E-11	90°_v2	1.513E-11
0°_v3	2.463E-11	45°_v3	2.061E-11	90°_v3	1.623E-11
0°_v4	2.476E-11	45°_v4	1.433E-11	90°_v4	1.749E-11
0°_v5	2.146E-11	45°_v5	1.807E-11	90°_v5	1.803E-11
Mean	2.23E-11		1.71E-11		1.62E-11
StdDev	2.20E-12		2.58E-12		1.54E-12
VarCoeff [%]	9.83		15.14		9.46

	K1	K2	angle
curve fit	2.319E-11	1.603E-11	164.98
analyt.	2.319E-11	1.583E-11	163.40

274_56p3_16lay_stationary.xls
274_56p3_16lay_sat.xls

	K [m²]
0°_v1	1.59682E-11
0°_v2	8.95359E-12
0°_v3	1.63490E-11
0°_v4	1.19872E-11
0°_v5	1.08628E-11
Mean	1.20E-11
StdDev	3.13E-12
VarCoeff [%]	26.04

SAE 540 stationary tests

540_50p8_2lay_stationary
540_50p8_2lay_sat.xls

	K [m²]		K [m²]		K [m²]
0°_v1	3.515E-11	45°_v1	3.074E-11	90°_v1	3.506E-11
0°_v2	4.169E-11	45°_v2	3.466E-11	90°_v2	4.869E-11
0°_v3	4.540E-11	45°_v3	2.744E-11	90°_v3	7.110E-11
0°_v4	3.427E-11	45°_v4	3.066E-11	90°_v4	3.839E-11
0°_v5	3.702E-11	45°_v5	3.396E-11	90°_v5	2.720E-11
Mean	3.87E-11		3.15E-11		3.36E-11
StdDev	4.71E-12		2.90E-12		5.75E-12
VarCoeff [%]	12.18		9.22		17.12

	K1	K2	angle
curve fit	7.210E-11	3.132E-11	143.46
analyt.	4.271E-11	3.103E-11	148.39

540_55p5_2lay_stationary
540_55p5_2lay_sat.xls

	K [m²]
0°_v1	2.133E-11
0°_v2	6.945E-11
0°_v3	1.871E-11
0°_v4	1.740E-11
0°_v5	1.723E-11
Mean	1.87E-11
StdDev	1.89E-12
VarCoeff [%]	10.15

540_50p8_4lay_stationary
540_50p8_4lay_sat.xls

	K [m²]		K [m²]		K [m²]
0°_v1	4.194E-11	45°_v1	3.464E-11	90°_v1	3.01531E-11
0°_v2	4.731E-11	45°_v2	3.143E-11	90°_v2	3.42332E-11
0°_v3	4.308E-11	45°_v3	3.310E-11	90°_v3	3.20519E-11
0°_v4	3.848E-11	45°_v4	3.513E-11	90°_v4	2.95252E-11
0°_v5	4.227E-11	45°_v5	3.511E-11	90°_v5	2.89172E-11
Mean	4.26E-11		3.39E-11		3.10E-11
StdDev	3.16E-12		1.60E-12		2.17E-12
VarCoeff [%]	7.42		4.73		7.00

	K1	K2	angle
curve fit	4.33946E-11	3.07931E-11	169.42
analyt.	4.31597E-11	3.06954E-11	169.80

540_55p5_4lay_stationary
540_55p5_4lay_sat.xls

	K [m²]
0°_v1	2.001E-11
0°_v2	1.851E-11
0°_v3	2.200E-11
0°_v4	1.731E-11
0°_v5	1.793E-11
Mean	1.92E-11
StdDev	1.88E-12
VarCoeff [%]	9.82

540_50p8_8lay_stationary
540_50p8_8lay_sat.xls

	K [m²]		K [m²]		K [m²]
0°_v1	4.805E-11	45°_v1	3.650E-11	90°_v1	3.466E-11
0°_v2	4.928E-11	45°_v2	3.388E-11	90°_v2	3.514E-11
0°_v3	5.017E-11	45°_v3	3.770E-11	90°_v3	3.946E-11
0°_v4	4.794E-11	45°_v4	4.007E-11	90°_v4	3.799E-11
0°_v5	4.941E-11	45°_v5	4.320E-11	90°_v5	4.061E-11
Mean	4.90E-11		3.83E-11		3.76E-11
StdDev	9.55E-13		3.54E-12		2.61E-12
VarCoeff [%]	1.95		9.26		6.96

	K1	K2	angle
curve fit	5.120E-11	3.650E-11	160.40
analyt.	5.137E-11	3.627E-11	159.94

540_55p5_8lay_stationary
540_55p5_8lay_sat.xls

	K [m²]
0°_v1	2.206E-11
0°_v2	1.965E-11
0°_v3	1.796E-11
0°_v4	1.850E-11
0°_v5	1.846E-11
Mean	1.93E-11
StdDev	1.65E-12
VarCoeff [%]	8.53

SAE 274 stationary tests p_{inj} = 1 bar

274_51p6_16lay_stationary
274_51p6_16lay_sat_1p.xls

	K [m²]		K [m²]		K [m²]
0°_v1	1.625E-11	**45°_v1**	1.638E-11	**90°_v1**	1.412E-11
0°_v2	1.358E-11	**45°_v2**	1.501E-11	**90°_v2**	5.806E-12
0°_v3	2.368E-11	**45°_v3**	1.685E-11	**90°_v3**	1.367E-11
0°_v4	2.716E-11	**45°_v4**	1.313E-11	**90°_v4**	1.241E-11
0°_v5	1.833E-11	**45°_v5**	1.945E-11	**90°_v5**	1.977E-11
Mean	1.98E-11		1.62E-11		1.32E-11
StdDev	5.54E-12		2.34E-12		4.99E-12
VarCoeff [%]	27.98		14.46		37.92

	K1	K2	angle
curve fit	2.123E-11	1.457E-11	171.92
analyt.	1.983E-11	1.314E-11	183.13

SAE 540 stationary tests p_{inj} = 1 bar

540_50p8_8lay_stationary_1p
540_50p8_8lay_sat_1p.xls

	K [m²]		K [m²]		K [m²]
0°_v1	4.071E-11	**45°_v1**	2.312E-11	**90°_v1**	3.386E-11
0°_v2	4.554E-11	**45°_v2**	2.836E-11	**90°_v2**	3.322E-11
0°_v3	4.941E-11	**45°_v3**	3.662E-11	**90°_v3**	3.757E-11
0°_v4	2.721E-11	**45°_v4**	3.325E-11	**90°_v4**	3.944E-11
0°_v5	3.606E-11	**45°_v5**	4.720E-11	**90°_v5**	4.009E-11
Mean	3.98E-11		3.37E-11		3.68E-11
StdDev	8.64E-12		9.10E-12		3.16E-12
VarCoeff [%]	21.72		27.01		8.57

	K1	K2	angle
curve fit	4.384E-11	3.521E-11	149.87
analyt.	4.449E-11	3.355E-11	142.98

A.3 List of Supervised Students

Name	Title of Thesis
Blaimer, Andreas	Permeabilitaetsmessung und Auswertung
Faber, Stefanie	Einfluss von Lagenanzahl und Flaechengewicht auf die Bestimmung der 2D-Permeabilitaet
Geisenhofer, Johannes	Ermittlung von Textilkennwerten mit Hilfe von Bildanalysemethoden
Hans, Thorsten	Ermittlung der Materialkennwerte geflochtener Strukturen
Holzapfel, Jakob	Fliesswegsimulation fuer ein CFK Monocoque im RTM Verfahren
Marquart, Maximilian	Methoden der Prozesssimulation fuer LCM-Prozesse
Meier, Reinhold	Methoden der Permeabilitaetsbestimmung fuer LCM-Prozesse
Radlmaier, Veronika	Optimierung eines Spritzgiessprozesses bei Verarbeitung eines langfaserverstaerkten Duroplasten
Riel, Ellen	RTM Prozesssimulation
Schaefer, Philipp	Materialcharakterisierung fuer Harzinfiltrationsprozesse
Schug, Alexander	Entwicklung einer Auswertemethodik fuer ungesaettigte Permeabilitaetsmessungen anhand von Drucksensoren
Shen, Yichen	Numerical permeability prediction using meso-scale models of carbon-fiber fabrics
Simon, Martin	Entwicklung von Simulationsmodellen zur Abbildung des Drapierprozesses textiler Halbzeuge mit Schnittstelle zur Simulation des Infiltrationsvorgangs
Weinzierl, Matthias	Entwicklung einer Methode zur Bestimmung gescherter Permeabilitaet
Elisabeth Winterstein	Simulation-based permeability determination of C-fibre fabrics using CT scans

List of Figures

List of Tables

Bibliography

[1] Flemming, M., G. Ziegmann and S. Roth: *Faserverbundbauweisen: Halbzeuge und Bauweisen*. Springer, Berlin, 1996.

[2] Jäger, H. and T. Hauke: *Carbonfasern und ihre Verbundwerkstoffe: Herstellungsprozesse, Anwendungen und Marktentwicklung*, volume 326 of *Die Bibliothek der Technik*. Verl. Moderne Industrie, München, 2010.

[3] McKinsey & Company: *Lightweight, heavy impact: How carbon fiber and other lightweight materials will develop across industries and specifically in automotive*, 2012.

[4] Advani, S. G. and M. E. Sozer: *Process modeling in composites manufacturing*. Marcel Dekker, New York, 2003.

[5] Aboudi, J., S. M. Arnold and B. A. Bednarcyk: *Micromechanics of composite materials: A generalized multiscale analysis approach*. Elsevier/Butterworth-Heinemann, Amsterdam and Boston, 1 edition, 2013.

[6] Whitaker, S.: *Flow in porous media I: A theoretical derivation of Darcy's law*. Transport in Porous Media, 1:3–25, 1986.

[7] Bear, J.: *Dynamics of fluids in porous media*. Dover, New York, 1988, c1972.

[8] Tucker, C. L. and R. B. Dessenberger: *Governing Equations for Flow and Heat Transfer in Stationary Fiber Beds*. In Advani, S. G. (editor): *Flow and rheology in polymer composites manufacturing*, pages 257–323. Elsevier, Amsterdam [etc.], 1994.

[9] Pillai, K. M.: *Governing equations for unsaturated flow through woven fiber mats. Part 1. Isothermal flows*. Composites Part A: Applied Science and Manufacturing, 33(7):1007–1019, 2002.

[10] Baehr, H. D. and K. Stephan: *Wärme- und Stoffübertragung*. Wärme- und Stoffübertragung, 2010.

[11] Brinkman, H.: *On the permeability of media consisting of closely packed porous particles*. Applied Scientific Research„ 1(1), 1947.

[12] Advani, S. G., M. V. Bruschke and R. S. Parnas: *Resin Transfer Molding Flow Phenomena in Polymeric Composites*. In Advani, S. G. (editor): *Flow and rheology in polymer composites manufacturing*, pages 464–515. Elsevier, Amsterdam [etc.], 1994.

[13] Binetruy, C.: *Physique du moulage des composites avancés : aspects théoriques.* Techniques de l'ingénieur Plasturgie : procédés spécifiques aux composites, Ref. article: am3718(TIB474DUO), 2004.

[14] Leclerc, J. S. and E. Ruiz: *Porosity reduction using optimized flow velocity in Resin Transfer Molding.* Composites Part A: Applied Science and Manufacturing, 39(12):1859–1868, 2008.

[15] Dimitrovova, Z. and S. G. Advani: *Analysis and Characterization of Relative Permeability and Capillary Pressure for Free Surface Flow of a Viscous Fluid across an Array of Aligned Cylindrical Fibers.* Journal of Colloid and Interface Science, 245(2):325–337, 2002.

[16] Dimitrovova, Z. and S. G. Advani: *Free boundary viscous flows at micro and mesolevel during liquid composites moulding process.* International Journal for Numerical Methods in Fluids, 46(4):435–455, 2004.

[17] Verleye, B., R. Croce, M. Griebel, M. Klitz, S. V. Lomov, G. Morren, H. Sol, I. Verpoest and D. Roose: *Permeability of textile reinforcements: Simulation, influence of shear and validation.* Composites Science and Technology, 68(13):2804–2810, 2008.

[18] Liakopoulos, A. C.: *Darcy's Coefficient of Permeability as Symmetric Tensor of Second Rank.* International Association of Scientific Hydrology. Bulletin, 10(3):41–48, 1965.

[19] Parry, R. H. G.: *Mohr circles, stress paths and geotechnics.* Spon Press, London and New York, 2 edition, 2004.

[20] Gebart, B.R and P. Lidstroem: *Measurement of in-plane permeability of anisotropic fiber reinforcements.* Polymer Composites, 17(1):43–51, 1996.

[21] Weitzenboeck, J. R., R. A. Shenoi and P. A. Wilson: *Measurement of principal permeability with the channel flow experiment.* Polymer Composites, 20(2):321–335, 1999.

[22] Papula, L.: *Mathematische Formelsammlung für Ingenieure und Naturwissenschaftler: Mit Rechenbeispielen und einer ausführlichen Integraltafel.* Studium. Vieweg, Wiesbaden, 8 edition, 2003.

[23] Alms, J. B., N. C. Correia, S. G. Advani, E. Ruiz and P. C. T. Goncalves: *Experimental Procedures to Run Longitudinal Injections to Measure Unsaturated Permeability of LCM Reinforcements*, 2010.

[24] Pfitzner, J.: *Poiseuille and his law.* Anaesthesia, 31(2):273–275, 1976.

[25] Chapuis, R. and M. Aubertin: *Predicting the Coefficient of Permeability of Soils using the Kozeny-Carman Equation: Report*, 2003.

[26] Gutowski, T. G., T. Morigaki and C. Zhong: *The Consolidation of Laminate Composites.* Journal of Composite Materials, 21(2):172–188, 1987.

[27] Gebart, B.R: *Permeability of Unidirectional Reinforcements for RTM.* Journal of Composite Materials, 26(8):1100–1133, 1992.

[28] Lundström, T.S.: *The permeability of non-crimp stitched fabrics.* Composites Part A: Applied Science and Manufacturing, 31(12):1345–1353, 2000.

[29] Nordlund, M., T.S Lundström, V. Frishfelds and A. Jakovics: *Permeability network model for non-crimp fabrics.* Composites Part A: Applied Science and Manufacturing, 37(6):826–835, 2006.

[30] Tran, T., C. Binetruy, S. Comas-Cardona and N. ABRIAK: *Microporomechanical behavior of perfectly straight unidirectional fiber assembly: Theoretical and experimental.* Composites Science and Technology, 69(2):199–206, 2009.

[31] Tran, T., S. Comas-Cardona, N.E. Abriak and C. Binetruy: *Unified microporomechanical approach for mechanical behavior and permeability of misaligned unidirectional fiber reinforcement.* Composites Science and Technology, 70(9):1410–1418, 2010.

[32] Rieber, G.: *Einfluss von textilen Parametern auf die Permeabilität von Multifilamentgeweben für Faserverbundkunststoffe: genehmigte Dissertation zur Verleihung des akad. Grades Dr.-Ing.*, volume 96 of *IVW-Schriftenreihe.* IVW, Kaiserslautern, 2011.

[33] Endruweit, A. and A. C. Long: *A model for the in-plane permeability of triaxially braided reinforcements.* Composites Part A: Applied Science and Manufacturing, 42(2):165–172, 2011.

[34] Calado, V. M.A. and S. G. Advani: *Effective average permeability of multi-layer preforms in resin transfer molding.* Composites Science and Technology, 56(5):519–531, 1996.

[35] Bruschke, M. V. and S. G. Advani: *A finite element/control volume approach to mold filling in anisotropic porous media.* Polymer Composites, 11(6):398–405, 1990.

[36] Chen, Z., L. Ye and H. Liu: *Effective permeabilities of multilayer fabric preforms in liquid composite moulding.* Composite Structures, 66(1-4):351–357, 2004.

[37] Diallo, M. L., R. Gauvin and F. Trochu: *Experimental analysis and simulation of flow through multi-layer fiber reinforcements in liquid composite molding.* Polymer Composites, 19(3):246–256, 1998.

[38] Trochu, F., R. Gauvin, M. Dong and J.-F Boudreault: *RTMFLOT - An Integrated Software Environment for the Computer Simulation of the Resin Transfer Molding Process.* Journal of Reinforced Plastics and Composites, 13(3):262–270, 1994.

[39] Adams, K. L. and L. Rebenfeld: *Permeability characteristics of multilayer fiber reinforcements. Part I: Experimental observations.* Polymer Composites, 12(3):179–185, 1991.

[40] Adams, K. L. and L. Rebenfeld: *Permeability characteristics of multilayer fiber reinforcements. Part II: Theoretical model.* Polymer Composites, 12(3):186–190, 1991.

[41] Luce, T. L., S. G. Advani, J. Howard and R. S. Parnas: *Permeability characterization. Part 2: Flow behavior in multiple-layer preforms.* Polymer Composites, 16(6):446–458, 1995.

[42] Parnas, R. S., J. Howard, T. L. Luce and S. G. Advani: *Permeability characterization. Part 1: A proposed standard reference fabric for permeability.* Polymer Composites, 16(6):429–445, 1995.

[43] Loendersloot, R.: *The structure -permeability relation of textile reinforcements.* PhD thesis, University of Twente, Twente, 2006.

[44] Elbouazzaoui, O.: *An Experimental Assessment of the Saturated Transverse Permeability of Non-crimped New Concept (NC2) Multiaxial Fabrics.* Journal of Composite Materials, 39(13):1169–1193, 2005.

[45] Drapier, S.: *Influence of the stitching density on the transverse permeability of non-crimped new concept (NC2) multiaxial reinforcements: measurements and predictions.* Composites Science and Technology, 62(15):1979–1991, 2002.

[46] Talvensaari, H., E. Ladstätter and W. Billinger: *Permeability of stitched preform packages: Fifth International Conference on Composite Science and Technology ICCST.* Composite Structures, 71(3–4):371–377, 2005.

[47] Grössing, H., M. Wohlfahrt and R. Schledjewski: *Comparison of Permeability Measurements of Several Fibre Textiles Using Different Measurement Methods.* Proeedings ECCM-15, 15(1), 2012.

[48] Parnas, R. S. and A. J. Salem: *A comparison of the unidirectional and radial in-plane flow of fluids through woven composite reinforcements.* Polymer Composites, 14(5):383–394, 1993.

[49] Lundstrom, T. S., B.R Gebart and E. Sandlund: *In-plane permeability measurements on fiber reinforcements by the multi-cavity parallel flow technique.* Polymer Composites, 20(1):146–154, 1999.

[50] Arbter, R., J.M Beraud, C. Binetruy, L. Bizet, J. Bréard, S. Comas-Cardona, C. Demaria, A. Endruweit, P. Ermanni, F. Gommer, S. Hasanovic, P. Henrat, F. Klunker, B. Laine, S. Lavanchy, S. V. Lomov, A. C. Long, V. Michaud, G. Morren, E. Ruiz, H. Sol, F. Trochu, B. Verleye, M. Wietgrefe, W. Wu and G. Ziegmann: *Experimental determination of the permeability of textiles: A benchmark exercise.* Composites Part A: Applied Science and Manufacturing, 42(9):1157–1168, 2011.

[51] Vernet, N., E. Ruiz, S. Advani, J.B Alms, M. Aubert, M. Barburski, B. Barari, J.M Beraud, D.C Berg, N. Correia, M. Danzi, T. Delavière, M. Dickert, C. Di Fratta, A. Endruweit, P. Ermanni, G. Francucci, J.A Garcia, A. George, C. Hahn, F. Klunker, S.V Lomov, A. Long, B. Louis, J. Maldonado, R. Meier, V. Michaud, H. Perrin, K. Pillai, E. Rodriguez, F. Trochu, S. Verheyden, M. Wietgrefe, W. Xiong, S. Zaremba and G. Ziegmann: *Experimental determination of the permeability of engineering textiles: Benchmark II.* Composites Part A: Applied Science and Manufacturing, 61:172–184, 2014.

[52] Lomov, S. V.: *Non-crimp fabric composites: Manufacturing, properties and applications.* Woodhead Publishing in materials. Woodhead Publishing, Cambridge and UK and Philadelphia and PA, 2011.

[53] Palmer, A. C.: *Dimensional analysis and intelligent experimentation.* World Scientific, Singapore, op. 2008.

[54] Liu, B., S. Bickerton and S. G. Advani: *Modelling and simulation of resin transfer moulding (RTM)–gate control, venting and dry spot prediction.* Composites Part A: Applied Science and Manufacturing, 27(2):135–141, 1996.

[55] Barandun, G. A.: *Injection strategies for liquid composite moulding processes.* PhD thesis, ETH Zürich, Zürich, 2009.

[56] Joubaud, L., V. Achim and F. Trochu: *Numerical Simulation of Resin Infusion and Reinforcement Consolidation Under Flexible Cover.* Polymer Composites, 26:417–427, 2005.

[57] Celle, P., S. Drapier and J. M. Bergheau: *Numerical modelling of liquid infusion into fibrous media undergoing compaction.* European Journal of Mechanics A/Solids, 27:647–661, 2008.

[58] Govignon, Q., S. Bickerton and P. A. Kelly: *Simulation of the Complete Resin Infusion Process*, 2008.

[59] Govignon, Q., S. Bickerton and P. A. Kelly: *Simulation of the reinforcement compaction and resin flow during the complete resin infusion process: Special Issue: Flow Processes in Composite Materials.* Composites Part A: Applied Science and Manufacturing, 41(1):45–57, 2010.

[60] Ruiz, E., V. Achim, S. Soukana, F. Trochu and J. Bréard: *Optimization of injection flow rate to minimize micro/macro-voids formation in resin transfer molded composites.* Composites Science and Technology, 66(3–4):475–486, 2006.

[61] Bickerton, S.: *Characterization and modeling of race-tracking in liquid composite molding processes.* Composites Science and Technology, 59(15):2215–2229, 1999.

[62] Advani, S. G. and P. Simacek: *Resin Flow Simulations in Liquid Composite Molding Pocesses: Recent Advances and Future Directions.* PhD thesis, University of Delaware,, Delaware, 2009.

[63] Verleye, B., A. Walbran, S. Bickerton and P. A. Kelly: *Simulation and experimental validation of force controlled compression resin transfer molding.* Journal of Composite Materials, 45(7):815–829, 2011.

[64] Isoldi, L. A., C. P. Oliveira, L. A. O. Rocha, J. A. Souza and S. C. Amico: *Three-dimensional numerical modeling of RTM and LRTM processes.* Journal of the Brazilian Society of Mechanical Sciences and Engineering, 34(2):105–111, 2012.

[65] Henne, M. and G. A. Barandun: *myRTM, a new tool for RTM process design.* JEC Composites Magazine, 2010(58):60–61, 2010.

[66] Koorevaar, A.: *Controlled vacuum infusion (CVI) technology*, 2009.

[67] Koorevaar, A.: *RTM-WORX: Features and detailed technical information*, 2009.

[68] Karl Mayer Textilmaschinenfabrik GmbH: *Warp Knitting Technology*, 2010.

[69] Spencer, David J.: *Knitting technology: A comprehensive handbook and practical guide.* Woodhead, Cambridge, 3 edition, 2001.

[70] Drago, A. and M. J. Pindera: *Micro-macromechanical analysis of heterogeneous materials.* Composites Science and Technology, 67(6):1243–1263, 2007.

[71] Trias, D., R. García, J. Costa, N. Blanco and J.E Hurtado: *Quality control of CFRP by means of digital image processing and statistical point pattern analysis.* Composites Science and Technology, 67(11-12):2438–2446, 2007.

[72] Verpoest, I. and S. V. Lomov: *Virtual textile composites software WiseTex: Integration with micro-mechanical, permeability and structural analysis: 20th Anniversary Special Issue.* Composites Science and Technology, 65(15-16):2563–2574, 2005.

[73] Sherburn, M.: *TexGen open source project.*, 2013.

[74] Robitaille, F., A. C. Long and C. D. Rudd: *Geometric modelling of textiles for prediction of composite processing and performance characteristics.* Plastics, Rubber and Composites, 31(2):66–75, 2002.

[75] Lomov, S. V., E. B. Belov, T. Bischoff, S. B. Ghosh, T. C. Truong and I. Verpoest: *Carbon composites based on multiaxial multiply stitched preforms. Part 1. Geometry of the preform.* Composites Part A: Applied Science and Manufacturing, 33(9):1171–1183, 2002.

[76] Lomov, S. V.: *Computational Models, Methods and Algorithms: Integrated Textile Preprocessor, WiseTex, Version 3.0.* PhD thesis, KU Leuven, Leuven, 2012.

[77] Lomov, S. V., I. Verpoest, M. Barburski and J. Laperre: *Carbon composites based on multiaxial multiply stitched preforms. Part 2. KES-F characterisation of the deformability of the preforms at low loads.* Composites Part A: Applied Science and Manufacturing, 34(4):359–370, 2003.

[78] Lomov, S. V., M. Barburski, T Stoilova, I. Verpoest, R. Akkerman, R. Loendersloot and R. H. W. Thije: *Carbon composites based on multiaxial multiply stitched preforms. Part 3: Biaxial tension, picture frame and compression tests of the preforms.* Composites Part A: Applied Science and Manufacturing, 36(9):1188–1206, 2005.

[79] Truong, T. C., M. Vettori, S. V. Lomov and I. Verpoest: *Carbon composites based on multi-axial multi-ply stitched preforms. Part 4. Mechanical properties of composites and damage observation.* Composites Part A: Applied Science and Manufacturing, 36(9):1207–1221, 2005.

[80] Loendersloot, R., S. V. Lomov, R. Akkerman and I. Verpoest: *Carbon composites based on multiaxial multiply stitched preforms. Part V: geometry of sheared biaxial fabrics.* Composites Part A: Applied Science and Manufacturing, 37(1):103–113, 2006.

[81] Vallons, K., M. Zong, S. V. Lomov and I. Verpoest: *Carbon composites based on multi-axial multi-ply stitched preforms – Part 6. Fatigue behaviour at low loads: Stiffness degradation and damage development.* Composites Part A: Applied Science and Manufacturing, 38(7):1633–1645, 2007.

[82] Guilleminot, J., C. Soize, D. Kondo and C. Binetruy: *Theoretical framework and experimental procedure for modelling mesoscopic volume fraction stochastic fluctuations in fiber reinforced composites.* International Journal of Solids and Structures, 45(21):5567–5583, 2008.

[83] Zhang, F., S. Comas-Cardona and C. Binetruy: *Statistical modeling of in-plane permeability of non-woven random fibrous reinforcement.* Composites Science and Technology, 72(12):1368–1379, 2012.

[84] Beavers, G. S. and D. D. Joseph: *Boundary conditions at a naturally permeable wall.* Journal of Fluid Mechanics, 30(01):197, 1967.

[85] Delerue, J.-F, S. V. Lomov, R. S. Parnas, I. Verpoest and M. Wevers: *Pore network modeling of permeability for textile reinforcements.* Polymer Composites, 24(3):344–357, 2003.

[86] Belov, E. B., S. V. Lomov, I. Verpoest, T. Peeters, D. Roose, R. S. Parnas, K. Hoes and H. Sol: *Modelling of permeability of textile reinforcements: lattice Boltzmann method.* Composites Science and Technology, 64(7-8):1069–1080, 2004.

[87] Wong, C. C., A. C. Long, M. Sherburn, F. Robitaille, P. Harrison and C. D. Rudd: *Comparisons of novel and efficient approaches for permeability prediction based on the fabric architecture: Selected Contributions from the 7th International Conference on Flow Processes in Composite Materials held at University of Delaware, USA.* Composites Part A: Applied Science and Manufacturing, 37(6):847–857, 2006.

[88] Wong, C.: *Modelling the Effects of Textile Preform Architecture on Permeability.* PhD thesis, University of Nottingham, Nottingham, 2006.

[89] Verleye, B.: *Computation of the permeability of multi-scale porous media with application to technical textiles.* PhD thesis, KU Leuven, Leuven, 2008.

[90] Verleye, B., S. V. Lomov, A. C. Long, I. Verpoest and D. Roose: *Permeability prediction for the meso-macro coupling in the simulation of the impregnation stage of Resin Transfer Moulding: Special Issue: Flow Processes in Composite Materials.* Composites Part A: Applied Science and Manufacturing, 41(1):29–35, 2010.

[91] Gonzalez, R. C. and R. E. Woods: *Digital image processing.* Prentice Hall, Upper Saddle River and N.J, 3 edition, 2008.

[92] Gonzalez, R. C., R. E. Woods and Steven L. Eddins: *Digital Image processing using MATLAB.* Gatesmark Publishing, United States, 2 edition, 2009.

[93] Otsu, N.: *A Threshold Selection Method from Gray-Level Histograms.* IEEE Transactions on Systems, Man, and Cybernetics, 9(1):62–66, 1979.

[94] Serra, J. P.: *Image analysis and mathematical morphology.* Academic Press, London and New York NY, 1988.

[95] Meyer, F.: *Topographic distance and watershed lines.* Mathematical Morphology and its Applications to Signal Processing, 38(1):113–125, 1994.

[96] Klein, J. C. and J. P. Serra: *The texture analyser.* Journal of Microscopy, 95(2):349–356, 1972.

[97] Haralick, R.M, K. Shanmugam and I. Dinstein: *Textural Features for Image Classification.* IEEE Transactions on Systems, Man, and Cybernetics, 3(6):610–621, 1973.

[98] Mostaço-Guidolin, L. B., A. C.T. Ko, F. Wang, B. Xiang, M. Hewko, G. Tian, A. Major, M. Shiomi and M. G. Sowa: *Collagen morphology and texture analysis: from statistics to classification.* Scientific Reports, 3, 2013.

[99] Oliveira, M.S, P.T Fernandes, W.M Avelar, S.L.M Santos, G. Castellano and L.M Li: *Texture analysis of computed tomography images of acute ischemic stroke patients.* Brazilian Journal of Medical and Biological Research, 42(11):1076–1079, 2009.

[100] Nishimura, T. and M. P. Ansell: *Fast Fourier Transform and Filtered Image Analyses of Fiber Orientation in OSB.* Wood Science and Technology, 36(4):287–307, 2002.

[101] Marquez, J. P.: *Fourier analysis and automated measurement of cell and fiber angular orientation distributions.* International Journal of Solids and Structures, 43(21):6413–6423, 2006.

[102] Peters, R. A.: *Lectures on Image Processing*, 2011.

[103] Canny, J.: *A Computational Approach to Edge Detection*. IEEE Transactions on Pattern Analysis and Machine Intelligence, 8(6):679–698, 1986.

[104] Tsai, D. and C. C. Kuo: *Defect detection in inhomogeneously textured sputtered surfaces using 3D Fourier image reconstruction*. Machine Vision and Applications, 18(6):383–400, 2007.

[105] Vanaerschot, A., B. N. Cox, S. V. Lomov and D. Vandepitte: *Stochastic framework for quantifying the geometrical variability of laminated textile composites using micro-computed tomography*. Composites Part A: Applied Science and Manufacturing, 44:122–131, 2013.

[106] Miene, A., A. S. Hermann and M. Göttinger: *Quality assurance by digital image analysis for the preforming and draping process of dry carbon fibre material*. Proceedings Sampe Europe 2008, 08(1):348–353, 2008.

[107] Miene, A.: *Bildanalytische Qualitätssicherung in der Preformfertigung*, 05.03.2010.

[108] Thumfart, S., W. Palfinger, M. Stöger and C. Eitzinger: *Accurate Fibre Orientation Measurement for Carbon Fibre Surfaces*. In Wilson, R., E. Hancock, A. Bors and W. Smith (editors): *Computer Analysis of Images and Patterns*, volume 8048 of *Lecture Notes in Computer Science*, pages 75–82. Springer Berlin Heidelberg, 2013.

[109] Frishfelds, V., A. Jakovics and T. S. Lundstrom: *Automatic Recognition and Analysis of Scanned Non-crimp Fabrics for Calculation of their Fluid Flow Permeability*. Journal of Reinforced Plastics and Composites, 26(3):285–296, 2007.

[110] Walbran, A. and H. Körber: *Towards Efficient Textile Characterisation: Key Parameters in Permeability and Compaction Characterisation*. Proceedings of the Texcomp-11 conference, 2013(11), 2013.

[111] Dubbel, H., K. H. Grote and J. Feldhusen: *Taschenbuch für den Maschinenbau*. Springer, Berlin and New York, 22 edition, 2007.

[112] Schug, A.: *Entwicklung einer Auswertemethodik für ungesättigte Permeabilitätsmessungen anhand von Drucksensoren: Semester thesis*, 2012.

[113] Faber, S.: *Einfluss von Lagenanzahl und Flächengewicht auf die Bestimmung der 2D-Permeabilität: Semester thesis*, 2013.

[114] Kim, Sung Jin and Seok Pil Jang: *Effects of the Darcy number, the Prandtl number, and the Reynolds number on local thermal non-equilibrium*. International Journal of Heat and Mass Transfer, 45(19):3885–3896, 2002.

[115] Leavers, V. F.: *Shape detection in computer vision using the Hough transform*. Springer-Verlag, London and New York, 1992.

[116] Yuen, H.K, J. Illingworth and J. Kittler: *Detecting partially occluded ellipses using the Hough transform.* Image and Vision Computing, 7(1):31–37, 1989.

[117] Rosin, P. L.: *Ellipse fitting by accumulating five-point fits.* Pattern Recognition Letters, 14(8):661–669, 1993.

[118] Taubin, G.: *Estimation Of Planar Curves, Surfaces And Nonplanar Space Curves Defined By Implicit Equations, With Applications To Edge And Range Image Segmentation.* IEEE Transactins on Pattern Analysis and Machine Intelligence, 13:1115–1138, 1991.

[119] Fitzgibbon, A. W., M. Pilu and R. B. Fisher: *Direct Least Squares Fitting of Ellipses.* IEEE Transactins on Pattern Analysis and Machine Intelligence, 21:476–480, 1999.

[120] Shen, Y.: *Numerical Permeability Prediction Using Meso-Scale Model of Carbon-fiber Fabrics: master thesis*, 2012.

[121] Lomov, S. V., I. Verpoest, J. Cichosz, C. Hahn, D. S. Ivanov and B. Verleye: *Meso-level textile composites simulations: Open data exchange and scripting.* Journal of Composite Materials, 48(5):621–637, 2014.

[122] Hahn, C., C. Binetruy, R. Hinterhölzl and K. Drechsler: *A Numerical Method of Permeability Determination for RTM Process Simulation.* Proceedings of the 11th International Conference on Flow Processing in Composite Materials (FPCM), 11, 2012.

[123] Greef, J. de, Y. Shen, C. Hahn, S. V. Lomov, D. Roose, B. Verleye and I. Verpoest: *Efficient generation of the voxel description of textile geometries for the computation of the permeability.* Proceedings of the 11th International Conference on Flow Processing in Composite Materials (FPCM), 11, 2012.

[124] Hahn, C., E. Winterstein, I. Straumit, B. Plank, R. Hinterhölzl, S. V. Lomov and C. Binetruy: *A simulation approach of permeability determination using computed tomography scans.* Proceedings of the Texcomp-11 conference, 11, 2013.

[125] Geisenhofer, J.: *Ermittlung von Textilkennwerten mit Hilfe von Bildanalysemethoden: diploma thesis*, 2012.

[126] Zeller, C.: *Dokumentation zum Matlab-Programm LCC-Faster: software documentation*, 2013.

[127] Winterstein, E.: *Simulation-based permeability determination of C-fibre fabrics using CT scans: master thesis*, 2013.

[128] Shoelson, B.: *MorphTool*, 2009.

[129] Roose, D., S. V. Lomov, T. Peeters and B. Verleye: *FlowTex User' Guide*, 2008.

[130] Swery, E., R. Meier, S. V. Lomov, C. Hahn, P. Kelly and I. Straumit: *Verification of FlowTex Solver Using Ansys CFX - Examining the Permeability Prediction Method on a Range of Textile Architecture Models.* Proceedings of the 16th European Conference on Composite Materials (ECCM), 16, 2014.

[131] ESI Group: *PAM-RTM 2013 - User's Guide & Tutorials*, 2012.

[132] Pickett, A. K. and G. Greech: *Meso-modelling of Non-Crimp Fabric composites for coupled drape and failure analysis.* Journal of Material Science, 41:6725–6736, 2006.

[133] Momentive: *Technical Information: EPIKOTE Resin MGS RIMR135*, 2012.

[134] Arnold, M., H. Franz, M. Bobertag, J. Glück, M. Cojutti, M. Wahl and P. Mitschang: *Kapazitive Messtechnik zur RTM-Prozessüberwachung.* lightweight design, 2013(1):50–55, 2013.

[135] Arnold, M., M. Cojutti and P. Mitschang: *Influence of the Shearing of Textiles on the In-Plane Permeability.* Proceedings of the 19th International Conference on Composite Materials (ICCM), 19, 2013.

[136] Demaria, C., E. Ruiz and F. Trochu: *In-plane anisotropic permeability characterization of deformed woven fabrics by unidirectional injection. Part I: Experimental results.* Polym Compos, 28(6):797–811, 2007.

[137] Demaria, C., E. Ruiz and F. Trochu: *In-plane anisotropic permeability characterization of deformed woven fabrics by unidirectional injection. Part II: Prediction model and numerical simulations.* Polym Compos, 28(6):812–827, 2007.